Self-assembly of pericentriolar material in interphase cells lacking centrioles

Fangrui Chen[1], Jingchao Wu[1], Malina K. Iwanski[1], Daphne Jurriens[1], Arianna Sandron[1], Milena Pasolli[1], Gianmarco Puma[1], Jannes Z. Kromhout[1], Chao Yang[1], Wilco Nijenhuis[1,2], Lukas C. Kapitein[1,2], Florian Berger[1] and Anna Akhmanova[1]

[1] Cell Biology, Neurobiology and Biophysics, Department of Biology, Faculty of Science, Utrecht University, Utrecht, The Netherlands

[2] Center for Living Technologies, Eindhoven-Wageningen-Utrecht Alliance, The Netherlands

Correspondence: a.akhmanova@uu.nl

Abstract

The major microtubule-organizing center (MTOC) in animal cells, the centrosome, comprises a pair of centrioles surrounded by pericentriolar material (PCM), which nucleates and anchors microtubules. Centrosome assembly depends on PCM binding to centrioles, PCM self-association and dynein-mediated PCM transport, but the self-assembly properties of PCM in interphase cells are poorly understood. Here, we used experiments and modeling to study centriole-independent features of interphase PCM assembly. We showed that when centrioles are lost due to PLK4 depletion or inhibition, dynein-based PCM transport and PCM self-clustering are sufficient to form a single compact MTOC, which generates a dense radial microtubule array. Interphase PCM self-assembly depends on γ-tubulin, pericentrin, CDK5RAP2 and ninein, but not NEDD1, CEP152 or CEP192. Formation of a compact acentriolar MTOC is inhibited by AKAP450-dependent PCM recruitment to the Golgi or by randomly organized CAMSAP2-stabilized microtubules, which keep PCM mobile and prevent its coalescence. Linking of CAMSAP2 to a minus-end-directed motor leads to the formation of an MTOC, but MTOC compaction requires cooperation with pericentrin-containing self-clustering PCM. Our data reveal that interphase PCM contains a set of components that can self-assemble into a compact structure and organize microtubules, but PCM self-organization is sensitive to motor- and microtubule-based rearrangement.

Introduction

The centrosome is the major microtubule organizing center (MTOC) in animal cells. It consists of two centrioles surrounded by pericentriolar material (PCM) (reviewed in (Conduit et al., 2015; Paz and Luders, 2017)). Major PCM components are microtubule-nucleating and anchoring proteins, which can associate with centrioles and with each other. For a long time it was thought that the PCM is amorphous, but super-resolution microscopy studies have shown that it has a distinct organization, with some proteins likely attached to the centriole wall and others organized around them (Fu and Glover, 2012; Lawo et al., 2012; Mennella et al., 2014; Mennella et al., 2012). This distinct organization is more obvious in interphase than in mitosis, when the microtubule-organizing capacity of the centrosome increases due to enhanced PCM recruitment. Many PCM components are known to oligomerize and interact with each other, and recent work suggested that the phase separation of interacting PCM components might contribute to centrosome assembly during mitosis (Raff, 2019; Woodruff et al., 2017). This idea is underscored by data showing that various cell-type-specific assemblies of PCM components can form clusters that are able to nucleate and organize microtubules and serve as MTOCs in the absence of centrioles, particularly during the formation of mitotic spindle poles (Balestra et al., 2021; Chinen et al., 2021; Gartenmann et al., 2020; Meitinger et al., 2020; Watanabe et al., 2020; Yeow et al., 2020). Furthermore, an important centrosome component, cytoplasmic dynein, is a motor that can bind to different PCM proteins and transport them to the centrosome-anchored microtubule ends, where these PCM proteins can nucleate and anchor additional microtubules, thus generating a positive feedback loop in centrosome assembly (Balczon et al., 1999; Burakov et al., 2008; Purohit et al., 1999; Redwine et al., 2017). Dynein and its mitotic binding partner NuMA also strongly participate in the formation of mitotic and meiotic spindle poles (Chinen et al., 2020; Khodjakov et al., 2000; Kolano et al., 2012). The relative importance of different molecular pathways of PCM assembly varies between cell systems and phases of the cell cycle and has not been explored systematically in interphase cells.

Here, we set out to investigate the centriole-independent self-assembly properties of interphase PCM. These properties, such as the ability of PCM to cluster or form molecular condensates, nucleate and anchor microtubules and move with motor proteins, are relevant because in most differentiated cell types, centrosome function is suppressed, and PCM forms acentrosomal MTOCs that are still poorly understood (Muroyama and Lechler, 2017; Sallee and Feldman, 2021). To study centriole-independent PCM function and dynamics, we removed centrioles using the PLK4 kinase inhibitor centrinone B which blocks centriole duplication (Wong et al., 2015). Importantly, in most commonly studied cultured cell lines, such as fibroblasts, epithelial, endothelial or cancer cells, microtubule networks are dense, and the centrosome is not the only MTOC. In such cells, non-centrosomal microtubule minus

63 ends are often stabilized by the members of CAMSAP family (Jiang et al., 2014; Meng et al., 2008;
64 Tanaka et al., 2012), and the Golgi apparatus serves as a second MTOC which nucleates and anchors
65 a very significant proportion of microtubules (Efimov et al., 2007; Rios, 2014; Wu et al., 2016; Zhu and
66 Kaverina, 2013). If centrosomes are lost because centriole duplication is blocked by inhibiting PLK4 or
67 depleting another essential centriole component, Golgi-dependent microtubule organization
68 becomes predominant (Gavilan et al., 2018; Martin et al., 2018; Wu et al., 2016). The ability of the
69 Golgi complex to serve as an MTOC critically depends on the Golgi adaptor AKAP450, which recruits
70 several PCM components that nucleate microtubules including the γ-tubulin ring complex (γ-TuRC),
71 CDK5RAP2 and pericentrin (Gavilan et al., 2018; Rivero et al., 2009; Wu et al., 2016). Moreover,
72 AKAP450 also tethers microtubule minus ends stabilized by CAMSAP2 to the Golgi membranes (Wu et
73 al., 2016). In the absence of AKAP450, the Golgi ribbon is maintained, but neither PCM components
74 nor CAMSAP-stabilized microtubule minus ends can be attached to the Golgi membranes and they are
75 instead dispersed in cytoplasm, leading to a randomly organized microtubule network (Gavilan et al.,
76 2018; Rivero et al., 2009; Wu et al., 2016). These data seem to suggest that centrioles and/or Golgi
77 membranes are essential to assemble PCM into an MTOC in interphase. However, this notion appears
78 to be inaccurate: in our previous study in RPE1 cells, we observed that a single compact acentriolar
79 MTOC (caMTOC) can still form after centriole loss in AKAP450 knockout cells, if the stabilization of
80 free minus ends in these cells is disabled by knocking out CAMSAP2 (Wu et al., 2016).

81 We used this observation as a starting point to investigate which properties of PCM allow it to self-
82 assemble in interphase mammalian cells and how the presence of non-centrosomal microtubules
83 affects this process. AKAP450 knockout cells provided a system to study PCM assembly in the absence
84 of competition with the Golgi-associated MTOC. caMTOC formation in AKAP450 knockout cells
85 required microtubules and depended on dynein, which brought together small PCM clusters with
86 attached minus ends. Experiments and modeling showed CAMSAP2-mediated minus-end stabilization
87 strongly perturbed PCM coalescence, because in the absence of AKAP450, randomly oriented
88 CAMSAP2-stabilized microtubules supported PCM motility and prevented PCM clustering. In the
89 absence of CAMSAP2, caMTOCs did form, but were often cylindrical rather than spherical in shape
90 and contained a subset of the major centrosome components. γ-tubulin, pericentrin, CDK5RAP2 and
91 ninein were necessary for the formation of caMTOCs, whereas some other major PCM proteins,
92 namely CEP192, CEP152 and NEDD1, were neither enriched in these structures nor required for their
93 formation, indicating that not all PCM components associate with each other in the absence of
94 centrioles. A single caMTOC containing PCM components could also form in the presence of CAMSAP2
95 when this protein was directly linked to a microtubule minus-end-directed motor. Importantly, in the
96 absence of pericentrin, minus-end-directed transport of CAMSAP2-stabilized minus ends organized

these ends into a ring, indicating that self-associating PCM is required for the formation of a caMTOC. This conclusion was supported by modeling. Taken together, our data show that a subset of interphase PCM components can self-assemble and efficiently nucleate and tether microtubules, but PCM clustering is sensitive to microtubule- and motor-dependent rearrangements. These properties of interphase PCM may also be involved in the transition from a centrosomal to a non-centrosomal microtubule network, as typically occurs during cell differentiation.

Results

Assembly of microtubule-dependent caMTOCs in AKAP450/CAMSAP2 KO cells lacking PLK4 activity

To study centriole-independent PCM organization and dynamics in interphase cells, we induced centriole loss in RPE1 cells by treating them for 11 days with the PLK4 inhibitor centrinone B (Wong et al., 2015) (Figure 1A,B). In wild type (WT) cells, PCM (detected with antibodies against pericentrin) relocalized to the Golgi apparatus, and the microtubule array reorganized around the Golgi membranes, as described previously (Gavilan et al., 2018; Wu et al., 2016) (Figure 1C,D). In AKAP450 knockout cells, centriole loss led to the appearance of strongly dispersed PCM clusters, which could no longer bind to the Golgi, and a highly disorganized microtubule system, consistent with published work (Gavilan et al., 2018; Wu et al., 2016) (Figure 1D,E). In contrast, in AKAP450/CAMSAP2 double knockout cells, a single caMTOC with microtubules focused around it was observed (Figure 1D-F). Formation of a single caMTOC was also observed in AKAP450 knockout cells transiently depleted of CAMSAP2 by siRNA transfection (Figure 1 – figure supplement 1A,B). As an alternative approach to block the ability of the Golgi apparatus to recruit PCM, we treated the cells with Brefeldin A, which disrupts the Golgi (Klausner et al., 1992). As expected, Brefeldin A by itself had no effect on centrosome integrity but led to the dispersal of the Golgi marker GM130 (Figure 1 – figure supplement 1C-E). In centrinone-treated wild type cells, PCM was dispersed after Golgi disruption, and the same was true for the majority of CAMSAP2 knockout cells (Figure 1 – figure supplement 1C-F). However, in 12 % of CAMSAP2 knockout cells treated with both centrinone B and Brefeldin A, we observed PCM compaction (Figure 1 – figure supplement 1D-F), similar to that seen in AKAP450/CAMSAP2 double knockout cells. The efficiency of caMTOC formation was low likely because dispersed AKAP450 could still recruit PCM to some extent or because the duration of the Brefeldin A treatment (2 hrs) was too short to allow for PCM compaction in most cells (longer Brefeldin A treatments were not performed due to potential cell toxicity). The acentriolar PCM can thus form a compact structure if both the Golgi MTOC and CAMSAP2-mediated minus-end stabilization are disabled.

Unlike centrosomes, which always have a spherical shape, caMTOCs in AKAP450/CAMSAP2 knockout cells were cylindrical in ~35% of the cells, whereas in the remaining cells that lacked centrioles based on staining for centrin, MTOCs had a round shape (~38% of the cells); the rest of the centrin-negative cells either had dispersed PCM clusters (~7%) or no detectable PCM clusters (~11%) (Figure 1 – figure supplement 2A, B). In contrast, ~72% of acentriolar AKAP450 knockout cells had dispersed PCM, while caMTOCs were very rare (Figure 1E, Figure 1 – figure supplement 2A, B). Analysis by Stimulated Emission Depletion (STED) microscopy revealed that cylindrical caMTOCs in AKAP450/CAMSAP2 knockout cells consisted of small clusters of PCM components, including pericentrin, CDK5RAP2, γ-

136 tubulin, ninein and dynein heavy chain (Figure 1F). caMTOCs with a clearly elongated shape had an
137 average length of ~11 µm and an average width of ~1.5 µm (Figure 1G).

138 To study PCM dynamics in caMTOCs, we generated cell lines stably expressing the PCM component
139 CDK5RAP2 tagged with GFP. In control, untreated cells, GFP-CDK5RAP2 was localized to the
140 centrosome and the Golgi apparatus as expected (Figure 1 – figure supplement 3A). In centrinone-
141 treated AKAP450/CAMSAP2 knockout cells, it was strongly enriched within caMTOCs and sometimes
142 also present in small motile clusters around a caMTOC (Figure 1H, Figure 1 – figure supplement 3B).
143 Fluorescence recovery after photobleaching (FRAP) assays showed that when the whole caMTOC was
144 bleached, the recovery was very slow and incomplete (Figure 1H, I). If only a part of a caMTOC was
145 photobleached, the dynamics of recovery showed cell-to-cell variability. Highly condensed caMTOCs
146 displayed a slow redistribution of GFP-CDK5RAP2 signal, suggesting that their components are largely
147 immobile and do not rearrange. In more loosely organized caMTOCs, some rearrangement of small
148 PCM clusters was observed (Figure 1H,I); however, the recovery was still far from complete. These
149 data indicate that caMTOCs display variable degrees of compaction and are composed of PCM clusters
150 that display limited exchange of GFP-CDK5RAP2 with the cytoplasmic pool, possibly because most of
151 the GFP-CDK5RAP2 is accumulated within the caMTOC.

152 Next, we investigated whether centriole loss induced by means other than pharmacological PLK4
153 inhibition could also cause the formation of a single caMTOC in AKAP450/CAMSAP2 knockout cells. To
154 achieve efficient protein depletion in RPE1 cells, they were transfected with siRNAs twice (on day 0
155 and day 2), treated with thymidine starting from day 4 to block cell cycle progression and fixed and
156 stained on day 5 or day 7 (Figure 1 – figure supplement 2C). Depletion of PLK4 using siRNAs caused
157 the appearance of round or cylindrical caMTOCs, similar to those observed after PLK4 inhibition with
158 centrinone B, indicating that catalytically inactive PLK4 had no scaffolding role within these structures
159 (Figure 1 – figure supplement 2C-F). The percentage of cells with caMTOCs increased over time (Figure
160 1 – figure supplement 2D), possibly due to the gradual depletion of PLK4. In contrast, depletion of
161 CPAP, an essential centriole biogenesis factor (Kohlmaier et al., 2009; Schmidt et al., 2009; Tang et al.,
162 2009), which also led to centriole loss, was much less efficient in inducing caMTOCs, and cylindrical
163 caMTOCs were never observed (Figure 1 – figure supplement 2C-E). After CPAP depletion, cells in
164 which pericentrin formed dispersed clusters or no visible clusters predominated (~67%, Figure 1 –
165 figure supplement 2D, E). Treatment of CPAP-depleted AKAP450/CAMSAP2 knockout cells with
166 centrinone B for 1 day promoted the assembly of round or cylindrical caMTOCs, and the proportion
167 of such cells increased to ~55% after 3 days of centrinone B treatment (Figure 1 – figure supplement
168 2C-G). We also tested whether the inhibition of PLK1, a kinase that is known to be a major regulator
169 of PCM self-assembly in mitosis (Haren et al., 2009; Joukov et al., 2014; Lee and Rhee, 2011), has an

170 effect on the formation of caMTOCs by treating cells with BI2536 (a highly selective and potent
171 inhibitor of PLK1), but found this not to be the case (Figure 1 – figure supplement 2C, D). We conclude
172 that PCM can assemble into a single stable MTOC in a centriole-independent manner if PLK4 is either
173 inactivated or depleted and the two major pathways of microtubule nucleation and minus-end
174 stabilization dependent on the Golgi membranes and CAMSAP2 are disabled.

175

176 ***Composition of caMTOCs and their effect on microtubule organization***

177 PCM is composed of numerous proteins that can bind to each other and interact with microtubules,
178 and we next set out to investigate which PCM components can self-assemble in the absence of
179 centrioles. We first stained centrinone-treated AKAP450/CAMSAP2 knockout cells with antibodies
180 against different centrosome and centriole markers and microtubule-associated proteins (MAPs). As
181 indicated above, the abundant PCM components pericentrin, CDK5RAP2, ninein and γ-tubulin
182 colocalized within caMTOCs (Figure 1F). In contrast, three other major PCM proteins, CEP152, CEP192
183 and NEDD1, could not be detected in these structures although they were present in centrosomes of
184 AKAP450/CAMSAP2 knockout RPE1 cells that were not treated with centrinone B (Figure 2A-C) and
185 were also expressed in centrinone-treated cells (Figure 2 – figure supplement 1A). We then
186 individually depleted all these proteins in centrinone-treated AKAP450/CAMSAP2 knockout cells using
187 siRNAs. After the depletion of pericentrin, no clusters of other PCM components could be detected
188 (Figure 2D,J,K, Figure 2 – figure supplement 1B). To confirm this result, we also attempted to knock
189 out pericentrin in AKAP450/CAMSAP2 knockout cells, but such cells were not viable, likely because
190 centrosome defects in these cells caused prolonged mitosis and p53-dependent G1 arrest (Fong et al.,
191 2016; Lambrus et al., 2016; Meitinger et al., 2016). However, we were able to knock out pericentrin in
192 cells lacking AKAP450, CAMSAP2 and p53 (Figure 2 – figure supplement 2), confirming that the loss of
193 p53 makes the cells more tolerant to centrosome absence and allows them to divide even in the
194 presence of centrinone B (Figure 2 – figure supplement 3, Video 1). Similar to pericentrin-depleted
195 cells, these quadruple knockout cells were unable to form a single caMTOC when treated with
196 centrinone B (Figure 2E, J). In these acentriolar quadruple knockout cells, CDK5RAP2, γ-tubulin and
197 cytoplasmic dynein displayed no clustering, while ninein and PCM1, a centriolar satellite protein that
198 localizes closely around the centrosome in normal cells (Prosser and Pelletier, 2020), formed small
199 clusters distributed throughout the cytoplasm (Figure 2 – figure supplement 4A). Loss of pericentrin
200 had no effect on the expression of CDK5RAP2, γ-tubulin and ninein (Figure 2 – figure supplement 4B),
201 indicating that clustering by pericentrin affects the organization but not the stability of these PCM
202 components.

203 The depletion of CDK5RAP2, γ-tubulin or ninein in centrinone-treated AKAP450/CAMSAP2 knockout
204 cells did not prevent the formation of small pericentrin clusters, but these failed to coalesce into a
205 single caMTOC (Figure 2F-H, J, Figure 2 – figure supplement 1B). In contrast, the depletion of CEP152,
206 CEP192 or NEDD1 had no effect on the formation of caMTOCs (Figure 2A-C, J, Figure 2 – figure
207 supplement 1B), in agreement with the fact these proteins could not be detected within these
208 structures. caMTOCs contained several centriole biogenesis factors, including CPAP, CP110 and
209 CEP120, but lacked centrin and CEP135; however, the depletion of different centriolar proteins did
210 not affect caMTOC formation (Figure 2K, Figure 2 – figure supplement 1C). Within caMTOCs, we also
211 detected a component of the HAUS complex (HAUS2), the centrosomal protein CEP170, dynein,
212 dynactin, CLASP1/2, CLIP-115, CLIP-170, chTOG, KIF2A and KIF1C (Figure 2K, Figure 2 – figure
213 supplement 1C). We tested the importance of some of these proteins for caMTOC formation by siRNA-
214 mediated depletion (see Figure 2K for an overview), but among the tested proteins, only cytoplasmic
215 dynein appeared essential for this process. In dynein-depleted cells, no clusters of pericentrin or other
216 PCM components could be detected after centrinone B treatment (Figure 2I-K). It is important to note,
217 however, that because we used siRNAs to reduce protein expression, we cannot exclude that the
218 residual levels of some of the investigated proteins were sufficient to support caMTOC formation.
219 Because we detected several microtubule plus-end tracking proteins (+TIPs) in the caMTOCs, such as
220 CLIP-170, CLASP1/2 and the large subunit of dynactin, p150Glued, we also tested for the presence of
221 the core components of the +TIP machinery, EB1 and EB3, but found that they were not enriched
222 within the caMTOCs (Figure 2K, Figure 2 – supplement 5A). Using the previously described cells that
223 lack EB3, CAMSAP2 and the C-terminal partner-binding half of EB1 (EB1/EB3/CAMSAP2mut cells; Yang
224 et al., 2017), we generated a knockout cell line that also lacks AKAP450 and found that caMTOCs could
225 still form in these cells (Figure 2K, Figure 2 – figure supplement 5B,C). We conclude that a subset of
226 PCM components binds to each other in the absence of centrioles, and in AKAP450/CAMSAP2
227 knockout cells, these proteins form caMTOCs that recruit a number of additional PCM proteins and
228 MAPs normally present in interphase centrosomes.

229 Despite containing only a subset of centrosomal proteins, caMTOCs strongly affected the organization
230 and density of the microtubule network in acentriolar cells: microtubules were focused around
231 caMTOCs if present and disorganized in cells lacking caMTOCs. The strongest loss of microtubule
232 density was observed in cells lacking pericentrin, dynein or γ-tubulin, while milder phenotypes were
233 observed in cells lacking CDK5RAP2 or ninein (Figure 3A,B,E). To further characterize microtubule
234 organization after the loss of these proteins, we analyzed the proportion of the radial and non-radial
235 microtubules. Whereas control cells (AKAP450/CAMSAP2 knockout cells treated with centrinone B
236 and control siRNA) formed radial microtubule networks with ~12% non-radial microtubules,

237 acentriolar cells lacking pericentrin or cytoplasmic dynein had ~46% non-radial microtubules, and the
238 depletion of CDK5RAP2, ninein and γ-tubulin led to an intermediate phenotype with 25-30% non-
239 radial microtubules (Figure 3C,D,E). An acentriolar PCM assembly containing pericentrin, CDK5RAP2,
240 ninein, γ-tubulin and dynein is thus sufficient to form a radial microtubule array, similar to a
241 centrosome, and PCM clustering promotes dense microtubule organization.

242

243 ***Dynamics of caMTOC disassembly***

244 To test whether the formation and maintenance of caMTOCs depends on microtubules, we
245 depolymerized them by treating cells with nocodazole at 37°C and found that caMTOCs fragmented
246 into small clusters upon nocodazole treatment and reassembled into a single structure after
247 nocodazole washout (Figure 4A-C). Because we found that caMTOC formation is dynein-dependent,
248 we also included the dynein inhibitor dynapyrazole A in these experiments (Steinman et al., 2017). We
249 confirmed that treatment with dynapyrazole A for 3 hrs had no effect on dynein expression (Figure
250 4D) and found that the addition of this drug before nocodazole treatment prevented the disassembly
251 of caMTOCs, whereas the treatment of cells with dynapyrazole A during nocodazole washout strongly
252 inhibited caMTOC re-assembly (Figure 4A-C). These data indicate that both microtubule-dependent
253 dispersal and coalescence of PCM clusters into caMTOCs are driven by dynein activity.

254 We next studied PCM dynamics using stably expressed GFP-CDK5RAP2 as a marker in live cells where
255 microtubules were labeled with SiR-tubulin. GFP-CDK5RAP2 was mostly immobile within caMTOCs
256 before nocodazole treatment (Figure 1 – figure supplement 3B, Video 2). After a few minutes of
257 nocodazole treatment, when the microtubule density was significantly reduced, small PCM clusters
258 started to move out of the caMTOC and undergo rapid directional motility with speeds of up to 2
259 µm/sec, which is within the range characteristic for cytoplasmic dynein (Schlager et al., 2014) (Figure
260 4E,F, Figure 4 – figure supplement 1A, Video 2). Once microtubules were completely disassembled,
261 the movement of GFP-CDK5RAP2-positive clusters stopped, indicating that it is microtubule-
262 dependent but occurs only when the microtubule network is partially depolymerized. Since cluster
263 dispersal towards the cell periphery could be blocked by a dynein inhibitor, and since cytoplasmic
264 dynein is a minus-end-directed motor, these data indicate that during microtubule disassembly by
265 nocodazole at 37°C, there is a transient stage when PCM clusters interact with only a few
266 microtubules, some of which have their minus-ends facing outwards, and these microtubules serve as
267 tracks for PCM transport. To support this idea, we used motor-PAINT, a technique that employs
268 nanometric tracking of purified kinesin motors on the extracted cytoskeleton of fixed cells to super-
269 resolve microtubules and determine their orientation (Tas et al., 2017). Using this approach, we

270 determined microtubule orientations in centrinone-treated AKAP450/CAMSAP2 knockout cells and in
271 cells that were also treated with nocodazole for 15 min to induce partial microtubule disassembly
272 (Figure 4G, Figure 4 – figure supplement 1B). We found that the cells contained a significant number
273 of minus-end-out microtubules, and their proportion increased during early stages of nocodazole
274 treatment, possibly because minus-end-out microtubules are more stable (Figure 4G, e.g., minus-end-
275 out microtubules constituted ~23% of the total microtubule length determined from kinesin-1
276 trajectories in the untreated cell and ~46% in the nocodazole-treated cell). These microtubules could
277 serve as tracks for outward movement of PCM, causing the disassembly of caMTOC when the overall
278 microtubule density around the caMTOC was strongly reduced (Figure 4H). These data suggest that
279 the dense network of PCM-anchored microtubule minus-ends around a caMTOC allows for its
280 compaction via dynein-mediated forces, but that dynein can pull the caMTOC apart when
281 microtubules are disorganized.

282 To further confirm that caMTOC disassembly is an active microtubule-dependent process, we also
283 depolymerized microtubules by a combination of cold (4°C) and nocodazole treatment. When all
284 microtubules were depolymerized, caMTOCs did not fall apart, even when the cells were subsequently
285 warmed to 37°C in the presence of nocodazole, so that microtubules could not re-grow (Figure 4I).
286 However, we noticed that in these conditions, the continuity and cylindrical organization of the PCM
287 cluster were often perturbed. This raised the possibility that the elongated arrangement of PCM
288 components within caMTOCs is microtubule-driven. Indeed, when cells were subjected to cold (4°C)
289 treatment in the absence of nocodazole, most of microtubules depolymerized, but some short cold-
290 stable microtubules remained associated with the caMTOC (Figure 4 – figure supplement 1C). These
291 data indicate that PCM self-assembly in the absence of centrioles is microtubule-dependent, and
292 microtubules are involved in shaping the PCM cluster. Once assembled, the PCM cluster is quite stable,
293 unless microtubule organization is altered and dynein-driven microtubule-based transport pulls it
294 apart.

295

296 ***Dynamics of caMTOC assembly***

297 When nocodazole-mediated microtubule disassembly was carried out at 4°C, the caMTOC remained
298 intact and after nocodazole washout it served as the major microtubule nucleation site, similar to the
299 centrosome in untreated wild-type cells (Figure 5 – figure supplement 1A). However, when
300 nocodazole-mediated disassembly of the caMTOC was carried out at 37°C, the cluster fell apart and
301 reassembled upon nocodazole washout (Figure 4A, B), providing a way to study the dynamics of PCM
302 self-assembly and the roles of different PCM components during this process. Small PCM clusters

303 positive for pericentrin, CDK5RAP2, γ-tubulin and the centriolar satellite protein PCM1 that co-
304 localized with the plus-ends of microtubules (labeled with EB1) could be detected 30 s after
305 nocodazole washout; these PCM clusters and nascent microtubules did not colocalize with the Golgi
306 membranes (Figure 5A, Figure 5 – figure supplement 1B). Ninein was not detected within the clusters
307 at this early stage of microtubule regrowth but could be found 2 min after nocodazole washout. In
308 contrast, no clusters of CEP192 or NEDD1 were observed even 10 min after nocodazole washout
309 (Figure 5A, Figure 5 – figure supplement 1B,C). The depletion of pericentrin, CDK5RAP2 and γ-tubulin
310 strongly inhibited microtubule nucleation in these conditions, whereas the depletion of dynein heavy
311 chain or ninein had a milder effect (Figure 5B,C). Live cell imaging with GFP-CDK5RAP2 and SiR-tubulin
312 showed that CDK5RAP2 clusters with attached microtubules coalesced by undergoing microtubule-
313 based movements (Figure 5D), and measurements in cells fixed at different time points after
314 nocodazole washout showed that a partly radial microtubule system emerged already 2 min after
315 nocodazole washout (Figure 5 – figure supplement 1D). Reassembly of a single caMTOC in the central
316 part of the cell occurred within ~15 min after nocodazole washout, though it was less compact than
317 in cells that were not treated with nocodazole (Figure 5D-G). Depletion of pericentrin, γ-tubulin and
318 dynein heavy chain strongly inhibited the reformation of a radial microtubule network during
319 nocodazole washout, whereas the effect of depleting CDK5RAP2 and ninein was less strong (Figure 5
320 – figure supplement 1D-F). Live cell imaging of acentriolar AKAP450/CAMSAP2 knockout RPE1 cells
321 stably expressing GFP-CDK5RAP2 showed that when pericentrin was depleted, CDK5RAP2 clusters
322 were not detectable, and the microtubule network, both before nocodazole treatment and after
323 nocodazole washout, was disorganized (Figure 5 – figure supplement 2, Video 3). Taken together, our
324 data show that pericentrin and γ-tubulin form microtubule-nucleating and anchoring units, which are
325 clustered by the self-association of pericentrin and assembled into larger structures by dynein-based
326 transport. CDK5RAP2 contributes to microtubule nucleation efficiency, whereas ninein appears to act
327 somewhat later and contributes to the formation of a compact PCM cluster and a radial microtubule
328 network. Importantly, all these proteins can cluster in the absence of centrioles, and together they
329 can efficiently nucleate and anchor microtubules.

330

331 ***The role of CAMSAP2-stabilized minus ends in defining microtubule network geometry***

332 The results of nocodazole treatment and washout suggested that PCM can self-assemble into a
333 caMTOC which nucleates and anchors microtubules, but this structure is sensitive to microtubule
334 organization. This observation prompted us to investigate in more detail how the microtubules that
335 are not anchored at PCM clusters affect PCM organization in steady state conditions. An abundant

336 population of stable minus ends that do not attach to PCM is decorated by CAMSAP2. In centrinone-
337 treated wild type cells, CAMSAP2-bound microtubule minus ends were anchored at the Golgi (Wu et
338 al., 2016)(Figure 1D), whereas in centrinone-treated AKAP450 knockout cells they were distributed
339 randomly (Figure 1D, 6A). Live imaging showed that CAMSAP2-decorated minus ends displayed only
340 limited motility on the scale of hours and thus formed a relatively stationary, disorganized microtubule
341 network (Video 4). Live imaging of GFP-CDK5RAP2 together with SiR-tubulin in these cells
342 demonstrated that small PCM clusters were distributed throughout the cytoplasm (Figure 6B). These
343 clusters moved along microtubules and encountered each other, but the direction of the movements
344 was random and the clusters did not coalesce into a single structure (Figure 6B, Figure 6 – figure
345 supplement 1A, Video 5). Treatment with nocodazole and subsequent nocodazole washout confirmed
346 that the motility of GFP-CDK5RAP2 clusters in centrinone-treated AKAP450 knockout cells was
347 microtubule-dependent, and that these clusters could nucleate microtubules and move together with
348 microtubule minus ends, but did not converge into a single caMTOC (Figure 6 – figure supplement 1A-
349 C, Video 5). Treatment with dynapyrazole A strongly inhibited the movements of small PCM clusters
350 (Figure 6 – figure supplement 1D,E, Video 6), indicating that they are dynein-driven. After the
351 depletion of pericentrin, GFP-CDK5RAP2 became completely diffuse, and it failed to form clusters
352 during nocodazole treatment or washout (Figure 6 – figure supplement 2, Video 7), indicating that
353 clustering of GFP-CDK5RAP2 in AKAP450 knockout cells is pericentrin-dependent. Based on these data,
354 we conclude that in AKAP450 knockout cells, pericentrin still forms PCM clusters that can nucleate
355 microtubules and can be moved by dynein along other microtubules, similar to what occurs in wild-
356 type cells. However, in the absence of AKAP450, CAMSAP2-stabilized microtubules form a
357 disorganized network, which imposes a random motility pattern on pericentrin-dependent PCM
358 clusters and thus prevents their assembly into a single caMTOC, likely because PCM interactions are
359 not sufficient to trigger their stable association (Figure 6C).

360 If the geometry of the CAMSAP2-stabilized microtubule network determines PCM distribution,
361 focusing CAMSAP2-bound minus ends is expected to bring PCM together. To test this idea, we linked
362 CAMSAP2-stabilized minus ends to a minus-end-directed motor. In order to avoid potential cell
363 toxicity associated with manipulating cytoplasmic dynein, we used the motor-containing part of a
364 moss kinesin-14, type VI kinesin-14b from the spreading earthmoss *Physcomitrella patens* (termed
365 here ppKin14). The C-terminal motor-containing part of this protein can efficiently induce minus-end-
366 directed motility of different cargoes in mammalian cells when it is tetramerized through a fusion with
367 the leucine zipper domain of GCN4 (GCN4-ppKin14-VIb (861–1321)) and recruited to cargoes using
368 inducible protein heterodimerization (Jonsson et al., 2015; Nijenhuis et al., 2020). We employed a
369 chemical heterodimerization system that is based on inducible binding of two protein domains, FRB

370 and FKBP, upon the addition of a rapamycin analog (rapalog) (Pollock et al., 2000). To ensure that all
371 CAMSAP2-decorated microtubule minus ends were linked to kinesin-14, we rescued centrinone-
372 treated AKAP450/CAMSAP2 knockout cells by expressing CAMSAP2 fused to a tandemly repeated
373 FKBP domain (2FKBP-mCherry-CAMSAP2) (Figure 6D-F). This construct was co-expressed with the FRB-
374 GCN4-tagBFP-ppKin14 fusion, which by itself localized quite diffusely, with only a weak enrichment
375 along microtubules, as described previously (Nijenhuis et al., 2020) (Figure 6D,F). In the absence of
376 rapalog, CAMSAP2-decorated microtubule minus ends were distributed randomly, similar to
377 endogenous CAMSAP2 in AKAP450 knockout cells (Figure 6F). However, upon rapalog addition,
378 ppKin14 was rapidly recruited to CAMSAP2-decorated microtubule ends, and after 2 hrs, more than
379 90% of cells acquired a radial microtubule organization (Figure 6E-G). In rapalog-treated cells,
380 CAMSAP2-bound microtubule minus ends formed either a tight cluster or a "whirlpool-like" ring in the
381 cell center (Figure 6D-G, Figure 6 – figure supplement 1F). The whirlpool-like arrangement likely comes
382 about when CAMSAP2-stretches are a bit longer and continue to slide against each other, forming a
383 nematic circular bundle. The major caMTOC components, pericentrin, CDK5RAP2, γ-tubulin and ninein
384 were also concentrated within the CAMSAP2 cluster (Figure 6F, Figure 6 – figure supplement 1F).
385 These data indicate that the positioning of stabilized minus-ends is an important determinant of the
386 overall microtubule organization and PCM localization in interphase cells.

387

388 ***The role of PCM in CAMSAP2-driven microtubule organization***

389 Presence of PCM in the caMTOC induced by minus-end-directed transport of CAMSAP2 might be a
390 passive consequence of microtubule reorganization, but might also play an active role in forming this
391 caMTOC. To distinguish between these possibilities, we attached CAMSAP2 to ppKin14 in centrinone
392 -treated cells where both AKAP450 and pericentrin were knocked out
393 (AKAP450/CAMSAP2/p53/pericentrin knockout). In the absence of rapalog, CAMSAP2-stabilized
394 minus ends and the whole microtubule network were disorganized, as expected, and the same was
395 true when the two constructs were expressed separately, with or without rapalog (Figure 7A,D, Figure
396 7- figure supplement 1). After rapalog addition, microtubules in cells expressing both constructs
397 acquired a radial organization, but their minus ends usually did not converge in a single spot but rather
398 accumulated in a ~30-70 µm-large ring-like structure (Figure 7A,D, Figure 7- figure supplement 2,
399 Video 8). Staining for PCM markers showed that CDK5RAP2 and γ-tubulin were enriched in the vicinity
400 of CAMSAP2-positive microtubule minus ends, whereas ninein appeared rather diffuse (Figure 7A). To
401 determine the nature of the structure "corralled" by the ring of CAMSAP2-decorated minus ends in
402 rapalog-treated cells, we stained for different membrane organelles and found that whereas there

403 was no strong correlation with the nucleus, Golgi membranes or lysosomes, the majority of
404 mitochondria were found within the CAMSAP2 ring, and the endoplasmic reticulum (ER) displayed
405 increased density overlapping with the CAMSAP2 ring (Figure 7B, Figure 7 - figure supplement 2B). It
406 therefore appeared that in the absence of pericentrin, CAMSAP2-decorated minus ends were brought
407 together by ppKin14, but their convergence was inefficient and possibly impeded by membrane
408 organelles enriched in the central, thicker part of the cell before rapalog addition (see the upper panel
409 of Figure 7 - figure supplement 2B). Transient transfection of centrinone-treated
410 AKAP450/CAMSAP2/p53/pericentrin knockout cells with GFP-pericentrin rescued the formation of a
411 tight CAMSAP2 cluster upon rapalog treatment (Figure 7C). Our data show that pericentrin-containing
412 PCM contributes to the formation of a caMTOC driven by minus-end-directed transport of CAMSAP2-
413 stabilized minus-ends.

414 To support this notion further, we also generated cells that were knockout for AKAP450, CAMSAP2,
415 CDK5RAP2, myomegalin (MMG, homologue of CDK5RAP2), p53 and pericentrin. To achieve this, we
416 used the previously described RPE1 cell line knockout for AKAP450, CAMSAP2, CDK5RAP2 and MMG
417 (Wu et al., 2016), in which we sequentially knocked out p53 and pericentrin (Figure 7 – figure
418 supplement 3A-G). While it was not possible to induce centriole loss by centrinone B treatment in
419 AKAP450/CAMSAP2/CDK5RAP2/MMG knockout cells because the proliferation of these cells was
420 arrested in the absence of centrioles (Wu et al., 2016), centriole removal was successful in
421 AKAP450/CAMSAP2/CDK5RAP2/MMG/p53/pericentrin knockout cells due to the absence of p53 and
422 led to microtubule disorganization (Figure 7 – figure supplement 3H). Interestingly, when these cells
423 were co-transfected with FKBP-linked CAMSAP2 and FRB-linked ppKin14 and treated with rapalog
424 (Figure 6D), we observed that CAMSAP2 clustering was even less efficient than in
425 AKAP450/CAMSAP2/p53/pericentrin knockout cells (Figure 7D,E). 49% of
426 AKAP450/CAMSAP2/CDK5RAP2/MMG/p53/pericentrin knockout cells had small bundles of CAMSAP2
427 stretches dispersed throughout the cytoplasm, and only 37% of these cells formed a ring of CAMSAP2-
428 decorated minus ends, whereas 80% of AKAP450/CAMSAP2/p53/pericentrin knockout cells formed
429 such a ring. We examined the ER and mitochondria in these cells and found that in cells that did form
430 a CAMSAP2 ring, the ER displayed an overlapping ring-like density, although the mitochondria inside
431 the CAMSAP2 ring were more scattered compared to those of AKAP450/CAMSAP2/p53/pericentrin
432 knockout cells (Figure 7 – figure supplement 2B). In cells with dispersed CAMSAP2-positive bundles,
433 no increased ER density or central accumulation of mitochondria were observed (Figure 7 – figure
434 supplement 2B). These data further support the notion that minus-end-directed transport of stable
435 minus ends alone is insufficient to generate a caMTOC, and that synergy with PCM is required.

436

437 ***Recapitulation of PCM self-organization by computer simulations***

438 To rationalize the appearance of the different microtubule arrangements and to find a minimal set of
439 interactions between filaments and motors that would lead to self-organization into structures that
440 we observed experimentally, we set up agent-based computer simulations with Cytosim (Nedelec and
441 Foethke, 2007). First, we sought to recapitulate the formation of a single PCM cluster. The numerical
442 values for the parameters of our simulations have been taken from literature or reasonably chosen
443 otherwise (Supplemental Table S1). For simplicity, we considered a two-dimensional circular cell with
444 a radius of 10 µm. We described a mobile PCM complex as a bead with a radius of 50 nm from which
445 one microtubule plus end could grow. Microtubule growth and shrinkage were simulated with the
446 classical microtubule model from Cytosim. When the microtubule reached a maximal length of 7.5
447 µm, its growth was stopped. In this way, we limited the microtubule length to avoid long microtubules
448 that push their minus end to the periphery of the cell. Additionally, one dynein molecule was attached
449 to a PCM complex with its cargo-binding domain. With this configuration, dynein molecules could
450 transport PCM complexes along microtubules growing from other PCM complexes. Once they were
451 bound to a microtubule, they walked towards the minus end in a force-dependent manner. When a
452 dynein motor reached a minus end, it detached. Furthermore, we implemented a reversible binding
453 interaction between PCM complexes to make them adhere to each other. Because we were interested
454 in the spatial arrangement of the PCM complexes, we introduced steric interactions between them.
455 However, we neglected steric interactions between microtubules to effectively account for the three-
456 dimensional space that we projected to two dimensions. Simulations of 300 of such PCM complexes
457 reproducibly reached a steady state in which they formed a compact centrally located cluster (Figure
458 8A, Video 9A). Quantification of 10 simulations showed that the mean and standard deviation of the
459 distance from each PCM complex to the average location of all complexes (the center of mass) were
460 small compared to the radius of the cell (Figure 8E, F). However, if we disabled the adhesive
461 interactions between PCM complexes, they formed a loose ring-like arrangement and not a compact
462 cluster (Figure 8B, Video 9B), and the mean and standard deviation of the distance of PCM complexes
463 to the center of mass were larger (Figure 8E, F). Taken together, our simulations support the idea that
464 PCM components form a central cluster through positive feedback of dynein molecules carrying them
465 towards the minus ends of microtubules attached to other PCM proteins, and that adhesive
466 interactions between the PCM complexes promote cluster compaction.

467 In our experiments, we saw that the presence of CAMSAP2-stabilized microtubule network prevented
468 PCM clustering (Figure 1D,E, Figure 6A-C), and that CAMSAP2-bound minus ends appeared almost
469 stationary on the scale of minutes (Video 4) compared to the rapid dynein-driven movement of small
470 PCM clusters (Video 5). To simulate such a situation, we assumed that 300 microtubules could grow

471 and shrink with random orientations from CAMSAP2-stabilized microtubule ends that were randomly
472 distributed and stationary within the cell. Furthermore, we assumed that some of the moving PCM
473 complexes were not efficient in nucleating microtubules, because the presence of a PCM-independent
474 microtubule population would reduce the concentration of soluble tubulin and thus nucleation
475 efficiency. To effectively account for such an effect, we allowed only 50 of the 300 PCM complexes to
476 nucleate microtubules. In this system, the PCM cluster formation was disrupted, and PCM complexes
477 randomly moved around the cell (Figure 8C, Video 9C). The distributions of the distances to the
478 average position of the PCM complexes were broad and had a large mean and standard deviation,
479 indicating the dispersed localization (Figure 8E, F). However, if we increased the strength of adhesive
480 interactions between the PCM complexes, the randomly oriented microtubule network no longer
481 suppressed the clustering of PCM complexes (Figure 8D, Video 9D). Therefore, the presence of a
482 stationary randomly organized microtubule network can be sufficient to block the formation of a
483 compact PCM cluster even though individual PCM complexes can still move with dynein and adhere
484 to each other, provided that the interaction between PCM complexes is not too tight.

485 Next, we examined how CAMSAP2-stabilized microtubules would organize when minus-end-directed
486 kinesin-14 motors could attach to them and carry the minus ends. CAMSAP2-stabilized microtubule
487 ends bound to kinesin-14 motors (termed "CAMSAP-kin14 complexes" in the text below) were
488 modelled as a bead with a radius of 50 nm from which a microtubule could grow and to which 6
489 kinesin-14 molecules were attached. Because the biophysical properties of single plant kinesin-14
490 molecules used in our assays are poorly understood, we assumed typical kinesin-1 values with an
491 opposite directionality. CAMSAP-kin14 complexes only interacted sterically but did not adhere to each
492 other. In a simulation of 300 CAMSAP-kin14 complexes, a loose ring-like arrangement appeared
493 (Figure 8G), similar to the one observed in our simulations of PCM complexes that could not bind to
494 each other (Figure 8B). Introducing adhesive interactions between CAMSAP-kin14 complexes was
495 sufficient to promote compact cluster formation (Figure 8H).

496 Finally, to investigate if a compact cluster of CAMSAP-kin14 complexes would emerge in the presence
497 of self-associating PCM complexes, we set up simulations with 150 CAMSAP-kin14 complexes together
498 with 150 adherent PCM complexes. The steady state of such a system displayed a compact central
499 cluster, in which both types of complexes were mixed (Figure 8I,K,L, Video 9I), while making PCM
500 complexes non-adhesive prevented cluster compaction (Figure 8J,K,L, Video 9J). Taken together, our
501 simulations suggest that the PCM complexes provide enough adhesive interactions to compact the
502 cluster of non-interacting CAMSAP-kin14 and PCM complexes, very similar to our experimental
503 observations.

504 **Discussion**

505 In this study, we explored the mechanisms of interphase PCM self-assembly in the absence of
506 centrioles. Our experiments and simulations support the idea that PCM complexes can form a single
507 cluster through a positive feedback mechanism, whereby dynein motors carry microtubule minus-
508 ends to other microtubule minus ends (Cytrynbaum et al., 2004). However, for a compact cluster to
509 emerge, the minus ends must not only be able to move towards each other but also to bind to each
510 other, and this idea is fully supported by our simulations. Interphase PCM is thus capable both of
511 dynein binding and self-association sufficient to organize a compact microtubule-nucleating and
512 anchoring structure in the absence of centrioles. However, the formation of a compact MTOC in
513 acentriolar cells is slow and less robust than in centriole-containing cells, and the resulting structure
514 is sensitive to the overall organization of microtubules and to dynein function. This means that
515 interphase PCM self-association is by itself reversible and not sufficiently tight to resist dynein-driven
516 forces. Centrioles can thus be regarded as catalysts of PCM assembly and stabilizers of interphase
517 centrosomes, preventing PCM movement on microtubules oriented with their minus ends away from
518 the centrosome.

519 Our experimental system allowed us to examine which PCM components are capable of associating
520 with each other and with dynein to promote microtubule nucleation and anchoring independently of
521 centrioles. The major scaffold for interphase acentriolar PCM assembly is pericentrin, which can self-
522 associate (Jiang et al., 2021) and form clusters that recruit CDK5RAP2 and ninein, two proteins known
523 to bind to pericentrin (Chen et al., 2014; Delaval and Doxsey, 2010; Kim and Rhee, 2014; Lawo et al.,
524 2012). CDK5RAP2 is important for efficient microtubule nucleation, consistent with its role as an
525 activator of γ-TuRC (Choi et al., 2010). The same may be true for pericentrin itself (Takahashi et al.,
526 2002) and, to a lesser extent, for ninein (Delgehyr et al., 2005; Mogensen et al., 2000), which was less
527 important for microtubule nucleation in our assays. Ninein might be required for promoting minus-
528 end anchoring, as proposed by previous studies (Abal et al., 2002; Chong et al., 2020; Delgehyr et al.,
529 2005; Goldspink et al., 2017; Lechler and Fuchs, 2007; Mogensen et al., 2000; Shinohara et al., 2013;
530 Zheng et al., 2020). The importance of ninein for the formation of caMTOCs highlights its function
531 within the PCM independent of its role at the centriolar appendages, a major site of ninein localization
532 at the centrosome (Chong et al., 2020; Delgehyr et al., 2005; Sonnen et al., 2012). Pericentrin can also
533 directly interact with dynein through the dynein light intermediate chain (Purohit et al., 1999). Ninein
534 was shown to form a triple complex with dynein and dynactin and activates dynein motility (Redwine
535 et al., 2017), and an interaction between CDK5RAP2 and dynein has also been reported (Jia et al.,
536 2013; Lee and Rhee, 2010). All these interactions likely contribute to dynein-dependent PCM
537 coalescence in the absence of centrioles and also to the function of PCM in microtubule organization,

538 as in the absence of PCM clustering, microtubule density is strongly reduced even though all PCM
539 proteins are expressed.

540 Pericentrin-dependent MTOC assembly has also been observed in acentriolar mitotic cells (Chinen et
541 al., 2021; Watanabe et al., 2020), but the interphase pathway displays some interesting differences.
542 Most notably, CEP192 and its binding partners CEP152 and NEDD1 (Gomez-Ferreria et al., 2012;
543 Joukov et al., 2014; Kim et al., 2013; Sonnen et al., 2013) were not enriched at caMTOCs, and their
544 depletion appeared to have no impact on caMTOC formation. This is surprising, because CEP192 is
545 essential for cell division (Gomez-Ferreria et al., 2007; Joukov et al., 2014; Yang and Feldman, 2015;
546 Zhu et al., 2008), and in acentriolar cells that rely on pericentrin and CDK5RAP2 for spindle pole
547 formation, CEP192 is recruited to mitotic pericentrin clusters (Chinen et al., 2021; Watanabe et al.,
548 2020). Moreover, although NEDD1 is targeted to centrosomes by CEP192, pericentrin can also
549 contribute to the centrosomal targeting of NEDD1 independently of CEP192 during mitosis (Chi et al.,
550 2021). However, our data indicate that in interphase, pericentrin and CEP192/NEDD1 are brought
551 together by centrioles. This conclusion is important for understanding MTOC assembly in
552 differentiated cells, where centrosome function is suppressed. Strikingly, pericentrin, ninein,
553 CDK5RAP2 and γ-TuRC are also present in non-centrosomal PCM-based MTOCs at the nuclear
554 envelope and the Golgi membranes in muscle cells, where they are targeted by AKAP450 (Gimpel et
555 al., 2017; Oddoux et al., 2013; Vergarajauregui et al., 2020). Recent work also demonstrated that at
556 the ciliary base of certain types of worm neurons, there is an acentriolar PCM-dependent MTOC that
557 is formed by the functional counterparts of CDK5RAP2 (SPD-5), pericentrin (PCMD-1) and γ-tubulin,
558 but lacks CEP192/SPD-2 (Garbrecht et al., 2021; Magescas et al., 2021). The co-assembly of
559 pericentrin, ninein and CDK5RAP2 counterparts into structures that can promote γ-TuRC-dependent
560 microtubule nucleation and also anchor minus ends may thus be a general property of interphase
561 PCM-dependent acentriolar MTOCs. Additionally, the participation of dynein is likely to be a general
562 feature of acentrosomal microtubule organization, as exemplified by MTOCs formed by the Golgi
563 apparatus or endosomal membranes (Liang et al., 2020; Zhu and Kaverina, 2013).

564 Our simple cellular system allowed us to dissect the molecular details of acentriolar PCM assemblies.
565 We found that caMTOCs recruited multiple MAPs and a subset of centriolar proteins. For example,
566 caMTOCs accumulated several +TIPs, such as CLASPs, CLIP170 and chTOG, though the depletion of
567 these proteins had no effect on caMTOC formation or function. In contrast, the core components of
568 the +TIP complexes, EB1 and EB3, were neither enriched in caMTOCs nor required for their assembly.
569 While the negative results on other +TIPs might be due to their incomplete depletion, EB1 and EB3
570 function was tested using genetic knockouts, indicating that interphase PCM function is EB-
571 independent. Among the centriolar proteins, we detected CPAP, CP110 and CEP120 in caMTOCs, and

572 it will be interesting to test whether any of these microtubule-binding factors contribute to
573 microtubule organization independently of their participation in centriole and centrosome assembly.

574 Furthermore, our work provided insight into the self-assembly properties of interphase PCM. It seems
575 that while oligomerization and clustering of pericentrin molecules is important for MTOC formation
576 both in interphase and in mitosis, during mitotic entry, pericentrin forms condensates (Jiang et al.,
577 2021), while in interphase, pericentrin clusters show no hallmarks of liquid droplets or condensates.
578 Moreover, the compaction and shape of these acentriolar PCM clusters depend on dynein and
579 microtubules. While caMTOCs were stable when all microtubules were disassembled, indicating that
580 attractive interactions between PCM components are sufficient to keep them together, cold
581 treatment experiments suggested that the cylindrical shape of caMTOCs is likely due to their
582 association with some stable microtubules. Furthermore, when the number of PCM-unattached stable
583 minus-end-out microtubules was increased by either nocodazole treatment or by the presence of
584 CAMSAP2, PCM clusters could no longer form a compact structure but continued to move along
585 microtubules. Therefore, an important outcome of our study is the key role of stabilized minus ends
586 in determining interphase PCM organization in the absence of the centrosome. This property may help
587 to explain how acentrosomal MTOCs form in cells where both PCM proteins and PCM-independent
588 microtubule stabilizers such as CAMSAPs are present. Two well studied examples of such systems are
589 the MTOCs at the Golgi membranes and the apical cortex of epithelial cells, where CAMSAPs and PCM
590 proteins are present simultaneously and may cooperate with each other or play redundant roles
591 (Goldspink et al., 2017; Nashchekin et al., 2016; Noordstra et al., 2016; Sanchez et al., 2021; Toya et
592 al., 2016; Wang et al., 2015; Wu et al., 2016; Zhu and Kaverina, 2013). We found that CAMSAP2-
593 stabilized minus ends can exert a highly dominant effect on PCM organization, and this property likely
594 explains how the Golgi, which anchors CAMSAP2-stabilized microtubules, recruits PCM and becomes
595 the major MTOC in cells lacking centrosomes. Importantly, our experiments and simulations showed
596 that coupling stable minus-ends to a minus-end directed motor is by itself insufficient to form a
597 compact MTOC, but self-clustering PCM can contribute to this process. Altogether, self-association of
598 interphase PCM appears to be strong enough to promote its clustering but is sufficiently dynamic to
599 allow PCM reorganization dependent on other microtubule regulators present in the cell.

600 An interesting question that remains unanswered by our work is the inhibitory role of PLK4 in
601 interphase caMTOC formation. We did observe caMTOCs in cells depleted of PLK4, indicating that,
602 unlike cells lacking TRIM37, which form PCM clusters containing catalytically inactive PLK4 (Meitinger
603 et al., 2020; Yeow et al., 2020), interphase cells studied here do not rely on enzymatically inactive PLK4
604 for PCM assembly. PLK4 is known to phosphorylate NEDD1 (Chi et al., 2021), and it is possible that the
605 lack of phosphorylation prevents this γ-TuRC activator and its partners, such as CEP192, from

606 participating in interphase caMTOC assembly. It is, of course, also possible that PLK4 phosphorylation
607 inhibits the interactions or activities of some of the players driving caMTOC formation. The easy-to-
608 manipulate cellular model that we have described here will allow these questions to be addressed and
609 facilitate detailed studies of the interactions and functions of PCM components in nucleating and
610 stabilizing interphase microtubule minus ends.

611 **Materials and Methods**

612 ***DNA constructs and protein purification***

613 To generate the lentiviral vector pLVX-GFP-CDK5RAP2-IRES-Puro, pLVX-IRES-Puro plasmid (Clontech)
614 was digested with AgeI and NotI (FastDigest, Thermo Fisher), and then Gibson Assembly (NEB) was
615 performed with gel-purified PCR product of GFP-CDK5RAP2 (Wu et al., 2016). To generate pB80-FRB-
616 TagBFP-GCN4-ppKin14 and pB80-FRB-HA-GCN4-ppKin14, pB80-FRB-GFP-GCN4-ppKin14-VIb was
617 digested with XbaI and BsrGI (FastDigest, Thermo Fisher), and then TagBFP and HA-tag encoding DNA
618 fragments were subcloned into the linearized vector by Gibson Assembly.

619 To generate the PX459 with single guide RNA (sgRNA) sequences, pSpCas9(BB)-2A-Puro (PX459) V2.0
620 (Ran et al., 2013)(purchased from Addgene) was digested with FastDigest BbsI (Thermo Fisher), and
621 the annealing product of single-strand sgRNA-encoding oligonucleotides was inserted into the linear
622 PX459 linear vector by T4 ligation (Thermo Fisher). The sgRNA sequences that were used in this study
623 are: sgRNA targeting AKAP450 5'- gAGGGTTACCTATGGGACTGA -3'; sgRNA targeting CAMSAP2
624 encoding gene 5'-gCATGATCGATACCCTCATGA-3'; sgRNA targeting p53-encoding gene exon 2 #1 5'-
625 gCGTCGAGCCCCCTCTGAGTC-3'; sgRNA targeting p53 exon 4 #2 5'-gCCATTGTTCAATATCGTCCG-3';
626 sgRNA targeting PCNT exon 5 #1 5'-gAGACGGCATTGACGGAGCTG-3'; sgRNA targeting pericentrin-
627 encoding gene exon 5 #2 5'-GCTCAACAGCCGGCGTGCCC-3'.

628 To generate the GST-DmKHC(1-421)-mNeonGreen construct used for protein purification for motor-
629 PAINT, the fragment containing amino acids 1 to 421 of the Drosophila melanogaster Kinesin Heavy
630 Chain (DmKHC) was amplified from donor construct DmKHC(1-421)-GFP-6x-His with a C-terminal
631 mNeonGreen tag by PCR and then cloned into a pGEX vector. The plasmid was transformed into *E. coli*
632 BL21 cells for purification. Bacteria were cultured until OD600 $\approx$0.7 and cultures were cooled prior to
633 inducing protein expression with 0.15 mM IPTG at 18°C overnight. Cells were then pelleted by
634 centrifugation, snap frozen in liquid nitrogen, and stored at -80°C until use. Cells were rapidly thawed
635 at 37°C before being resuspended in chilled lysis buffer (phosphate buffered saline (PBS)
636 supplemented with 5 mM $MgCl_2$, 0.5 mM ATP, 0.1% Tween 20, 250 mM NaCl, and 1x complete
637 protease inhibitor; pH 7.4). Bacteria were lysed by sonication (5 rounds of 30 s) and supplemented
638 with 5 mM DTT and 2mg/mL lysozyme and then incubated on ice for 45 min. The lysate was clarified
639 by centrifuging at 26000 xg for 30 minutes before being incubated with equilibrated Glutathione
640 Sepharose 4B resin for 1.75 hrs. Beads were then pelleted, resuspended in wash buffer (PBS
641 supplemented with 5 mM $MgCl_2$, 0.1% Tween 20, 250 mM NaCl, 1 mM DTT, and 0.5 mM ATP; pH 7.4),
642 and transferred to a BioRad column. Once settled, the resin was washed with 2 x 10 column volumes
643 (CV) wash buffer, followed by 1 x 10CV PreScission buffer (50 mM Tris-HCl, 5 mM $MgCl_2$, 100mM NaCl,

644 1 mM DTT, 0.5 mM ATP; pH 8.0). The resin was then incubated overnight in 4CV PreScission buffer
645 with 80U PreScission protease to cleave off the GST tag. The following morning, after allowing the
646 resin to settle, the eluent was collected, concentrated by spinning through a 3000kDa MWCO filter,
647 supplemented with an additional 0.1mM ATP, 1mM DTT, and 20% w/v sucrose before flash freezing
648 in liquid nitrogen, and finally stored at -80°C. Concentration was determined using a Nanodrop. All
649 steps from lysis onwards were performed at 4°C.

650

651 ***Cell culture and drug treatment***

652 hTERT immortalized RPE-1 (RPE1) cell lines were grown in an 1:1 mix of DMEM and F-10 (Lonza) and
653 Human Embryonic Kidney (HEK) 293T cells line were cultured in DMEM, both supplemented with 10%
654 fetal bovine serum (FBS, GE Healthcare) and 1% penicillin and streptomycin (Sigma-Aldrich). All cells
655 were grown in tissue culture polystyrene flasks (Corning) and were maintained in a humidified
656 incubator at 37°C with 5% CO_2. Mycoplasma contamination was routinely checked with LT07-518
657 Mycoalert assay (Lonza).

658 FuGENE 6 (Promega) was used to transfect RPE1 cells with plasmids for generating CRISPR/Cas9
659 knockouts, immunofluorescence staining and live cell imaging; RNAiMAX (Thermo Fisher Scientific)
660 was used to transfect RPE1 cells with siRNAs at 20 nM; MaxPEI was used to transfect HEK293T cells
661 for lentivirus packaging. Transfections were performed according to the manufacturer's instructions
662 within the recommended reagent/DNA or reagent/siRNA ratio range.

663 We used the following drugs: centrinone B (Tocris Bioscience), nocodazole (Sigma), rapalog (A/C
664 Heterodimerizer, Takara), dynapyrazole A (Sigma-Aldrich) , BI2536 (Selleckchem), Thymidine (Sigma-
665 Aldrich) , proTAME (Boston Biochem) and Brefeldin A (Peptrotech).

666 To remove centrioles, RPE1 cells were treated with 125 nM centrinone B containing complete medium
667 for ~10 days, and drug-containing medium was refreshed every 24 hrs; cell confluence was maintained
668 around ~50-80% during the treatment.

669 For the microtubule disassembly and regrowth assay, the acentriolar RPE1 cells were seeded onto
670 coverslips in 24-well plates and incubated for 24 hrs, then cells were treated with 10 µM nocodazole
671 for 1 hr in an incubator (37°C, 5% CO_2) and followed by another 1 hr treatment at 4°C to achieve
672 complete disassembly of stable microtubule fragments. Nocodazole washout was then carried out by
673 at least six washes on ice with ice-cold complete medium; subsequently, plates were moved to a 37°C
674 water bath and pre-warmed medium was added to each well to allow microtubule regrowth.

675 For cell cycle synchronization, centrinone-treated AKAP450/CAMSAP2/P53 knockout cells were
676 treated with 5 mM Thymidine (Sigma-Aldrich) overnight, released in centrinone containing medium
677 for 4 hrs and subsequently treated with 5µM proTAME (Boston Biochem, I-440) for 2 hrs before being
678 released in centrinone containing medium for 1-4 hrs followed by live imaging and fixation.

679 For the inducible ppKin14-CAMSAP2 heterodimerization experiment, acentriolar cells were seeded
680 onto coverslips in 24-well plates, cultured with centrinone B containing medium and co-transfected
681 with 2FKBP-mCherry-CAMSAP2 and FRB-TagBFP-GCN4-ppKin14 vectors. 24 hrs after transfection,
682 rapalog was added into the medium at a final concentration of 50 nM and incubated overnight for
683 preparation of fixed cells. For live imaging, rapalog was used at 100 nM.

684

685 ***Lentivirus packaging and generation of transgenic stable cell lines***

686 Lentiviruses were produced by MaxPEI-based co-transfection of HEK293T cells with the transfer
687 vectors together with the packaging vector psPAX2 and envelope vector pMD2.G (psPAX2 and
688 pMD2.G were a gift from Didier Trono, Addgene plasmid #12259 and #12260; RRID:Addgene_12259
689 and RRID:Addgene_12260). Supernatant of packaging cells was harvested 48-72 hrs after transfection,
690 filtered through a 0.45 µm filter, incubated with a polyethylene glycol (PEG)-6000-based precipitation
691 solution overnight at 4°C and centrifuged for 30 minutes at 1500 rpm to concentrate the virus.
692 Lentiviral pellet was resuspended in PBS.

693 Wild type, AKAP450 and AKAP450/CAMSAP2 knockout RPE1 cells were infected with lentivirus and
694 incubated in complete medium supplemented with 8 µg/ml polybrene (Sigma-Aldrich). After 24 hrs,
695 the cell medium was replaced with fresh medium. Starting 72 hrs after viral transduction, cells were
696 subjected to selection with puromycin at a concentration of 25 µg/ml for wild-type, 20 µg/ml for
697 AKAP450 knockout and 15 µg/ml for AKAP450/CASMAP2 knockout for up to 3 days (until most of the
698 untransduced control cells, treated with the same concentration of antibiotic, were dead). After
699 selection, cells were grown in normal medium for 3 days and individual colonies expressing GFP were
700 isolated into 96-well plates by fluorescence-activated cell sorting (FACS). Sorted single transgenic
701 stable cell lines were further confirmed by immunofluorescence staining to check the expression level
702 of GFP-CDK5RAP2 and its colocalization with other centrosomal proteins.

703

704 ***Generation of CRIPSR/Cas9 knockout cell lines***

705 The CRISPR/Cas9-mediated knockout of p53-, pericentrin-, AKAP450- and CAMSAP2-encoding genes
706 was performed as described previously (Ran et al., 2013). In brief, AKAP450/CAMSAP2 knockout RPE1

707 cells (Wu et al., 2016) were transfected with the vectors bearing the appropriate targeting sequences
708 using FuGENE 6. One day after transfection, the transfected AKAP450/CAMSAP2 knockout RPE1 cells
709 were subjected to selection with 15 µg/ml puromycin for up to 3 days. After selection, cells were
710 allowed to recover in normal medium for ∼7 days, and knockout efficiency was checked by
711 immunofluorescence staining. Depending on the efficiency, 50–500 individual clones were isolated
712 and confirmed by immunofluorescence staining, and the resulted single colonies were characterized
713 by Western blotting, immunostaining and genome sequencing. AKAP450/CAMSAP2/p53 and
714 AKAP450/CAMSAP2/MMG/CDK5RAP2/p53 knockout cell lines were generated first and subsequently,
715 each of them was used to knock out the gene encoding pericentrin. The mutated portions of the p53-
716 and pericentrin-encoding genes were sequenced using gel-purified PCR products obtained with
717 primers located in the vicinity of the corresponding sgRNA targeting sites.

718

719 ***Antibodies, immunofluorescence staining and Western blotting***

720 Antibodies used for immunostaining and Western blotting are listed in the Key Reagent or Resource
721 table. For immunofluorescence cell staining, cultured cells were fixed with –20°C methanol for 5 min
722 or with 4% paraformaldehyde (PFA) for 12 min at room temperature, rinsed in PBS for 5 min,
723 permeabilized with 0.15% Triton X-100 in PBS for 2 min, washed 3 times for 5 min with 0.05% Tween-
724 20 in PBS, sequentially incubated for 20 min in the blocking buffer (2% BSA and 0.05% Tween-20 in
725 PBS), 1 hr with primary antibodies in the blocking buffer, washed 3 times for 5 min with 0.05% Tween-
726 20 in PBS, then for 1 hr in secondary antibodies in the blocking buffer, washed 3 times for 5 min with
727 0.05% Tween-20 in PBS, and air-dried after a quick wash in 96% ethanol. Cells were mounted in
728 Vectashield mounting medium with or without DAPI (Vector laboratories, Burlingame, CA). Alexa Fluor
729 -405, -488, –594 and −647 conjugated goat antibodies against rabbit, rat and mouse IgG were used as
730 secondary antibodies (Molecular Probes, Eugene, OR).

731 For Western blotting, cells were harvested from six-well plates or 10 cm dishes at 90% confluence and
732 protein extracts were prepared using the lysis buffer containing 20 mM Tris-Cl, pH 7.5, 150 mM NaCl,
733 0.5 mM EDTA, 1 mM DTT, 1% Triton X-100 or RIPA buffer containing 50 mM Tris-HCl, pH 7.5, 150 mM
734 NaCl, 1% Triton X-100, 0.5% Sodium Deoxycholate supplemented with protease inhibitor and
735 phosphatase inhibitors (Roche). Samples were run on polyacrylamide gels, followed by transfer on
736 0.45 µm nitrocellulose membrane (Sigma-Aldrich). Blocking was performed in 2% BSA in PBS for 30
737 min at room temperature. The membrane was first incubated with the primary antibodies overnight
738 at 4°C and washed with 0.05% Tween-20 in PBS 3 times and subsequently incubated with secondary
739 antibodies for 1 hr at room temperature and washed 3 times with 0.05% Tween-20 in PBS. IRDye

740 800CW/680 LT Goat anti-rabbit and anti-mouse were used as secondary antibodies (Li-Cor
741 Biosciences, Lincoln, LE) and membranes were imaged on Odyssey CLx infrared imaging system (Image
742 Studio version 5.2.5, Li-Cor Biosciences).

743

744 ***Imaging and analysis of fixed cells***

745 Images of fixed cells were collected with a Nikon Eclipse Ni upright fluorescence microscope equipped
746 with a DS-Qi2 CMOS camera (Nikon), an Intensilight C-HGFI epi-fluorescence illuminator (Nikon), Plan
747 Apo Lambda 100× NA 1.45 or Plan Apo Lambda 60x N.A. 1.40 oil objectives (Nikon) and driven by NIS-
748 Elements Br software (Nikon).

749 Gated STED imaging was performed with Leica TCS SP8 STED 3X microscope driven by LAS X software
750 using HC PL APO 100x/1.4 oil STED WHITE objective, white laser (633 nm) for excitation and 775 nm
751 pulsed lased for depletion. Images were acquired in 2D STED mode with vortex phase mask. Depletion
752 laser power was equal to 90% of maximum power and an internal Leica HyD hybrid detector with a
753 time gate of $1 \leqslant tg \leqslant 8$ ns was used.

754 ImageJ was used for adjustments of intensity levels and contrast, quantification of the
755 immunofluorescence signal intensity and maximum intensity projections. To analyze PCM clustering
756 after nocodazole washout in AKAP450/CAMSAP2 knockout RPE1 cells, images were separated into
757 concentric circular areas using Concentric Circles plugin of ImageJ. The biggest PCM cluster (which
758 normally also had the highest fluorescence intensity) was selected as the center, around which 20
759 circles with 2 µm inner radius and 20 µm outer radius were drawn. Fluorescence intensity of PCM
760 clusters in these concentric circles was measured automatically and normalized by the sum of the total
761 PCM intensity in each cell per condition. To quantify the areas occupied by PCM clusters,
762 immunofluorescence images of fixed cells and time lapse images of live cells were analyzed by drawing
763 the smallest circle that covered visible PCM clusters to indicate the area occupied by the PCM clusters,
764 and the diameters of the circles were used for the quantification.

765

766 ***Measurements of microtubule radiality***

767 To analyze microtubule radiality, images of fluorescently labeled microtubules were separated into
768 radial and non-radial components using a customized ImageJ macro
769 (https://github.com/ekatrukha/radialitymap). First, a local orientation angle map was calculated for
770 each pixel using the OrientationJ plugin. We used 'cubic spline gradient' method and tensor sigma

771 parameter of 6 pixels (0.4 µm). The new origin of coordinates was specified by selecting the
772 centrosome position in the corresponding channel, or the brightest spot in case of centrinone
773 treatment. Radial local orientation angle was calculated as a difference between the local orientation
774 angle and the angle of the vector drawn from the new origin of coordinates to the current pixel
775 position. A radial map image was calculated as an absolute value of the cosine of the radial local
776 orientation angle at each pixel providing values between zero and one. A non-radial map image was
777 calculated as one minus the radial map. Both maps were multiplied with the original image to account
778 for different signal intensities; the two maps illustrate separated radial and non-radial image
779 components.

780

781 ***Live cell imaging and analysis***

782 Live fluorescent imaging was performed with spinning disk confocal microscopy on inverted research
783 microscope Nikon EclipseTi-E (Nikon), equipped with the Perfect Focus System (Nikon), Nikon Plan
784 Apo VC 60x NA 1.4 and Nikon Plan Apo VC 100x N.A. 1.40 oil objectives (Nikon) and spinning-disc
785 confocal scanner unit (CSU-X1-A1, Yokogawa). The system was also equipped with ASI motorized stage
786 with the piezo top plate MS-2000-XYZ (ASI), Photometrics Evolve 512 EMCCD camera (Photometrics)
787 and controlled by the MetaMorph 7.8 software (Molecular Devices). Vortran Stradus lasers (405 nm
788 100 mW, 488 nm 150 mW and 642 nm 165 mW) and Cobolt Jive 561 nm 110 mW laser were used as
789 the light sources. System was equipped with ET-DAPI (49000), ET-GFP (49002), ET-mCherry (49008)
790 and ET-Cy5 (49006) filter sets (Chroma). 16-bit images were projected onto the EMCCD chip with the
791 intermediate lens 2.0X (Edmund Optics) at a magnification of 110 nm per pixel (60x objective) and 67
792 nm per pixel (100x objective). To keep cells at 37°C and 5% CO_2 we used stage top incubator (INUBG2E-
793 ZILCS, Tokai Hit). Cells were plated on round 25 mm coverslips, which were mounted in Attofluor Cell
794 Chamber (Thermo fisher). Cells were imaged with a 2 s interval and 200 ms exposure for 1-3 hrs at
795 10% laser power.

796 Phase-contrast live cell imaging was performed on a Nikon Ti equipped with a perfect focus system
797 (Nikon), a super high pressure mercury lamp (C-SHG1, Nikon, Japan), a Plan Apo 60x NA 1.4 (Ph3), a
798 CoolSNAP HQ2 CCD camera (Photometrics, Tucson, AZ), a motorized stage MS-2000-XYZ with Piezo
799 Top Plate (ASI, Eugene, OR) and a stage top incubator (Tokai Hit, Japan) for 37°C/5% CO2 incubation.
800 The microscope setup was controlled by Micro-manager software. Cells were plated on round 25 mm
801 coverslips, which were mounted in Attofluor Cell Chamber (Thermo fisher), and imaged with a 1 min
802 interval for ~24 hrs.

803 For live imaging of nocodazole treatment and washout experiments, cells were incubated with the
804 medium containing 100 nM SiR-tubulin (Tebu-bio) overnight to image the microtubule network.
805 Centrinone-treated cells were imaged for a desired period of time prior to the nocodazole treatment,
806 and then nocodazole was added into the medium at a final concentration of 10 µM while imaging
807 simultaneously. Culture medium was carefully removed when microtubules were completely
808 depolymerized and washed with prewarmed medium six times to let microtubules regrow. GFP-
809 CDK5RAP2 and SiR-tubulin imaging was performed with a 2 s interval with 200 ms exposure for 1-3
810 hrs in total, and maximum intensity projections, contrast adjustment and further processing was
811 performed using ImageJ.

812

813 ***FRAP***

814 FRAP experiments were performed on the spinning disc microscope describe above, equipped with
815 iLas platform and using Targeted Laser Action options of iLas and controlled with iLas software (Roper
816 Scientific, now Gataca Systems). Photobleaching in the GFP channel was performed with the 488 nm
817 laser. For the FRAP analysis, Polygon ROIs were set in photobleached and non-bleached regions as
818 well as in the background. The average fluorescence intensity was measured using ImageJ for each
819 frame, the background intensity was subtracted from the bleached and non-bleached areas and
820 normalized to the average of the frames acquired prior to the bleach. The mean fluorescence
821 intensities of the images before photobleaching were set as 100%, and the subsequent relative
822 recovery percentages were calculated. Time lapse acquisitions were corrected for drift with the
823 ImageJ plugins Template Matching.

824

825 ***motor-PAINT and analysis***

826 For motor-PAINT, a protocol published previously (Tas et al., 2017) was used, with minor adjustments.
827 Cells were incubated with 50 nM SiR-tubulin and 500 nM verapamil overnight to allow fields of view
828 suitable for imaging to be located before the addition of purified GST-DmKHC(1-421)-mNeonGreen.
829 For nocodazole-treated samples, cells were first incubated with 10 µM nocodazole for 15 minutes at
830 37°C. A single nocodazole-treated or control sample was then transferred to an imaging chamber, and
831 cells were subjected to extraction for 1 minute in extraction buffer (BRB80: 80 mM K-Pipes, 1 mM
832 $MgCl_2$, 1 mM EGTA; pH 6.8, supplemented with 1M sucrose and 0.15% TritonX-100) pre-warmed to
833 37°C. Pre-warmed fixation buffer (BRB80 supplemented with 2% PFA) was added to this (i.e. final PFA
834 concentration of 1%) and the solutions were mixed by gentle pipetting for 1 minute. This buffer was

835 removed and the chamber was washed for 4 times for 1 minute in pre-warmed wash buffer (BRB80
836 supplemented with 1 µM Taxol) before adding imaging buffer (BRB80 supplemented with 583 µg/mL
837 catalase, 42 µg/mL glucose oxidase, 1.7% w/v glucose, 1 mM DTT, 1 µM Taxol, and 5mM ATP). An
838 aliquot of GST-DmKHC(1-421)-mNeonGreen motors was warmed, spun in the Airfuge at 20 psi for 5
839 minutes in a pre-chilled rotor to remove any aggregates, and then transferred to a clean tube prior to
840 use. Motors were kept on ice and added locally to cells in 0.3 µl increments.

841 Imaging was performed immediately after sample preparation at room temperature on a Nikon Ti-E
842 microscope equipped with a 100x Apo TIRF oil immersion objective (NA. 1.49) and Perfect Focus
843 System 3 (Nikon). Excitation was achieved with a Lighthub-6 laser combiner (Omicron) containing a
844 647 nm laser (LuxX 140 mW, Omicron), a 488 nm laser (LuxX 200 mW, Omicron), and optics allowing
845 for a tunable angle of incidence. Illumination was adjusted for (pseudo-) total internal reflection
846 fluorescence (TIRF) microscopy. Emission light was separated from excitation light using a quad-band
847 polychroic mirror (ZT405/488/561/640rpc, Chroma), a quad-band emission filter
848 (ZET405/488/561/640m, Chroma), and an additional single-band emission filter (ET525/50m for
849 mNeonGreen emission, Chroma). Detection was achieved using a Hamamatsu Flash 4.0v2 sCMOS
850 camera. Image stacks were acquired with a 60 ms exposure time, 7% laser power, and 15000-22000
851 images per field of view. Components were controlled using MicroManager (Edelstein et al., 2014).

852 Acquired stacks were pre-processed using the Faster Temporal Median ImageJ plugin
853 (https://github.com/HohlbeinLab/FTM2; (Jabermoradi et al., 2021)) with a window size of 100 frames.
854 These stacks were then analyzed using Detection of Molecules (DoM) plugin v.1.2.1 for ImageJ
855 (https://github.com/ekatrukha/DoM_Utrecht), as has been described previously (Chazeau et al.,
856 2016; Tas et al., 2017). Each image in an acquired stack is convoluted with a two-dimensional Mexican
857 hat kernel. The resulting intensity histogram is used to create a thresholded mask based on a cut-off
858 of three standard deviations above the mean. This mask is then subject to rounds of dilution and
859 erosion to create a filtered mask used to calculate the centroids on the original image. These centroids
860 are used as initial values to perform unweighted nonlinear least squares fitting with a Levenberg-
861 Marquardt algorithm to an asymmetric two-dimensional Gaussian point spread function (PSF),
862 allowing for the sub-pixel localization of particles.

863 Images were drift-corrected using DoM. The normalized cross-correlation between intermediate
864 reconstructions of consecutive sub-stacks is used to calculate the drift in x and y between sub-stacks,
865 which is then linearly interpolated to adjust each individual frame in the stack.

866 Detected particles were linked into tracks again using DoM, which performs a quicker variant of a
867 nearest neighbor search, with a maximum distance of 5 pixels (~320nm) between consecutive frames

868 and no permitted frame gap. Tracks were later filtered to remove those shorter than 4 frames or
869 longer than 200 frames, those in which an angle between parts of the trajectory exceeded 90 degrees,
870 and those in which the speed of the motor was less than 100nm/s or more than 1500nm/s.

871 The particle table was then split into four particle tables corresponding to the four quadrants of the
872 image with tracks sorted based on their net displacement (i.e., $\Delta x>0 \wedge \Delta y>0$; $\Delta x>0 \wedge \Delta y<0$; Δ
873 $x<0 \wedge \Delta y>0$; $\Delta x<0 \wedge \Delta y<0$), as described previously (Tas et al., 2017). These directionality-filtered
874 particle tables were reconstructed using DoM, creating four super-resolved images of microtubule
875 segments pointing in a similar direction. These were merged with the reconstructed image of all
876 localizations to determine the direction of each microtubule segment. Each microtubule was manually
877 assessed to assign it as being plus-end-in or plus-end-out. Microtubules were manually traced with
878 lines 4 pixels (80 nm) wide, assigned a color based on their orientation, flattened onto the image,
879 filtered with a Gaussian Blur of radius 2, and finally merged with the reconstructed image of all
880 localizations.

881 To quantify the percentage of minus-end-out microtubule length to total microtubule length before
882 and after nocodazole treatment, the length of each microtubule (determined from kinesin-1
883 trajectories) in the cell was measured by calculating the Euclidean distance between all subsequent
884 pairs of points along the microtubule and summed. The ratio was calculated as the total minus-end-
885 out microtubule length divided by the total microtubule length.

886

887 ***Analysis of PCM cluster dynamics***

888 To represent the motion of PCM clusters during nocodazole treatment, ImageJ plugin
889 KymoResliceWide v.0.4 (https://github.com/ekatrukha/KymoResliceWide) was used for generating
890 kymographs from the time lapse images. The velocity of PCM clusters was measured manually using
891 kymographs starting from the time point when a small PCM cluster moved out of a caMTOC.
892 Microtubule density around each PCM cluster was determined by measuring the mean fluorescence
893 intensity of SiR-tubulin in a circular area with a 2 µm radius centered on the PCM cluster and
894 normalizing it to the mean fluorescence intensity of 20 images prior to nocodazole addition (set as
895 100%). The moment when a PCM cluster started to move out of the caMTOC was set as the initial time
896 point (0 min), and the subsequent PCM cluster motion velocity and the relative local microtubule
897 density at 43 time points were calculated and averaged.

898 The movement trajectories of PCM clusters were generated using ImageJ plugin TrackMate (version
899 is 6.0.2). The parameters and the settings used were as following: LoG (Laplacian of Gaussian) detector

900 with estimated blob diameter: 14.9 µm; thresholding value 12.25; sub-pixel localization was selected.
901 HyperStack Displayer was selected to overlay the spots and tracks on the current hyperstack window.
902 Simple LAP tracker was selected to track the distance and time with the linking max distance: 32.0 µm,
903 gap-closing max distance: 55.0 µm and gap-closing max frame gap: 2. All other parameters and
904 settings were used as the default.

905

906 ***Computer simulations and analysis***

907 Simulations were performed with Cytosim (version June 2019). Cytosim solves a set of Langevin-
908 equations that describe the movement of flexible cytoskeletal filaments and associated proteins, such
909 as molecular motors (Nedelec and Foethke, 2007). The numerical values for the parameters are given
910 in Table S1. The configuration file is provided as Supplemental file 1.

911 We defined the following components in the simulation:

912 *Cell shape:* We considered a two-dimensional system with a circular cell with a radius of 10 µm. As
913 commonly used in Cytosim simulations, we set the intracellular viscosity to 1 pN s/ μm^2.

914 *Molecular motors:* The binding process of a molecular motor to a microtubule was described by a
915 binding rate k_{on} and the unbinding from the microtubule by a force-dependent unbinding rate k_{off} =
916 $k^0_{off} \exp(F/F_d)$. When a motor was engaged with the microtubule it moved along the microtubule with
917 a linear force-dependent velocity, characterized by $v(F) = v_0 (1 - F/F_s)$. Dynein, as well as kinesin-14
918 motors moved to the minus end of microtubules.

919 *Microtubule filaments:* We used a classical model for microtubule dynamics which is described by a
920 catastrophe rate, a growth speed, and a shrinkage speed. The growth speed is force-dependent with
921 a characteristic growing force. For simplicity, we ignored rescue events. The catastrophe rate was set
922 as $k_{cat} = v_g/L_{MT}$, in which the mean microtubule length L_{MT} was 5 µm. To further restrict the microtubule
923 length, we set a maximum of 7.5 µm. This limitation was necessary to avoid that long microtubules
924 were pushing the minus ends to the periphery.

925 *PCM complexes*: We described a PCM complex as a bead with a radius of 50 nm. We randomly placed
926 one microtubule nucleation site and one dynein on the bead. To effectively account for an unspecific
927 adhesive interaction between PCM complexes, we introduced two molecules that can bind to each
928 other. One was implemented as a 10 nm Cytosim fiber and the binding partner as a Cytosim hand with
929 a binding range of 100 nm, binding rate of 10 s^{-1}, force-free unbinding rate of 0.01 s^{-1}, and
930 characteristic unbinding force of 3 pN. We randomly placed one of each molecule on a PCM complex.
931 In the simulations with strong adhesive interactions, we increased the number of adhesive binding

932 molecules on the beads and kept all the other parameters the same. We defined five random
933 attachment points on the beads and placed to each point five molecules. In this setup each PCM
934 complex was covered with 25 Cytosim binding filaments and 25 Cytosim binding hands. Therefore,
935 when two PCM complexes were close to each they formed multiple bonds between each other.

936 *CAMSAP-kin14 complexes:* We described a complex consisting of a CAMSAP-stabilized microtubule
937 end with kinesin 14 motors attached as a Cytosim bead with a radius of 50 nm. We attached five kin14
938 motors and one microtubule nucleation site randomly on the bead. When we implemented adhesive
939 interaction between CAMSAP-kin14 complexes, we used exactly the same binding molecules and
940 arrangements as used for the PCM complexes.

941 *Steric interactions:* In all simulations, we considered steric interaction between the beads which either
942 describe the PCM complex or the CAMSAP-kin14 complexes. All other steric interactions, except with
943 the cell boundary were ignored.

944 *Simulations and data analysis:* We set the time step for the simulation to 0.01 s and simulated for a
945 total of 30 min, after which a definite steady state was reached. For each configuration, we run 10
946 simulations and analyzed them afterward to obtain statistics on the emerging structures. From the
947 last frame of the simulation, we obtained all positions of the complexes and calculated the mean
948 position, which defines the center of mass. We subtracted the center of mass from all positions and
949 derived all distances of the complexes to the center of mass. For a few examples, we determined the
950 empirical cumulative distribution of the distances to the center of mass. We used the standard NumPy
951 functions to determine the mean and standard deviation of the distances to the center of mass for
952 each simulation.

953

954 ***Statistical analysis***

955 All statistical analyses were performed using GraphPad Prism 9. Statistical details for each experiment
956 can be found in the corresponding figure legends and supporting files.

957

958 ***Data and software availability***

959 All mentioned ImageJ plugins have source code available and are licensed under open-source GNU
960 GPL v3 license. The source data for the original Western blots are available within the paper.

961

Acknowledgements

We thank Lynne Cassimeris (Lehigh University, USA), Pierre Gönczy and Didier Trono (EPFL, Switzerland), Dr. Duane Compton (Geisel School of Medicine at Dartmouth, USA) and Dr. Laurence Pelletier (Lunenfeld-Tanenbaum Research Institute, Canada) for the gift of materials and Ilya Grigoriev and Eugene Katrukha (Biology Imaging Center, Utrecht University) for the help with imaging and image analysis. This work was supported by China Scholarship Council scholarships to Fangrui Chen, Jingchao Wu and Chao Yang, the Netherlands Organization for Scientific Research Spinoza prize to A.A, as well as the European Research Council Consolidator Grant 819219 to L.C.K. and the Eindhoven-Wageningen-Utrecht Alliance (www.ewuu.nl) that supports the Center for Living Technologies.

Competing financial interests

The authors declare no competing financial interests.

975 **References**

976 Abal, M., M. Piel, V. Bouckson-Castaing, M. Mogensen, J.B. Sibarita, and M. Bornens. 2002.
977 Microtubule release from the centrosome in migrating cells. *J Cell Biol*. 159:731-737.
978 Akhmanova, A., C.C. Hoogenraad, K. Drabek, T. Stepanova, B. Dortland, T. Verkerk, W. Vermeulen,
979 B.M. Burgering, C.I. De Zeeuw, F. Grosveld, and N. Galjart. 2001. Clasps are CLIP-115 and -
980 170 associating proteins involved in the regional regulation of microtubule dynamics in
981 motile fibroblasts. *Cell*. 104:923-935.
982 Balczon, R., C.E. Varden, and T.A. Schroer. 1999. Role for microtubules in centrosome doubling in
983 Chinese hamster ovary cells. *Cell Motil Cytoskeleton*. 42:60-72.
984 Balestra, F.R., A. Dominguez-Calvo, B. Wolf, C. Busso, A. Buff, T. Averink, M. Lipsanen-Nyman, P.
985 Huertas, R.M. Rios, and P. Gonczy. 2021. TRIM37 prevents formation of centriolar protein
986 assemblies by regulating Centrobin. *Elife*. 10:e62640.
987 Belyy, V., M.A. Schlager, H. Foster, A.E. Reimer, A.P. Carter, and A. Yildiz. 2016. The mammalian
988 dynein-dynactin complex is a strong opponent to kinesin in a tug-of-war competition. *Nat*
989 *Cell Biol*. 18:1018-1024.
990 Berger, F., S. Klumpp, and R. Lipowsky. 2019. Force-Dependent Unbinding Rate of Molecular Motors
991 from Stationary Optical Trap Data. *Nano Lett*. 19:2598-2602.
992 Brenner, S., F. Berger, L. Rao, M.P. Nicholas, and A. Gennerich. 2020. Force production of human
993 cytoplasmic dynein is limited by its processivity. *Sci Adv*. 6:eaaz4295.
994 Burakov, A., O. Kovalenko, I. Semenova, O. Zhapparova, E. Nadezhdina, and V. Rodionov. 2008.
995 Cytoplasmic dynein is involved in the retention of microtubules at the centrosome in
996 interphase cells. *Traffic*. 9:472-480.
997 Burakov, A., E. Nadezhdina, B. Slepchenko, and V. Rodionov. 2003. Centrosome positioning in
998 interphase cells. *J Cell Biol*. 162:963-969.
999 Carter, N.J., and R.A. Cross. 2005. Mechanics of the kinesin step. *Nature*. 435:308-312.
1000 Cassimeris, L., and J. Morabito. 2004. TOGp, the human homolog of XMAP215/Dis1, is required for
1001 centrosome integrity, spindle pole organization, and bipolar spindle assembly. *Mol Biol Cell*.
1002 15:1580-1590.
1003 Charrasse, S., M. Schroeder, C. Gauthier-Rouviere, F. Ango, L. Cassimeris, D.L. Gard, and C. Larroque.
1004 1998. The TOGp protein is a new human microtubule-associated protein homologous to the
1005 Xenopus XMAP215. *J Cell Sci*. 111 (Pt 10):1371-1383.
1006 Chazeau, A., E.A. Katrukha, C.C. Hoogenraad, and L.C. Kapitein. 2016. Studying neuronal microtubule
1007 organization and microtubule-associated proteins using single molecule localization
1008 microscopy. *Methods Cell Biol*. 131:127-149.
1009 Chen, C.T., H. Hehnly, Q. Yu, D. Farkas, G. Zheng, S.D. Redick, H.F. Hung, R. Samtani, A. Jurczyk, S.
1010 Akbarian, C. Wise, A. Jackson, M. Bober, Y. Guo, C. Lo, and S. Doxsey. 2014. A unique set of
1011 centrosome proteins requires pericentrin for spindle-pole localization and spindle
1012 orientation. *Curr Biol*. 24:2327-2334.
1013 Chi, W., G. Wang, G. Xin, Q. Jiang, and C. Zhang. 2021. PLK4-phosphorylated NEDD1 facilitates
1014 cartwheel assembly and centriole biogenesis initiations. *J Cell Biol*. 220:e202002151.
1015 Chinen, T., S. Yamamoto, Y. Takeda, K. Watanabe, K. Kuroki, K. Hashimoto, D. Takao, and D.
1016 Kitagawa. 2020. NuMA assemblies organize microtubule asters to establish spindle bipolarity
1017 in acentrosomal human cells. *EMBO J*. 39:e102378.
1018 Chinen, T., K. Yamazaki, K. Hashimoto, K. Fujii, K. Watanabe, Y. Takeda, S. Yamamoto, Y. Nozaki, Y.
1019 Tsuchiya, D. Takao, and D. Kitagawa. 2021. Centriole and PCM cooperatively recruit CEP192
1020 to spindle poles to promote bipolar spindle assembly. *J Cell Biol*. 220:e202006085.
1021 Choi, Y.K., P. Liu, S.K. Sze, C. Dai, and R.Z. Qi. 2010. CDK5RAP2 stimulates microtubule nucleation by
1022 the gamma-tubulin ring complex. *J Cell Biol*. 191:1089-1095.

1023 Chong, W.M., W.J. Wang, C.H. Lo, T.Y. Chiu, T.J. Chang, Y.P. Liu, B. Tanos, G. Mazo, M.B. Tsou, W.N.
1024 Jane, T.T. Yang, and J.C. Liao. 2020. Super-resolution microscopy reveals coupling between
1025 mammalian centriole subdistal appendages and distal appendages. *Elife*. 9:e53580.
1026 Cizmecioglu, O., M. Arnold, R. Bahtz, F. Settele, L. Ehret, U. Haselmann-Weiss, C. Antony, and I.
1027 Hoffmann. 2010. Cep152 acts as a scaffold for recruitment of Plk4 and CPAP to the
1028 centrosome. *Journal of Cell Biology*. 191:731-739.
1029 Conduit, P.T., A. Wainman, and J.W. Raff. 2015. Centrosome function and assembly in animal cells.
1030 *Nat Rev Mol Cell Biol*. 16:611-624.
1031 Cytrynbaum, E.N., V. Rodionov, and A. Mogilner. 2004. Computational model of dynein-dependent
1032 self-organization of microtubule asters. *J Cell Sci*. 117:1381-1397.
1033 Delaval, B., and S.J. Doxsey. 2010. Pericentrin in cellular function and disease. *J Cell Biol*. 188:181-
1034 190.
1035 Delgehyr, N., J. Sillibourne, and M. Bornens. 2005. Microtubule nucleation and anchoring at the
1036 centrosome are independent processes linked by ninein function. *J Cell Sci*. 118:1565-1575.
1037 Dogterom, M., and B. Yurke. 1997. Measurement of the force-velocity relation for growing
1038 microtubules. *Science*. 278:856-860.
1039 Edelstein, A.D., M.A. Tsuchida, N. Amodaj, H. Pinkard, R.D. Vale, and N. Stuurman. 2014. Advanced
1040 methods of microscope control using muManager software. *J Biol Methods*. 1:e10.
1041 Efimov, A., A. Kharitonov, N. Efimova, J. Loncarek, P.M. Miller, N. Andreyeva, P. Gleeson, N. Galjart,
1042 A.R. Maia, I.X. McLeod, J.R. Yates, 3rd, H. Maiato, A. Khodjakov, A. Akhmanova, and I.
1043 Kaverina. 2007. Asymmetric CLASP-dependent nucleation of noncentrosomal microtubules
1044 at the trans-Golgi network. *Dev Cell*. 12:917-930.
1045 Fong, C.S., G. Mazo, T. Das, J. Goodman, M. Kim, B.P. O'Rourke, D. Izquierdo, and M.F. Tsou. 2016.
1046 53BP1 and USP28 mediate p53-dependent cell cycle arrest in response to centrosome loss
1047 and prolonged mitosis. *Elife*. 5:e16270.
1048 Fong, K.W., Y.K. Choi, J.B. Rattner, and R.Z. Qi. 2008. CDK5RAP2 is a pericentriolar protein that
1049 functions in centrosomal attachment of the gamma-tubulin ring complex. *Mol Biol Cell*.
1050 19:115-125.
1051 Fu, J.Y., and D.M. Glover. 2012. Structured illumination of the interface between centriole and peri-
1052 centriolar material. *Open Biology*. 2:120104.
1053 Ganem, N.J., and D.A. Compton. 2004. The KinI kinesin Kif2a is required for bipolar spindle assembly
1054 through a functional relationship with MCAK. *J Cell Biol*. 166:473-478.
1055 Ganem, N.J., K. Upton, and D.A. Compton. 2005. Efficient mitosis in human cells lacking poleward
1056 microtubule flux. *Curr Biol*. 15:1827-1832.
1057 Garbrecht, J., T. Laos, E. Holzer, M. Dillinger, and A. Dammermann. 2021. An acentriolar centrosome
1058 at the C. elegans ciliary base. *Curr Biol*. 31:2418-2428.
1059 Gartenmann, L., C.C. Vicente, A. Wainman, Z.A. Novak, B. Sieber, J.H. Richens, and J.W. Raff. 2020.
1060 Drosophila Sas-6, Ana2 and Sas-4 self-organise into macromolecular structures that can be
1061 used to probe centriole and centrosome assembly. *J Cell Sci*. 133:jcs244574.
1062 Gavilan, M.P., P. Gandolfo, F.R. Balestra, F. Arias, M. Bornens, and R.M. Rios. 2018. The dual role of
1063 the centrosome in organizing the microtubule network in interphase. *EMBO Rep*. 19:e45942.
1064 Gibeaux, R., A.Z. Politi, P. Philippsen, and F. Nedelec. 2017. Mechanism of nuclear movements in a
1065 multinucleated cell. *Mol Biol Cell*. 28:645-660.
1066 Gimpel, P., Y.L. Lee, R.M. Sobota, A. Calvi, V. Koullourou, R. Patel, K. Mamchaoui, F. Nedelec, S.
1067 Shackleton, J. Schmoranzer, B. Burke, B. Cadot, and E.R. Gomes. 2017. Nesprin-1alpha-
1068 Dependent Microtubule Nucleation from the Nuclear Envelope via Akap450 Is Necessary for
1069 Nuclear Positioning in Muscle Cells. *Curr Biol*. 27:2999-3009.
1070 Goldspink, D.A., C. Rookyard, B.J. Tyrrell, J. Gadsby, J. Perkins, E.K. Lund, N. Galjart, P. Thomas, T.
1071 Wileman, and M.M. Mogensen. 2017. Ninein is essential for apico-basal microtubule
1072 formation and CLIP-170 facilitates its redeployment to non-centrosomal microtubule
1073 organizing centres. *Open Biol*. 7:160274.

1074 Gomez-Ferreria, M.A., M. Bashkurov, A.O. Helbig, B. Larsen, T. Pawson, A.C. Gingras, and L. Pelletier.
1075 2012. Novel NEDD1 phosphorylation sites regulate gamma-tubulin binding and mitotic
1076 spindle assembly. *J Cell Sci*. 125:3745-3751.
1077 Gomez-Ferreria, M.A., U. Rath, D.W. Buster, S.K. Chanda, J.S. Caldwell, D.R. Rines, and D.J. Sharp.
1078 2007. Human Cep192 is required for mitotic centrosome and spindle assembly. *Curr Biol*.
1079 17:1960-1966.
1080 Grigoriev, I., S.M. Gouveia, B. van der Vaart, J. Demmers, J.T. Smyth, S. Honnappa, D. Splinter, M.O.
1081 Steinmetz, J.W. Putney, Jr., C.C. Hoogenraad, and A. Akhmanova. 2008. STIM1 is a MT-plus-
1082 end-tracking protein involved in remodeling of the ER. *Curr Biol*. 18:177-182.
1083 Gros, O.J., H.G.J. Damstra, L.C. Kapitein, A. Akhmanova, and F. Berger. 2021. Dynein self-organizes
1084 while translocating the centrosome in T-cells. *Mol Biol Cell*. 32:855-868.
1085 Haren, L., M.H. Remy, I. Bazin, I. Callebaut, M. Wright, and A. Merdes. 2006. NEDD1-dependent
1086 recruitment of the gamma-tubulin ring complex to the centrosome is necessary for centriole
1087 duplication and spindle assembly. *J Cell Biol*. 172:505-515.
1088 Haren, L., T. Stearns, and J. Luders. 2009. Plk1-dependent recruitment of gamma-tubulin complexes
1089 to mitotic centrosomes involves multiple PCM components. *PLoS One*. 4:e5976.
1090 Hoogenraad, C.C., P. Wulf, N. Schiefermeier, T. Stepanova, N. Galjart, J.V. Small, F. Grosveld, C.I. de
1091 Zeeuw, and A. Akhmanova. 2003. Bicaudal D induces selective dynein-mediated microtubule
1092 minus end-directed transport. *Embo J*. 22:6004-6015.
1093 Jabermoradi, A., S. Yang, M. Gobes, J.P.M. van Duynhoven, and H. J. 2021. Enabling single-molecule
1094 localization microscopy in turbid food emulsions. *bioRxiv*:2021.2003.2003.433739.
1095 Jia, Y., K.W. Fong, Y.K. Choi, S.S. See, and R.Z. Qi. 2013. Dynamic recruitment of CDK5RAP2 to
1096 centrosomes requires its association with dynein. *PLoS One*. 8:e68523.
1097 Jiang, K., S. Hua, R. Mohan, I. Grigoriev, K.W. Yau, Q. Liu, E.A. Katrukha, A.F. Altelaar, A.J. Heck, C.C.
1098 Hoogenraad, and A. Akhmanova. 2014. Microtubule minus-end stabilization by
1099 polymerization-driven CAMSAP deposition. *Dev Cell*. 28:295-309.
1100 Jiang, X., D.B.T. Ho, K. Mahe, J. Mia, G. Sepulveda, M. Antkowiak, L. Jiang, S. Yamada, and L.E. Jao.
1101 2021. Condensation of pericentrin proteins in human cells illuminates phase separation in
1102 centrosome assembly. *J Cell Sci*. 134.
1103 Jonsson, E., M. Yamada, R.D. Vale, and G. Goshima. 2015. Clustering of a kinesin-14 motor enables
1104 processive retrograde microtubule-based transport in plants. *Nat Plants*. 1:15087.
1105 Joukov, V., J.C. Walter, and A. De Nicolo. 2014. The Cep192-organized aurora A-Plk1 cascade is
1106 essential for centrosome cycle and bipolar spindle assembly. *Mol Cell*. 55:578-591.
1107 Khodjakov, A., R.W. Cole, B.R. Oakley, and C.L. Rieder. 2000. Centrosome-independent mitotic
1108 spindle formation in vertebrates. *Curr Biol*. 10:59-67.
1109 Kim, S., and K. Rhee. 2014. Importance of the CEP215-pericentrin interaction for centrosome
1110 maturation during mitosis. *PLoS One*. 9:e87016.
1111 Kim, T.S., J.E. Park, A. Shukla, S. Choi, R.N. Murugan, J.H. Lee, M. Ahn, K. Rhee, J.K. Bang, B.Y. Kim, J.
1112 Loncarek, R.L. Erikson, and K.S. Lee. 2013. Hierarchical recruitment of Plk4 and regulation of
1113 centriole biogenesis by two centrosomal scaffolds, Cep192 and Cep152. *Proc Natl Acad Sci U*
1114 *S A*. 110:E4849-4857.
1115 Klausner, R.D., J.G. Donaldson, and J. Lippincott-Schwartz. 1992. Brefeldin A: insights into the control
1116 of membrane traffic and organelle structure. *J Cell Biol*. 116:1071-1080.
1117 Klumpp, S., C. Keller, F. Berger, and R. Lipowsky. 2015. Molecular Motors: Cooperative Phenomena
1118 of Multiple Molecular Motors. *In* Multiscale Modeling in Biomechanics and Mechanobiology.
1119 S. De, W. Hwang, and E. Kuhl, editors. Springer London, London. 27-61.
1120 Kohlmaier, G., J. Loncarek, X. Meng, B.F. McEwen, M.M. Mogensen, A. Spektor, B.D. Dynlacht, A.
1121 Khodjakov, and P. Gonczy. 2009. Overly Lona Centrioles and Defective Cell Division upon
1122 Excess of the SAS-4-Related Protein CPAP. *Current Biology*. 19:1012-1018.

1123 Kolano, A., S. Brunet, A.D. Silk, D.W. Cleveland, and M.H. Verlhac. 2012. Error-prone mammalian
1124 female meiosis from silencing the spindle assembly checkpoint without normal
1125 interkinetochore tension. *Proc Natl Acad Sci U S A*. 109:E1858-1867.
1126 Kole, T.P., Y. Tseng, I. Jiang, J.L. Katz, and D. Wirtz. 2005. Intracellular mechanics of migrating
1127 fibroblasts. *Mol Biol Cell*. 16:328-338.
1128 Komarova, Y., G. Lansbergen, N. Galjart, F. Grosveld, G.G. Borisy, and A. Akhmanova. 2005. EB1 and
1129 EB3 control CLIP dissociation from the ends of growing microtubules. *Mol Biol Cell*. 16:5334-
1130 5345.
1131 Lambrus, B.G., V. Daggubati, Y. Uetake, P.M. Scott, K.M. Clutario, G. Sluder, and A.J. Holland. 2016. A
1132 USP28-53BP1-p53-p21 signaling axis arrests growth after centrosome loss or prolonged
1133 mitosis. *J Cell Biol*. 214:143-153.
1134 Lansbergen, G., Y. Komarova, M. Modesti, C. Wyman, C.C. Hoogenraad, H.V. Goodson, R.P. Lemaitre,
1135 D.N. Drechsel, E. van Munster, T.W.J. Gadella Jr., F. Grosveld, N. Galjart, G.G. Borisy, and A.
1136 Akhmanova. 2004. Conformational changes in CLIP-170 regulate its binding to microtubules
1137 and dynactin localisation. *J Cell Biol*. 166:1003-1014.
1138 Lawo, S., M. Bashkurov, M. Mullin, M.G. Ferreria, R. Kittler, B. Habermann, A. Tagliaferro, I. Poser,
1139 J.R. Hutchins, B. Hegemann, D. Pinchev, F. Buchholz, J.M. Peters, A.A. Hyman, A.C. Gingras,
1140 and L. Pelletier. 2009. HAUS, the 8-subunit human Augmin complex, regulates centrosome
1141 and spindle integrity. *Curr Biol*. 19:816-826.
1142 Lawo, S., M. Hasegan, G.D. Gupta, and L. Pelletier. 2012. Subdiffraction imaging of centrosomes
1143 reveals higher-order organizational features of pericentriolar material. *Nat Cell Biol*.
1144 14:1148-1158.
1145 Lechler, T., and E. Fuchs. 2007. Desmoplakin: an unexpected regulator of microtubule organization in
1146 the epidermis. *J Cell Biol*. 176:147-154.
1147 Lee, K., and K. Rhee. 2011. PLK1 phosphorylation of pericentrin initiates centrosome maturation at
1148 the onset of mitosis. *J Cell Biol*. 195:1093-1101.
1149 Lee, S., and K. Rhee. 2010. CEP215 is involved in the dynein-dependent accumulation of
1150 pericentriolar matrix proteins for spindle pole formation. *Cell Cycle*. 9:774-783.
1151 Letort, G., F. Nedelec, L. Blanchoin, and M. Thery. 2016. Centrosome centering and decentering by
1152 microtubule network rearrangement. *Mol Biol Cell*. 27:2833-2843.
1153 Liang, X., M. Kokes, R.D. Fetter, M.D. Sallee, A.W. Moore, J.L. Feldman, and K. Shen. 2020. Growth
1154 cone-localized microtubule organizing center establishes microtubule orientation in
1155 dendrites. *Elife*. 9:e56547.
1156 Lin, Y.N., C.T. Wu, Y.C. Lin, W.B. Hsu, C.J. Tang, C.W. Chang, and T.K. Tang. 2013. CEP120 interacts
1157 with CPAP and positively regulates centriole elongation. *J Cell Biol*. 202:211-219.
1158 Luders, J., U.K. Patel, and T. Stearns. 2006. GCP-WD is a gamma-tubulin targeting factor required for
1159 centrosomal and chromatin-mediated microtubule nucleation. *Nat Cell Biol*. 8:137-147.
1160 Magescas, J., S. Eskinazi, M.V. Tran, and J.L. Feldman. 2021. Centriole-less pericentriolar material
1161 serves as a microtubule organizing center at the base of C. elegans sensory cilia. *Curr Biol*.
1162 31:2410-2417.
1163 Martin, M., A. Veloso, J. Wu, E.A. Katrukha, and A. Akhmanova. 2018. Control of endothelial cell
1164 polarity and sprouting angiogenesis by non-centrosomal microtubules. *Elife*. 7:e33864.
1165 Meitinger, F., J.V. Anzola, M. Kaulich, A. Richardson, J.D. Stender, C. Benner, C.K. Glass, S.F. Dowdy,
1166 A. Desai, A.K. Shiau, and K. Oegema. 2016. 53BP1 and USP28 mediate p53 activation and G1
1167 arrest after centrosome loss or extended mitotic duration. *J Cell Biol*. 214:155-166.
1168 Meitinger, F., M. Ohta, K.Y. Lee, S. Watanabe, R.L. Davis, J.V. Anzola, R. Kabeche, D.A. Jenkins, A.K.
1169 Shiau, A. Desai, and K. Oegema. 2020. TRIM37 controls cancer-specific vulnerability to PLK4
1170 inhibition. *Nature*. 585:440-446.
1171 Meng, W., Y. Mushika, T. Ichii, and M. Takeichi. 2008. Anchorage of microtubule minus ends to
1172 adherens junctions regulates epithelial cell-cell contacts. *Cell*. 135:948-959.

1173 Mennella, V., D.A. Agard, B. Huang, and L. Pelletier. 2014. Amorphous no more: subdiffraction view
1174 of the pericentriolar material architecture. *Trends Cell Biol*. 24:188-197.
1175 Mennella, V., B. Keszthelyi, K.L. McDonald, B. Chhun, F. Kan, G.C. Rogers, B. Huang, and D.A. Agard.
1176 2012. Subdiffraction-resolution fluorescence microscopy reveals a domain of the
1177 centrosome critical for pericentriolar material organization. *Nat Cell Biol*. 14:1159-1168.
1178 Mimori-Kiyosue, Y., I. Grigoriev, G. Lansbergen, H. Sasaki, C. Matsui, F. Severin, N. Galjart, F.
1179 Grosveld, I. Vorobjev, S. Tsukita, and A. Akhmanova. 2005. CLASP1 and CLASP2 bind to EB1
1180 and regulate microtubule plus-end dynamics at the cell cortex. *J Cell Biol*. 168:141-153.
1181 Mogensen, M.M., A. Malik, M. Piel, V. Bouckson-Castaing, and M. Bornens. 2000. Microtubule
1182 minus-end anchorage at centrosomal and non-centrosomal sites: the role of ninein. *J Cell Sci*.
1183 113 (Pt 17):3013-3023.
1184 Muroyama, A., and T. Lechler. 2017. Microtubule organization, dynamics and functions in
1185 differentiated cells. *Development*. 144:3012-3021.
1186 Nashchekin, D., A.R. Fernandes, and D. St Johnston. 2016. Patronin/Shot Cortical Foci Assemble the
1187 Noncentrosomal Microtubule Array that Specifies the Drosophila Anterior-Posterior Axis.
1188 *Dev Cell*. 38:61-72.
1189 Nedelec, F., and D. Foethke. 2007. Collective Langevin dynamics of flexible cytoskeletal fibers. *New*
1190 *Journal of Physics*. 9:427-427.
1191 Nijenhuis, W., M.M.P. van Grinsven, and L.C. Kapitein. 2020. An optimized toolbox for the
1192 optogenetic control of intracellular transport. *J Cell Biol*. 219:e201907149.
1193 Noordstra, I., Q. Liu, W. Nijenhuis, S. Hua, K. Jiang, M. Baars, S. Remmelzwaal, M. Martin, L.C.
1194 Kapitein, and A. Akhmanova. 2016. Control of apico-basal epithelial polarity by the
1195 microtubule minus-end-binding protein CAMSAP3 and spectraplakin ACF7. *J Cell Sci*.
1196 129:4278-4288.
1197 Oddoux, S., K.J. Zaal, V. Tate, A. Kenea, S.A. Nandkeolyar, E. Reid, W. Liu, and E. Ralston. 2013.
1198 Microtubules that form the stationary lattice of muscle fibers are dynamic and nucleated at
1199 Golgi elements. *J Cell Biol*. 203:205-213.
1200 Ohashi, K.G., L. Han, B. Mentley, J. Wang, J. Fricks, and W.O. Hancock. 2019. Load-dependent
1201 detachment kinetics plays a key role in bidirectional cargo transport by kinesin and dynein.
1202 *Traffic*. 20:284-294.
1203 Paz, J., and J. Luders. 2017. Microtubule-Organizing Centers: Towards a Minimal Parts List. *Trends*
1204 *Cell Biol*:S0962-8924(0917)30187-30183.
1205 Pollock, R., R. Issner, K. Zoller, S. Natesan, V.M. Rivera, and T. Clackson. 2000. Delivery of a stringent
1206 dimerizer-regulated gene expression system in a single retroviral vector. *Proc Natl Acad Sci U*
1207 *S A*. 97:13221-13226.
1208 Prosser, S.L., and L. Pelletier. 2020. Centriolar satellite biogenesis and function in vertebrate cells. *J*
1209 *Cell Sci*. 133:jcs239566.
1210 Purohit, A., S.H. Tynan, R. Vallee, and S.J. Doxsey. 1999. Direct interaction of pericentrin with
1211 cytoplasmic dynein light intermediate chain contributes to mitotic spindle organization. *J*
1212 *Cell Biol*. 147:481-492.
1213 Pyrpassopoulos, S., H. Shuman, and E.M. Ostap. 2020. Modulation of Kinesin's Load-Bearing Capacity
1214 by Force Geometry and the Microtubule Track. *Biophys J*. 118:243-253.
1215 Raff, J.W. 2019. Phase Separation and the Centrosome: A Fait Accompli? *Trends Cell Biol*. 29:612-
1216 622.
1217 Ran, F.A., P.D. Hsu, J. Wright, V. Agarwala, D.A. Scott, and F. Zhang. 2013. Genome engineering using
1218 the CRISPR-Cas9 system. *Nat Protoc*. 8:2281-2308.
1219 Redwine, W.B., M.E. DeSantis, I. Hollyer, Z.M. Htet, P.T. Tran, S.K. Swanson, L. Florens, M.P.
1220 Washburn, and S.L. Reck-Peterson. 2017. The human cytoplasmic dynein interactome
1221 reveals novel activators of motility. *Elife*. 6:e28257.
1222 Rios, R.M. 2014. The centrosome-Golgi apparatus nexus. *Philos Trans R Soc Lond B Biol Sci*.
1223 369:20130462.

1224 Rivero, S., J. Cardenas, M. Bornens, and R.M. Rios. 2009. Microtubule nucleation at the cis-side of
1225 the Golgi apparatus requires AKAP450 and GM130. *EMBO J*. 28:1016-1028.
1226 Sallee, M.D., and J.L. Feldman. 2021. Microtubule organization across cell types and states. *Curr Biol*.
1227 31:R506-R511.
1228 Sanchez, A.D., T.C. Branon, L.E. Cote, A. Papagiannakis, X. Liang, M.A. Pickett, K. Shen, C. Jacobs-
1229 Wagner, A.Y. Ting, and J.L. Feldman. 2021. Proximity labeling reveals non-centrosomal
1230 microtubule-organizing center components required for microtubule growth and
1231 localization. *Curr Biol*. 31:3586-3600 e3511.
1232 Schlager, M.A., A. Serra-Marques, I. Grigoriev, L.F. Gumy, M. Esteves da Silva, P.S. Wulf, A.
1233 Akhmanova, and C.C. Hoogenraad. 2014. Bicaudal d family adaptor proteins control the
1234 velocity of Dynein-based movements. *Cell Rep*. 8:1248-1256.
1235 Schmidt, T.I., J. Kleylein-Sohn, J. Westendorf, M. Le Clech, S.B. Lavoie, Y.D. Stierhof, and E.A. Nigg.
1236 2009. Control of centriole length by CPAP and CP110. *Curr Biol*. 19:1005-1011.
1237 Shinohara, H., N. Sakayori, M. Takahashi, and N. Osumi. 2013. Ninein is essential for the
1238 maintenance of the cortical progenitor character by anchoring the centrosome to
1239 microtubules. *Biol Open*. 2:739-749.
1240 Sonnen, K.F., A.M. Gabryjonczyk, E. Anselm, Y.D. Stierhof, and E.A. Nigg. 2013. Human Cep192 and
1241 Cep152 cooperate in Plk4 recruitment and centriole duplication. *J Cell Sci*. 126:3223-3233.
1242 Sonnen, K.F., L. Schermelleh, H. Leonhardt, and E.A. Nigg. 2012. 3D-structured illumination
1243 microscopy provides novel insight into architecture of human centrosomes. *Biology Open*.
1244 1:965-976.
1245 Spektor, A., W.Y. Tsang, D. Khoo, and B.D. Dynlacht. 2007. Cep97 and CP110 suppress a cilia
1246 assembly program. *Cell*. 130:678-690.
1247 Splinter, D., M.E. Tanenbaum, A. Lindqvist, D. Jaarsma, A. Flotho, K.L. Yu, I. Grigoriev, D. Engelsma,
1248 E.D. Haasdijk, N. Keijzer, J. Demmers, M. Fornerod, F. Melchior, C.C. Hoogenraad, R.H.
1249 Medema, and A. Akhmanova. 2010. Bicaudal D2, dynein and kinesin-1 associate with nuclear
1250 pore complexes and regulate centrosome and nuclear positioning during mitotic entry. *PLoS*
1251 *Biol*. 8:e1000350.
1252 Steinman, J.B., C.C. Santarossa, R.M. Miller, L.S. Yu, A.S. Serpinskaya, H. Furukawa, S. Morimoto, Y.
1253 Tanaka, M. Nishitani, M. Asano, R. Zalyte, A.E. Ondrus, A.G. Johnson, F. Ye, M.V. Nachury, Y.
1254 Fukase, K. Aso, M.A. Foley, V.I. Gelfand, J.K. Chen, A.P. Carter, and T.M. Kapoor. 2017.
1255 Chemical structure-guided design of dynapyrazoles, cell-permeable dynein inhibitors with a
1256 unique mode of action. *Elife*. 6:e25174.
1257 Stolz, A., N. Ertych, and H. Bastians. 2015. A phenotypic screen identifies microtubule plus end
1258 assembly regulators that can function in mitotic spindle orientation. *Cell Cycle*. 14:827-837.
1259 Takahashi, M., A. Yamagiwa, T. Nishimura, H. Mukai, and Y. Ono. 2002. Centrosomal proteins CG-
1260 NAP and kendrin provide microtubule nucleation sites by anchoring gamma-tubulin ring
1261 complex. *Mol Biol Cell*. 13:3235-3245.
1262 Tanaka, N., W. Meng, S. Nagae, and M. Takeichi. 2012. Nezha/CAMSAP3 and CAMSAP2 cooperate in
1263 epithelial-specific organization of noncentrosomal microtubules. *Proc Natl Acad Sci U S A*.
1264 109:20029-20034.
1265 Tang, C.J.C., R.H. Fu, K.S. Wu, W.B. Hsu, and T.K. Tang. 2009. CPAP is a cell-cycle regulated protein
1266 that controls centriole length. *Nat Cell Biol*. 11:825-831.
1267 Tas, R.P., A. Chazeau, B.M.C. Cloin, M.L.A. Lambers, C.C. Hoogenraad, and L.C. Kapitein. 2017.
1268 Differentiation between Oppositely Oriented Microtubules Controls Polarized Neuronal
1269 Transport. *Neuron*. 96:1264-1271.
1270 Tibelius, A., J. Marhold, H. Zentgraf, C.E. Heilig, H. Neitzel, B. Ducommun, A. Rauch, A.D. Ho, J.
1271 Bartek, and A. Kramer. 2009. Microcephalin and pericentrin regulate mitotic entry via
1272 centrosome-associated Chk1. *J Cell Biol*. 185:1149-1157.

1273 Toya, M., S. Kobayashi, M. Kawasaki, G. Shioi, M. Kaneko, T. Ishiuchi, K. Misaki, W. Meng, and M.
1274 Takeichi. 2016. CAMSAP3 orients the apical-to-basal polarity of microtubule arrays in
1275 epithelial cells. *Proc Natl Acad Sci U S A*. 113:332-337.
1276 Vergarajauregui, S., R. Becker, U. Steffen, M. Sharkova, T. Esser, J. Petzold, F. Billing, M.S. Kapiloff, G.
1277 Schett, I. Thievessen, and F.B. Engel. 2020. AKAP6 orchestrates the nuclear envelope
1278 microtubule-organizing center by linking golgi and nucleus via AKAP9. *Elife*. 9:e61669.
1279 Vinopal, S., M. Cernohorska, V. Sulimenko, T. Sulimenko, V. Vosecka, M. Flemr, E. Draberova, and P.
1280 Draber. 2012. gamma-Tubulin 2 nucleates microtubules and is downregulated in mouse
1281 early embryogenesis. *PLoS One*. 7:e29919.
1282 Wang, G., Q. Chen, X. Zhang, B. Zhang, X. Zhuo, J. Liu, Q. Jiang, and C. Zhang. 2013. PCM1 recruits
1283 Plk1 to the pericentriolar matrix to promote primary cilia disassembly before mitotic entry. *J*
1284 *Cell Sci*. 126:1355-1365.
1285 Wang, S., D. Wu, S. Quintin, R.A. Green, D.K. Cheerambathur, S.D. Ochoa, A. Desai, and K. Oegema.
1286 2015. NOCA-1 functions with gamma-tubulin and in parallel to Patronin to assemble non-
1287 centrosomal microtubule arrays in C. elegans. *Elife*. 4:e08649.
1288 Watanabe, S., F. Meitinger, A.K. Shiau, K. Oegema, and A. Desai. 2020. Centriole-independent
1289 mitotic spindle assembly relies on the PCNT-CDK5RAP2 pericentriolar matrix. *J Cell Biol*.
1290 219:e202006010.
1291 Wong, Y.L., J.V. Anzola, R.L. Davis, M. Yoon, A. Motamedi, A. Kroll, C.P. Seo, J.E. Hsia, S.K. Kim, J.W.
1292 Mitchell, B.J. Mitchell, A. Desai, T.C. Gahman, A.K. Shiau, and K. Oegema. 2015. Cell biology.
1293 Reversible centriole depletion with an inhibitor of Polo-like kinase 4. *Science*. 348:1155-
1294 1160.
1295 Woodruff, J.B., B. Ferreira Gomes, P.O. Widlund, J. Mahamid, A. Honigmann, and A.A. Hyman. 2017.
1296 The Centrosome Is a Selective Condensate that Nucleates Microtubules by Concentrating
1297 Tubulin. *Cell*. 169:1066-1077.
1298 Wu, J., C. de Heus, Q. Liu, B.P. Bouchet, I. Noordstra, K. Jiang, S. Hua, M. Martin, C. Yang, I. Grigoriev,
1299 E.A. Katrukha, A.F. Altelaar, C.C. Hoogenraad, R.Z. Qi, J. Klumperman, and A. Akhmanova.
1300 2016. Molecular Pathway of Microtubule Organization at the Golgi Apparatus. *Dev Cell*.
1301 39:44-60.
1302 Yang, C., J. Wu, C. de Heus, I. Grigoriev, N. Liv, Y. Yao, I. Smal, E. Meijering, J. Klumperman, R.Z. Qi,
1303 and A. Akhmanova. 2017. EB1 and EB3 regulate microtubule minus end organization and
1304 Golgi morphology. *J Cell Biol*. 216:3179-3198.
1305 Yang, R., and J.L. Feldman. 2015. SPD-2/CEP192 and CDK Are Limiting for Microtubule-Organizing
1306 Center Function at the Centrosome. *Curr Biol*. 25:1924-1931.
1307 Yeow, Z.Y., B.G. Lambrus, R. Marlow, K.H. Zhan, M.A. Durin, L.T. Evans, P.M. Scott, T. Phan, E. Park,
1308 L.A. Ruiz, D. Moralli, E.G. Knight, L.M. Badder, D. Novo, S. Haider, C.M. Green, A.N.J. Tutt, C.J.
1309 Lord, J.R. Chapman, and A.J. Holland. 2020. Targeting TRIM37-driven centrosome
1310 dysfunction in 17q23-amplified breast cancer. *Nature*. 585:447-452.
1311 Zheng, Y., R.A. Buchwalter, C. Zheng, E.M. Wight, J.V. Chen, and T.L. Megraw. 2020. A perinuclear
1312 microtubule-organizing centre controls nuclear positioning and basement membrane
1313 secretion. *Nat Cell Biol*. 22:297-309.
1314 Zhu, F., S. Lawo, A. Bird, D. Pinchev, A. Ralph, C. Richter, T. Muller-Reichert, R. Kittler, A.A. Hyman,
1315 and L. Pelletier. 2008. The mammalian SPD-2 ortholog Cep192 regulates centrosome
1316 biogenesis. *Curr Biol*. 18:136-141.
1317 Zhu, X.D., and I. Kaverina. 2013. Golgi as an MTOC: making microtubules for its own good.
1318 *Histochemistry and Cell Biology*. 140:361-367.

1319

1320 **Figure legends.**

1321 **Figure 1. Formation and characterization of caMTOCs in AKAP450/CAMSAP2 knockout cells**

1322 (A) Immunofluorescence images of control or centrinone-treated wild type (WT) RPE1 cells stained for
1323 centrioles (CEP135, red; centrin, green). The zooms of the boxed area show the centrioles stained with
1324 the indicated markers.

1325 (B) Quantification shows the percentage of cells with centrioles before and after the centrinone
1326 treatment. 350 cells (n=7 fields of view) analyzed for each measurement in three independent
1327 experiments. The statistical significance was determined by unpaired two-tailed Mann-Whitney test
1328 in Prism 9.1 (***p<0.001). Values represent mean±SD.

1329 (C) Immunofluorescence images of centrinone-treated WT RPE1 cells stained for pericentrin (PCNT,
1330 green) and the Golgi marker GM130 (red). Inset shows the merged image of the boxed area.

1331 (D) Diagrams of the microtubule organization in WT and knockout (KO) cells used.

1332 (E) Immunofluorescence images of control and centrinone-treated WT and knockout RPE1 cell lines
1333 stained for pericentrin (green) and microtubules (α-tubulin, red). Enlargements on the right show the
1334 boxed areas.

1335 (F) Immunofluorescence images of centrinone-treated AKAP450/CAMSAP2 knockout RPE1 cells
1336 stained for different PCM components as indicated and imaged by STED microscopy.

1337 (G) Quantification of the length and width of cylindrical PCM clusters. n=65 cells analyzed in three
1338 independent experiments. Values represent mean±SD.

1339 (H) (Top left) Two frames of time-lapse images of centrinone-treated AKAP450/CAMSAP2 knockout
1340 RPE1 cells stably expressing GFP-CDK5RAP2 prior to FRAP experiments. (Top right) Schemes show
1341 regions of caMTOC where photobleaching was performed. (Middle) Kymographs illustrating
1342 fluorescence of unbleached caMTOC (No FRAP), fully photobleached caMTOC (Whole FRAP) and
1343 partially photobleached caMTOC (Partial FRAP). (Bottom) Time-lapse images illustrating partial FRAP
1344 of a caMTOC. Time is min:sec.

1345 (I) Normalized fluorescence intensity as a function of time. The blue line shows averaged intensity
1346 traces of unbleached caMTOCs (No FRAP), the black line shows averaged intensity traces of fully
1347 photobleached caMTOCs (Whole FRAP), the red line shows averaged intensity traces of whole
1348 caMTOC that were partially photobleached (whole caMTOC intensity, Partial FRAP) and the green line
1349 shows averaged intensity traces of the photobleached region of the partially photobleached caMTOC
1350 (FRAP region intensity, Partial FRAP). n=3 for No FRAP, 3 for Whole FRAP, 5 for Partial FRAP (whole

1351 caMTOC intensity) and 5 for Partial FRAP (FRAP region intensity); time-lapse images of ~1600
1352 timepoints with 2 s interval were analyzed for each measurement. Values are mean±SD.

1353

1354 **Figure 2. Molecular composition of caMTOCs in AKAP450/CAMSAP2 knockout cells**

1355 All the cells used in this figure are AKAP450/CAMSAP2 knockout cells, except for panel E as indicated.

1356 (A-C) Immunofluorescence images of control or centrinone-treated AKAP450/CAMSAP2 knockout
1357 RPE1 cells stained for and depleted of the indicated proteins.

1358 (D, F-I) Immunofluorescence images of centrinone-treated AKAP450/CAMSAP2 knockout RPE1 cells
1359 stained for and depleted of the indicated proteins.

1360 (E) Immunofluorescence images of centrinone-treated AKAP450/CAMSAP2/p53 knockout and
1361 AKAP450/CAMSAP2/p53/pericentrin knockout RPE1 cells stained as indicated.

1362 In panels A-I, insets show enlargements of the merged channels of the boxed areas, and dashed lines
1363 indicate cell edges.

1364 (J) Quantification of the main PCM organization types, as described in Figure 1- figure supplement 2A,
1365 for cells prepared as described in panel A-C, E-I. Numbers on the histogram show the percentages.
1366 1293 (-CentB), 1547(+CentB), 2021(siLuci), 1822(siCEP152), 1345(siCEP192), 1161(siNEDD1), 2302
1367 (AKAP450/CAMSAP2/p53/PCNT knockout (PCNT KO)), 2264(siCDK5RAP2), 2510(siγ-tubulin),
1368 2408(siNIN) and 2526(siDHC) cells were analyzed for each measurement in three independent
1369 experiments (n=3). Values represent mean±SD.

1370 (K) Summarizing table of PCM localization and the depletion effects on caMTOC formation in
1371 AKAP450/CAMSAP2 knockout RPE1 cells. NT, not tested.

1372

1373 **Figure 3. Microtubule organization in acentriolar cells missing different caMTOC components**

1374 (A) Immunofluorescence images of centrinone-treated AKAP450/CAMSAP2 knockout RPE1 cells
1375 depleted of the indicated proteins and stained for microtubules (α-tubulin, red) and different PCM
1376 proteins (green). Insets show enlargements of the merged channels of the boxed areas and dashed
1377 lines show cell boundaries.

1378 (B) Quantification of the normalized overall microtubule intensity for the indicated conditions. The
1379 number of cells analyzed in three independent experiments: n=56 (siLuci), 45 (siPCNT), 33

1380 (siCDK5RAP2), 36 (siNinein), 43 (siγ-tubulin) and 28 (siDHC). The statistical significance was
1381 determined by unpaired two-tailed Mann-Whitney test in Prism 9.1 (***p<0.001). Values represent
1382 mean±SD.

1383 (C) Microtubule images were split into a radial and non-radial components (heat maps) based on
1384 microtubule orientation in relation to the PCM clusters or the brightest point, as described in
1385 Methods.

1386 (D) Quantification of the proportion of the non-radial microtubules shown in panel C (see Methods
1387 for details). The number of cells analyzed for each measurement in three independent experiments:
1388 n=25 (siLuci), 43 (siPCNT), 32 (siCDK5RAP2), 34 (siNinein), 37 (siγ-tubulin) and 25 (siDHC). The
1389 statistical significance was determined by unpaired two-tailed Mann-Whitney test in Prism 9.1
1390 (***p<0.001). Values represent mean±SD.

1391 (E) Diagram illustrating the distribution of PCM clusters and microtubule organization upon the
1392 depletion of the indicated proteins in centrinone-treated AKAP450/CAMSAP2 knockout cells.

1393

1394 **Figure 4. Microtubule- and dynein-dependent disassembly of caMTOCs**

1395 (A) Diagram illustrating different order of cell treatments with nocodazole (Noco) and/or dynapyrazole
1396 A (Dyna, 5 µM) and the time points when the cells were fixed.

1397 (B) Immunofluorescence staining of centrinone-treated AKAP450/CAMSAP2 knockout cells treated as
1398 shown in panel A. Dashed red circles represent the areas occupied by PCM clusters in each condition.

1399 (C) Quantification of the area occupied by PCM clusters in each condition, as shown in panels A and B.
1400 n=35-53 cells analyzed for each measurement in three independent experiments. The statistical
1401 significance was determined by unpaired two-tailed Mann-Whitney test in Prism 9.1 (not significant
1402 (NS), *P*<0.12; **P*<0.033; ****P*<0.001). Values are represented as mean±SD.

1403 (D) Western blot showing that 3 hrs treatment with dynaprazole A does not affect the expression of
1404 the endogenous dynein heavy chain and the dynactin large subunit p150Glued.

1405 (E) Time-lapse images of centrinone-treated AKAP450/CAMSAP2 knockout RPE1 cells stably
1406 expressing GFP-CDK5RAP2. Microtubules were visualized by treating cells with 100 nM SiR-tubulin
1407 overnight. Red arrows show the immobilized PCM clusters at indicated timepoints. Time is min:sec.
1408 Time-lapse images of the same cell prior to the nocodazole treatment were shown in Figure 1 - figure
1409 supplement 3B.

1410 (F) (Top) Kymograph illustrating the motility of PCM clusters during microtubule disassembly with
1411 nocodazole. (Bottom) Measurements of the normalized microtubule (SiR-tubulin) fluorescence
1412 intensity (red plot, left Y-axis) and the instantaneous velocity of GFP-CDK5RAP2 clusters (green plot,
1413 right Y-axis) during the movement of GFP-CDK5RAP2 clusters away from caMTOC. Microtubule density
1414 around each PCM cluster was determined by measuring mean fluorescence intensity of SiR-tubulin in
1415 a circular area with a 2 µm radius centered on the PCM cluster and normalizing it to the mean
1416 fluorescence intensity of 20 images prior to nocodazole addition (set as 100%). The moment when a
1417 PCM cluster started to move out of the caMTOC was set as the initial time point (0 min) for this cluster,
1418 and the subsequent PCM cluster motion velocity and the relative local microtubule density of 43 time
1419 points were calculated and averaged. n=12 clusters were analyzed in each condition. Values are
1420 represented as mean±SD.

1421 (G) Motor-PAINT images of centrinone-treated AKAP450/CAMSAP2 knockout RPE1 cells before and
1422 after nocodazole treatment. Plus-end-out microtubules are shown in white whereas minus-end-out
1423 microtubules are shown in magenta. Asterisks represent the putative position of caMTOC.

1424 (H) Summarizing diagram illustrating microtubule organization and the motility of GFP-CDK5RAP2-
1425 positive PCM clusters during nocodazole treatment and dynapyrazole A (treat first) and nocodazole
1426 co-treatment.

1427 (I) Immunofluorescence images of centrinone-treated AKAP450/CAMSAP2 knockout RPE1 cells
1428 stained for microtubules (α-tubulin, red) and PCM (PCNT, green). Enlargements show the merged and
1429 single channels of the boxed areas.

1430

1431 **Figure 5. Dynamics of microtubule nucleation and caMTOC re-assembly in acentriolar cells**

1432 (A) Immunofluorescence images of microtubule regrowth after nocodazole washout at the indicated
1433 timepoints in centrinone-treated AKAP450/CAMSAP2 knockout RPE1 cells stained for PCM
1434 components (green) and newly nucleated microtubules (EB1, red). A Golgi marker, GM130 (blue), is
1435 included in the left row, and zooms of the boxed regions (numbered 1 and 2) show that microtubules
1436 nucleate from PCM clusters but not from the Golgi membranes. Dashed lines show cell boundaries.

1437 (B) (Top) Timeline shows the time course of protein depletion (siRNA transfection), nocodazole
1438 treatment, nocodazole washout and microtubule regrowth. (Bottom) Immunofluorescence images of
1439 microtubule regrowth experiments after depletion of the indicated proteins in centrinone-treated
1440 AKAP450/CAMSAP2 knockout RPE1 cells stained for the indicated PCM markers (green) and EB1 as a

1441 marker of nascent microtubules (red). Cell outlines are indicated with dashed lines and enlargements
1442 of the merged channels of the boxed areas are shown on the right.

1443 (C) Quantification of normalized microtubule intensity at 30 s after nocodazole washout in control
1444 cells and cells depleted of the indicated PCM proteins. n=40 (siLuci, siPCNT), 57 (siCDK5RAP2), 48
1445 (siNIN), 45 (siγ-tubulin) and 50 (siDHC) cells analyzed for each measurement in three independent
1446 experiments. The statistical significance was determined by unpaired two-tailed Mann-Whitney test
1447 in Prism 9.1 (**P<0.002; ***P<0.001). Values are represented as mean±SD.

1448 (D) Time-lapse images of centrinone-treated AKAP450/CAMSAP2 knockout RPE1 cells stably
1449 expressing GFP-CDK5RAP2 before and after nocodazole washout. Dispersed GFP-CDK5RAP2-positive
1450 PCM clusters (GFP, green) serve as microtubule nucleation sites (SiR-tubulin, red) and coalesce into a
1451 big cluster after nocodazole washout. Time is min:sec.

1452 (E) Immunofluorescence images of centrinone-treated AKAP450/CAMSAP2 knockout RPE1 cells
1453 stained for pericentrin (green) and microtubules (α-tubulin, red) at the indicated timepoints after
1454 nocodazole washout.

1455 (F) Measurements of normalized fluorescence intensity of PCM clusters at the indicated distances in
1456 relation to the brightest point, as described in Methods. The biggest PCM cluster (which normally also
1457 had the highest fluorescence intensity) was selected as the center, around which 10 concentric circles
1458 with 2 µm width were drawn. Fluorescence intensity of PCM clusters in these concentric circles was
1459 measured automatically and normalized by the sum of the total PCM intensity in each cell per
1460 condition. n=12 cells per plot per timepoint. Values represent mean±SD.

1461 (G) Summarizing diagram illustrating microtubule organization and motility of GFP-CDK5RAP2-positive
1462 PCM clusters during nocodazole washout.

1463

1464 **Figure 6. caMTOC formation in the presence of CAMSAP2 using inducible motor recruitment**

1465 (A) Immunofluorescence images of control or centrinone treated AKAP450 knockout RPE1 cells
1466 stained for CAMSAP2 (green), PCM protein (γ-tubulin, cyan) and microtubules (α-tubulin, red).
1467 Enlargements show the boxed regions of the merged images.

1468 (B) Time lapse images of centrinone treated AKAP450 knockout RPE1 cells stably expressing GFP-
1469 CDK5RAP2 (green). Microtubules were labeled with 100 nM SiR-tubulin overnight (red, top row). The
1470 maximum intensity projection includes 200 frames, 200 ms/frame. Red arrows show the motion
1471 directions of GFP-CDK5RAP2-positive PCM clusters. Time is min:sec.

1472 (C) A diagram of microtubule organization and PCM motility in AKAP450 knockout cells.

1473 (D, E) Diagram of the inducible heterodimerization assay with ppKin14 and CAMSAP2. (D) CAMSAP2
1474 was tagged with mCherry and fused to a tandemly repeated FKBP domain; tetramerized ppKin14 was
1475 tagged with TagBFP and fused to FRB. Rapalog induces the binding of CAMSAP2 and ppKin14 by linking
1476 FKBP to FRB. (E) Rapalog treatment induces the binding of CAMSAP2 (red) and ppKin14 (blue) and the
1477 formation of radial microtubule network. In this scheme, PCM-anchored microtubules are not shown.

1478 (F) Immunofluorescence images of centrinone-treated AKAP450/CAMSAP2 knockout RPE1 cells co-
1479 transfected with 2FKBP-mCherry-CAMSAP2 and FRB-TagBFP-GCN4-ppKin14 and stained for the
1480 indicated proteins in cells treated with DMSO or rapalog. Zooms show the magnifications of boxed
1481 areas.

1482 (G) Quantification of the proportion of cells with a radial, whirlpool-like or non-radial microtubule
1483 organization with and without rapalog treatment. Numbers on the histogram show the percentages.
1484 414 cells treated with DMSO (-Rapa) and 385 cells treated with rapalog (+Rapa) analyzed for each
1485 measurement in three independent experiments (n=3). Values represent mean±SD.

1486

1487 **Figure 7. The role of the PCM in CAMSAP2-driven formation of caMTOCs**

1488 (A,B) Immunofluorescence images of centrinone-treated AKAP450/CAMSAP2/p53/pericentrin
1489 knockout RPE1 cells transfected with 2FKBP-mCherry-CAMSAP2 and FRB-TagBFP-GCN4-ppKi14 and
1490 stained for the indicated components before (top) or after an overnight rapalog treatment. Zooms
1491 show magnifications of boxed areas. Black dashed lines show the position of the nucleus.

1492 (C) Cells treated as described for panel A were co-transfected with GFP-pericentrin and stained for
1493 mitochondria (cytochrome C, red) and CAMSAP2 (red) in same channel overnight after rapalog
1494 addition. Zooms show magnifications of boxed areas.

1495 (D) Quantification of the proportion of cells with different types of microtubule minus end
1496 organization before and after overnight rapalog treatment. Numbers on the histogram show the
1497 percentages. 334 (-Rapa), 424(+Rapa) cells of AKAP450/CAMSAP2/p53/pericentrin knockout RPE1
1498 cells, 206(-Rapa) and 239(+Rapa) of AKAP450/CAMSAP2/CDK5RAP2/MMG/p53/pericentrin knockout
1499 RPE1 cells analyzed for each measurement in three independent experiments (n=3). Values represent
1500 mean±SD.

1501 (E) Immunofluorescence images of centrinone-treated
1502 AKAP450/CAMSAP2/CDK5RAP2/MMG/p53/pericentrin knockout RPE1 cells transfected with 2FKBP-

1503 mCherry-CAMSAP2 and FRB-TagBFP-GCN4-ppKi14 and stained for microtubules (α-tubulin, green)
1504 after an overnight rapalog treatment. Zooms show magnifications of boxed areas.

1505

1506 **Figure 8. Cytosim simulations of PCM and microtubule self-organization.**

1507 In all simulations, we considered a circular cell with a radius of 10 µm (gray line), containing
1508 microtubules (red), PCM complexes (green), and CAMSAP-kin14 complexes (blue).

1509 (A) Simulation of 300 PCM complexes; each PCM complex is attached to a dynein motor, and from
1510 each complex, a MT can grow. A weak adhesive interaction is introduced between the PCM complexes.
1511 A compact PCM cluster is observed.

1512 (B) The same simulation as in (A), but with the adhesive interaction disabled; PCM is organized in a
1513 ring-like structure.

1514 (C) The simulation in (A) modified in two ways: a randomly organized, dynamic microtubule network
1515 with 300 filaments is added, and only 50 of the 300 PCM complexes can nucleate microtubules. PCM
1516 cluster formation is disrupted.

1517 (D) The same simulation as in (C), but the strength of the adhesive interaction is increased. The
1518 formation of a compact cluster is recovered.

1519 (E) Cumulative distributions of distances of the PCM complexes to the average position (the center of
1520 mass), determined from the last frame of the simulations.

1521 (F) The mean and standard deviation (SD) of the distances of the PCM complexes to the center of mass
1522 from different repetitions of the simulations. Each system was simulated 10 times. Small values for
1523 the mean and for the standard deviation indicate a compact cluster. For a ring-like structure, the mean
1524 values are is larger and describe the radius of the ring. A dispersed localization of PCM complexes is
1525 characterized by large values for the mean and the standard deviation.

1526 (G) Simulation of 300 CAMSAP-kin14 complexes, which consist of a microtubule nucleation site and
1527 five kinesin-14 motors, but do not adhere to each other. The complexes form a ring-like structure.

1528 (H) The same simulation as in (G), but with complexes that have the same weak adhesive interaction
1529 as for the PCM complexes in (A). The complexes form a central compact cluster.

1530 (I) Simulation of a mixed system with 150 CAMSAP-kin14 complexes that do not adhere to each other
1531 and 150 weakly adhesive PCM complexes. All complexes associate in a central compact cluster.

(J) The same simulation as in (I), but with non-adhesive PCM complexes. A ring-like structure is formed.

(K) Cumulative distributions of the distances from all complexes to the center of mass of the last frame of the simulation.

(L) The mean and standard deviation of the distances from all complexes to the center of mass from different repetitions of the simulations. Each system was simulated 10 times. A compact cluster is characterized by a small value for the mean and for the standard deviation. A ring-like structure has a larger mean value.

1539 **Legends to Supplemental Figures**

1540 **Figure 1 – figure supplement 1. Characterization of caMTOCs in wild type, AKAP450 knockout and**
1541 **CAMSAP2 knockout cells**

1542 (A) Immunofluorescence images of centrinone B treated AKAP450 knockout RPE1 cells stained for
1543 CAMSAP2 (green) and γ-tubulin (red), transfected either with control (Luciferase) or CAMSAP2 siRNAs.
1544 Insets show enlargements of the merged images of the boxed areas.

1545 (B) Quantification of CAMSAP2 depletion and caMTOC formation related to panel A. For normalized
1546 CAMSAP2 intensity, n=76 (siLuciferase) and 62 (siCAMSAP2) cells from three independent experiment
1547 were analyzed; to calculate the percentage of cells showing dispersed or clustered PCM, n=300
1548 (siLuciferase) and 299 (siCAMSAP2) cells analyzed for each measurement in three independent
1549 experiments. The statistical significance was determined by unpaired two-tailed Mann-Whitney test
1550 in Prism 9.1 (***$p<0.001$). Values represent mean±SD.

1551 (C-E) Immunofluorescence images of wild type and CAMSAP2 knockout cells treated with DMSO,
1552 CentB, Brefeldin A (BFA) (5 µg/ml (17.8 µM) for 2 hrs), and stained for centrioles (Centrin, red), PCM
1553 (PCNT, green), microtubules (α-tubulin, red) and Golgi apparatus (GM130, blue). Insets show
1554 enlargements of the merged channels of the boxed areas.

1555 (F) Quantification of the proportion of cells with different types of microtubule minus end organization
1556 in wild type (WT) and CAMSAP2 knockout RPE1 cell lines with indicated treatment. 319 (+DMSO),
1557 413(+CentB), 412(+BFA), 353(+CentB+BFA) WT cells and 340(+DMSO), 445(+CentB), 384(+BFA),
1558 553(+CentB+BFA) CAMSAP2 knockout RPE1 cells analyzed for each measurement in three
1559 independent experiments (n=3). Values represent mean±SD.

1560

1561 **Figure 1 – figure supplement 2. Characterization of caMTOCs in AKAP450/CAMSAP2 knockout cells**

1562 (A) Immunofluorescence images of control (-CentB) and centrinone-treated AKAP450/CAMSAP2
1563 knockout RPE1 cells stained for pericentrin and centrin to show the main PCM organization types
1564 (centrin-negative cells with cylindrical or round PCM cluster, dispersed PCM or no cluster, and centrin-
1565 positive centrosomes) in each condition. Enlargements of the merged channels of the boxed areas are
1566 shown on the right.

1567 (B) Quantification of the main PCM organization types in centrinone-treated AKAP450 knockout and
1568 AKAP450/CAMSAP2 knockout RPE1 cells. Numbers on the histogram show the percentages. 465

1569 (AKAP450 KO) and 495 (AKAP450/CAMSAP2 KO) cells analyzed for each measurement in three
1570 independent experiments (n=3). Values represent mean±SD.

1571 (C) Diagram showing the generation of CPAP or PLK4 depleted AKAP450/CAMSAP2 knockout RPE1
1572 cells with different drug treatments. Cells were transfected with siRNAs to depleted CPAP and PLK4
1573 respectively. After 2 days, the transfection was performed again to increase the depletion efficiency.
1574 After 2 more days, cells were treated with thymidine to block cell proliferation or with a combination
1575 of thymidine and centrinone B, or thymidine, centrinone B and the PLK1 inhibitor BI 2536 for one or
1576 three days. Cells were fixed for the first time (Fix1) after a 24 hr drug treatment, and for the second
1577 time (Fix2) after a 72 hr drug treatment.

1578 (D) Quantification of the main PCM organization types, as described in panel A, for cells prepared as
1579 described in panel E-G. Numbers on the histogram show the percentages and numbers in brackets
1580 show cells analyzed for each measurement in three independent experiments (n=3; 247-612 cells
1581 analyzed per condition). Values represent mean±SD.

1582 (E-G) Immunofluorescence images of Fix2 (as described in panel C) showing control (transfected with
1583 siRNA against Luciferase), or depleted of PLK4 or CPAP and treated as indicated. Cells were stained for
1584 centrioles (CEP135, centrin), PCM proteins (PCNT) and microtubules (α-tubulin). Images illustrate the
1585 PCM organization types in each condition. Insets show the merged channels of the boxed areas.

1586

1587 **Figure 1 – figure supplement 3. PCM dynamics visualized with GFP-CDK5RAP2**

1588 (A) Immunofluorescence images of control (-CentB) and centrinone B treated WT RPE1 cell stably
1589 expressing GFP-CDK5RAP2 (green) stained for α-tubulin (red) and pericentrin (PCNT, blue). Zooms
1590 show enlargements of the boxed regions.

1591 (B) Time-lapse images of centrinone-treated AKAP450/CAMSAP2 knockout RPE1 cells stably
1592 expressing GFP-CDK5RAP2. Microtubules are visualized by treating the cells with 100 nM SiR-tubulin
1593 overnight. PCM labeled with GFP-CDK5RAP2 (green) forms a stable cluster that functions as the MTOC.
1594 Zooms show the enlarged GFP channel of the boxed regions. Time is min:sec.

1595

1596 **Figure 2 – figure supplement 1. Characterization of PCM components localizing to caMTOCs in**
1597 **AKAP450/CAMSAP2 knockout cells**

1598 (A) Western blot showing that endogenous NEDD1 and CEP192 are present in centrinone-treated
1599 AKAP450/CAMSAP2 knockout cells.

1600 (B) Western blot results showing the depletion of the indicated PCM proteins.

1601 (C) Immunofluorescence images of centrinone-treated AKAP450/CAMSAP2 knockout RPE1 cells
1602 showing the localization and the effects of depletion of the indicated proteins on the caMTOCs. siRNA
1603 against luciferase was used as a control. Zooms show enlargements of the merged channels of the
1604 boxed areas.

1605

1606 **Figure 2 – figure supplement 2. Generation of the AKAP450/CAMSAP2/p53/pericentrin knockout**
1607 **RPE1 cell line**

1608 (A) Diagram illustrating two sgRNA sites targeting p53 exon 2 and exon 4. The green and red boxes
1609 indicate the position of the PAM sites, and the predicted Cas9 cut sites are indicated by scissors.

1610 (B,C) Genotyping results of the genomic mutation using gel-purified PCR product which covers exon 2
1611 and exon 4 of the p53-encoding gene in AKAP450/CAMSAP2/p53 knockout cell line and a diagram
1612 illustrating the induced inversion.

1613 (D) Diagram illustrating the binding sites of p53 antibodies and the position of the mutation induced
1614 in p53-encoding gene.

1615 (E,F) Immunofluorescence and Western blot images showing p53 expression in control and
1616 AKAP450/CAMSAP2/p53 knockout cells.

1617 (G-H) Genotyping results of the genomic mutation using gel-purified PCR product which covers the
1618 two sgRNAs targeting sites within pericentrin-encoding gene in AKAP450/CAMSAP2/p53/pericentrin
1619 knockout cell line and a diagram illustrating the induced genomic mutations within exon 5 of the
1620 pericentrin-encoding gene. The green and red boxes indicate the position of the PAM sites, and the
1621 predicted Cas9 cut sites are indicated by scissors.

1622 (I) Diagram illustrating the binding domain of the pericentrin antibody and the positions of the
1623 mutations induced downstream of the Cas9 cutting sites.

1624 (J) Immunofluorescence images confirming the loss of pericentrin in
1625 AKAP450/CAMSAP2/p53/pericentrin knockout cells.

1626 (K) Western blot confirming the loss of p53 and pericentrin in AKAP450/CAMSAP2/p53/pericentrin
1627 knockout cells.

1628

1629 **Figure 2 – figure supplement 3. Characterization of cell division in centrinone-treated**
1630 **AKAP450/CAMSAP2/p53 knockout cells**

1631 (A) Immunofluorescence images of metaphase AKAP450/CAMSAP2/p53 knockout cells treated with
1632 DMSO and centrinone (CentB) and stained for h microtubules (α-tubulin, magenta), PCM (PCNT, red),
1633 centrioles (Centrin, green) and DNA (DAPI, blue).

1634 (B-C) Phase-contrast time-lapse images of centrinone-treated AKAP450/CAMSAP2/p53 knockout
1635 RPE1 cells. Time is hh:mm. (B) The red and blue arrows show two cells with different mitosis duration.
1636 (C) Mitotic phases in a representative cell.

1637 (D) Quantification of the mitosis duration of centrinone-treated AKAP450/CAMSAP2/p53 knockout
1638 RPE1 cells. 36 cells from 14 videos were analyzed. Values represent mean±SD.

1639

1640 **Figure 2 – figure supplement 4. Characterization of PCM organization in AKAP450/CAMSAP2/p53/**
1641 **pericentrin knockout cells**

1642 (A) Immunofluorescence images of centrinone-treated AKAP450/CAMSAP2/p53 knockout (Control)
1643 and AKAP450/CAMSAP2/p53/pericentrin knockout (PCNT KO) RPE1 cells showing staining for the
1644 indicated proteins. Zooms of the boxed areas show merged channels.

1645 (B) Western blots showing the expression levels of CDK5RAP2, γ-tub, and ninein in control (+DMSO)
1646 and centrinone-treated (+CentB) AKAP450/CAMSAP2/p53 knockout and
1647 AKAP450/CAMSAP2/p53/PCNT knockout RPE1 cells.

1648

1649 **Figure 2 – figure supplement 5. Effects of the depletion or knockout of EB1 and EB3 on caMTOC**
1650 **formation in AKAP450/CAMSAP2 knockout cells**

1651 (A) Immunofluorescence images of centrinone-treated AKAP450/CAMSAP2 knockout cells stained for
1652 EB1 or EB3 and pericentrin showing effects of EB1 or EB3 depletion on caMTOCs.

1653 (B) Western blot confirming the loss of AKAP450 and CAMSAP2 in AKAP450/CAMSAP2/EB1/EB3
1654 mutant cells.

1655 (C) Immunofluorescence images of control or centrinone-treated AKAP450/CASMSAP2/EB1/EB3
1656 mutant RPE1 cells stained for the indicated proteins. Zooms of the boxed areas show merged
1657 channels.

1658

1659 **Figure 4 – Figure supplement 1. PCM dynamics during nocodazole treatment in centrinone-treated**
1660 **AKAP450/CAMSAP2 knockout cells**

1661 (A) Time-lapse images illustrating the dynamics of GFP-CDK5RAP2 clusters (green, white arrows) and
1662 microtubules (visualized with an overnight treatment with 100 nM SiR-tubulin, red) during nocodazole
1663 treatment. A single frame of the whole cell is on the bottom left, with the boxed area indicating the
1664 location of the enlarged images. Time is min:sec.

1665 (B) (Top) Motor-PAINT images of centrinone-treated AKAP450/CAMSAP2 knockout RPE1 cells before
1666 and after treatment with 10 µM nocodazole for 15 min (the same cells, colorized differently, are
1667 displayed in Figure 4G). Microtubule segments were assigned a color based on their absolute
1668 orientation, with their plus-ends pointing in the directions indicated with the compass. Asterisks
1669 indicate approximate assumed positions of caMTOCs. (Bottom) Directionality-filtered reconstruction
1670 of motor tracks used for generating the Motor-PAINT images.

1671 (C) Immunofluorescence images of centrinone-treated AKAP450/CAMSAP2 knockout RPE1 cells
1672 stained for microtubules (α-tubulin, red) and PCM (PCNT, green) after cold treatment for 30 min at
1673 4°C. Enlargements show the merged and single channels of the boxed areas.

1674

1675 **Figure 5 – figure supplement 1. PCM dynamics and microtubule regrowth during nocodazole**
1676 **washout in AKAP450/CAMSAP2 knockout cells**

1677 (A) Immunofluorescence images of control (+DMSO) and centrinone-treated AKAP450/CAMSAP2
1678 knockout cells treated with cold alone or cold and nocodazole, and stained for nascent microtubules
1679 (EB1, red), PCM (PCNT, green) and the Golgi apparatus (GM130, blue) 30 s after nocodazole washout.

1680 (B) Immunofluorescence images of acentriolar AKAP450/CAMSAP2 knockout RPE1 cells fixed at 30 s
1681 and 10 min after nocodazole washout and stained for the indicated markers. Zooms show the
1682 enlargements of boxed areas. Dashed lines show the cell boundaries.

1683 (C) Summarizing table showing the presence of PCM components in clusters (including centrosome
1684 and caMTOC) before and after nocodazole washout in indicated conditions.

1685 (D) Immunofluorescence images of control acentriolar AKAP450/CAMSAP2 knockout RPE1 cells and
1686 cells lacking the indicated PCM proteins fixed 2 min after nocodazole washout and stained for EB1 (a
1687 marker of growing microtubules, red) and different PCM proteins (γ-tubulin, ninein (NIN) and dynein
1688 heavy chain (DHC), green; CDK5RAP2 and PCNT, blue). Insets show the enlargements of the boxed

areas and the heat maps on the right show the radial and non-radial part of growing microtubules. Dashed lines show the cell boundaries.

(E) Quantification of the proportion of non-radial microtubules 2 min after nocodazole washout. The radial and the non-radial microtubule intensities were measured and the non-radial microtubule intensity was normalized by dividing it by the sum of the radial and the non-radial microtubule intensities for each group. n=20-25 cells analyzed for each measurement in three independent experiments. The statistical significance was determined by unpaired two-tailed Mann-Whitney test in Prism 9.1 (***$p<0.001$). Values represent mean±SD.

(F) Diagram showing microtubule regrowth and PCM assembly in control acentriolar AKAP450/CAMSAP2 knockout RPE1 cells and cells depleted of the indicated PCM proteins at 30 s and 2 min after nocodazole washout.

Figure 5 – figure supplement 2. Pericentrin is required for PCM clustering in acentriolar AKAP450/CAMSAP2 knockout RPE1 cells

Time-lapse images of centrinone-treated AKAP450/CAMSAP2 knockout RPE1 cells stably expressing GFP-CDK5RAP2 (green), which is diffusely distributed and does not form any clear clusters. Microtubule regrowth experiments show random nucleation of microtubules (labeled with 100nM SiR-tubulin overnight) that remain disorganized. Summarizing diagram shows PCM clusters and microtubule network in the indicated conditions.

Figure 6 – figure supplement 1. PCM dynamics and the effects of CAMSAP2 clustering on PCM organization in centrinone-treated RPE1 cells lacking AKAP450

(A) Time-lapse images illustrating the dynamics of PCM clusters (green, white arrows) and microtubules (SiR-tubulin, red) after nocodazole washout in centrinone-treated AKAP450 knockout RPE1 cells stably expressing GFP-CDK5RAP2. A single frame of the whole cell with numbered boxed areas indicating the location of enlarged time-lapse images is shown on the left. White arrows indicate moving PCM clusters after microtubules re-grow. Time is min:sec.

(B) Time-lapse images of centrinone-treated AKAP450 knockout RPE1 cells stably expressing GFP-CDK5RAP2. GFP-CDK5RAP2 forms small clusters that are dynamic before microtubules (SiR-tubulin, red) are disassembled by nocodazole treatment. Red arrows show that these clusters become immobile when microtubules are completely depolymerized (enlargements of the boxed areas shown

1720 in the bottom rows). GFP-CDK5RAP2-positive clusters are sites of microtubule nucleation after
1721 nocodazole washout and become dynamic again once microtubules re-grow. The maximum intensity
1722 projections include 100 or 400 frames, 200 ms/frame. Time is min:sec.

1723 (C) Summarizing diagram illustrating microtubule organization and the motility of PCM clusters in
1724 acentriolar AKAP450 knockout RPE1 cells.

1725 (D) Movement trajectories of PCM clusters in acentriolar AKAP450 knockout cells before and after 1
1726 hr treatment with 5µM dynapyrazole A (Dyna). 350 frames with a 2 s interval from the same cell were
1727 analyzed. Shaded areas represent the cell body.

1728 (E) Quantification of the length of the trajectories of moving PCM clusters. n=132 (without
1729 dynapyrazole A, from 5 cells) and 111 (after 1 hr dynapyrazole A treatment, from 4 cells) trajectories
1730 were analyzed for each condition. The statistical significance was determined by unpaired two-tailed
1731 Mann-Whitney test in Prism 9.1 (***$p<0.001$). Values represent mean±SD.

1732 (F) Immunofluorescence images of centrinone-treated AKAP450/CAMSAP2 knockout RPE1 cells
1733 transfected with 2FKBP-mCherry-CAMSAP2 and FRB-TagBFP-GCN4-ppKin14 and stained for the
1734 indicated proteins after overnight rapalog treatment. Zooms show the magnification of boxed area.

1735

1736 **Figure 6 – figure supplement 2. Pericentrin is required for PCM clustering in acentriolar AKAP450**
1737 **knockout RPE1 cells**

1738 Time-lapse images of centrinone-treated AKAP450 knockout RPE1 cells stably expressing GFP-
1739 CDK5RAP2 (green) depleted of pericentrin. GFP-CDK5RAP2 is diffusely distributed and does not form
1740 any clear clusters. Microtubule regrowth experiments show random nucleation of microtubules
1741 (labeled with 100nM SiR-tubulin overnight) that remain disorganized. Summarizing diagram shows
1742 PCM clusters and microtubule network in the indicated conditions.

1743

1744 **Figure 7 – figure supplement 1. Inducible CAMSAP2-driven microtubule rearrangement in**
1745 **AKAP450/CAMSAP2/p53/pericentrin knockout cell**

1746 Immunofluorescence images of centrinone-treated AKAP450/CAMSAP2/p53/pericentrin knockout
1747 cells expressing either FKBP-mCh-CAMSAP2 alone, FRB-GFP-ppKin14 alone or both, with or without
1748 rapalog treatment, and stained for microtubules (α-tubulin). Enlargements show the merged channels
1749 of the boxed areas.

1750

1751 **Figure 7 – figure supplement 2. Inducible CAMSAP2-driven radial microtubule rearrangement in**
1752 **AKAP450/CAMSAP2/p53/pericentrin knockout cell**

1753 (A) Time-lapse images of a centrinone-treated AKAP450/CAMSAP2/p53/pericentrin knockout cell
1754 transiently expressing 2FKBP-mCherry-CAMSAP2 and FRB-GFP-GCN4-ppKin14 imaged for 10 min (100
1755 frames, 6 s interval) prior to treatment with 100 nM rapalog and ~90 min after. Time is hr: min: sec.

1756 (B) Immunofluorescence images of centrinone-treated AKAP450/CAMSAP2/p53/pericentrin knockout
1757 and AKAP450/CAMSAP2/MMG/CDK5RAP2/p53/pericentrin knockout RPE1 cells, stained for the
1758 indicated markers. In the upper row, the cells were neither transfected nor treated with rapalog,
1759 whereas in the other panels, cells were transfected with 2FKBP-mCherry-CAMSAP2 and FRB-HA-
1760 GCN4-ppKin14 and treated with rapalog overnight. Zooms show the magnification of boxed areas.

1761

1762 **Figure 7 – figure supplement 3. Generation of the AKAP450/CAMSAP2/CDK5RAP2/MMG/**
1763 **p53/pericentrin knockout RPE1 cell line**

1764 (A) Diagram illustrating two sgRNA sites targeting p53 exon 4. The green and red boxes indicate the
1765 position of the PAM sites, and the predicted Cas9 cut sites are indicated by scissors. Genotyping results
1766 of the genomic mutation using gel-purified PCR product which covers exon 4 of the p53-encoding gene
1767 in AKAP450/CAMSAP2/MMG/CDK5RAP2/p53 knockout cell line are shown below.

1768 (B) Diagram illustrating the binding sites of p53 antibodies and the position of the mutation induced
1769 in p53-encoding gene.

1770 (C) Immunofluorescence images showing p53 staining in control and
1771 AKAP450/CAMSAP2/MMG/CDK5RAP2/p53 knockout cells.

1772 (D) Diagram illustrating two sgRNA sites targeting pericentrin exon 5. The green and red boxes indicate
1773 the position of the PAM sites, and the predicted Cas9 cut sites are indicated by scissors. Genotyping
1774 results of the genomic mutation using gel-purified PCR product which covers exon 5 of the pericentrin-
1775 encoding gene in AKAP450/CAMSAP2/MMG/CDK5RAP2/p53/pericentrin knockout cell line are shown
1776 below.

1777 (E) Diagram illustrating the binding domain of the pericentrin antibody and the positions of the
1778 mutations induced downstream of the Cas9 cut sites.

1779 (F) Immunofluorescence images showing the confirmation of pericentrin loss in control and
1780 AKAP450/CAMSAP2/MMG/CDK5RAP2/p53/pericentrin knockout cells.

1781 (G) Western blot illustrating the p53 and pericentrin loss in control and
1782 AKAP450/CAMSAP2/MMG/CDK5RAP2/p53/pericentrin knockout cells.

1783 (H) Immunofluorescence images of control and centrinone-treated AKAP450/CAMSAP2/
1784 CDK5RAP2/MMG/p53/pericentrin knockout cells staining microtubules (α-tubulin, red) and
1785 centrosomes (CEP192, green). Zooms show magnification of the boxed area.

1786

1787 **Legends to Supplemental Videos**

1788 **Video 1. Cell cycle progression in acentriolar AKAP450/CAMSAP2/p53 knockout cells**

1789 Cell cycle progression visualized by phase-contrast imaging of centrinone-treated
1790 AKAP450/CAMSAP2/p53 knockout RPE1 cells. The cells were imaged for ~15 hrs with 1min interval.
1791 Time is hh:mm.

1792 **Video 2. caMTOC disassembly during nocodazole treatment of acentriolar AKAP450/CAMSAP2**
1793 **knockout cells**

1794 PCM dynamics visualized by stable expression of GFP-CDK5RAP2 (green) in centrinone-treated
1795 AKAP450/CAMSAP2 knockout RPE1 cells. Microtubules were labeled overnight with 100 nM SiR-
1796 tubulin (red). The cell was imaged for ~3.5min (100 frames, 2 s interval) prior to the addition of 10 µM
1797 nocodazole. Time is min: sec.

1798 **Video 3. Depletion of pericentrin inhibits PCM clustering in acentriolar AKAP450/CAMSAP2**
1799 **knockout cells**

1800 A pericentrin-depleted acentriolar AKAP450/CAMSAP2 knockout cell stably expressing GFP-CDK5RAP2
1801 (green) and labeled overnight with 100 nM SiR-tubulin (red) was imaged for ~4.5 min (140 frames, 2 s
1802 time interval) prior to treatment with 10 µM nocodazole. Nocodazole was washed out at ~20 min
1803 (frame 591), when all microtubules were depolymerized. Time is hr: min: sec.

1804 **Video 4. CAMSAP2 distribution and dynamics in acentriolar AKAP450 knockout cells**

1805 An acentriolar AKAP450 knockout RPE1 cell transiently expressing mCherry-CAMSAP2 was imaged for
1806 15 hrs (900 frames, 1min interval). Time is hr:mm.

1807 **Video 5. PCM dynamics during nocodazole treatment and washout in acentriolar AKAP450 knockout**
1808 **cells**

1809 An acentriolar AKAP450 knockout RPE1 cell stably expressing GFP-CDK5RAP2 (green) and labeled
1810 overnight with 100 nM SiR-tubulin (red) was imaged for ~7min (200 frames, 2 s interval) prior to
1811 treatment with 10 µM nocodazole. Nocodazole was washed out at ~27 min (frame 801) when all
1812 microtubules were depolymerized. Time is min: sec.

1813 **Video 6. PCM dynamics in acentriolar AKAP450 knockout cells are inhibited by dynapyrazole**

1814 An acentriolar AKAP450 knockout RPE1 cell stably expressing GFP-CDK5RAP2 (green) and labeled
1815 overnight with 100 nM SiR-tubulin (red) was imaged for ~12 min (350 frames, 2 s interval) prior to the

1816 dynapyrazole treatment, treated with 5 µM Dynapyrazole A for 1h, and then the same cell was imaged
1817 for ~12 min. Time is min: sec.

1818 **Video 7. Depletion of pericentrin inhibits PCM clustering in acentriolar AKAP450 knockout cells**

1819 A pericentrin-depleted acentriolar AKAP450 knockout cell stably expressing GFP-CDK5RAP2 (green)
1820 and labeled overnight with 100 nM SiR-tubulin (red) was imaged for ~3 min (90 frames, 2 s time
1821 interval) prior to treatment with 10 µM nocodazole. Nocodazole was washed out at ~23 min (frame
1822 701) when all microtubules were depolymerized. Time is hr: min: sec.

1823 **Video 8. Inducible CAMSAP2-driven radial microtubule rearrangement in an**
1824 **AKAP450/CAMSAP2/p53/pericentrin knockout cell**

1825 An acentriolar AKAP450/CAMSAP2/p53/pericentrin knockout cell transiently expressing 2FKBP-
1826 mCherry-CAMSAP2 (red) and FRB-GFP-GCN4-ppKin14 (green) was imaged for 10 min (100 frames, 6 s
1827 interval) prior to treatment with 100 nM rapalog. Subsequently, the cell was imaged for ~1 hr and 35
1828 min after rapalog addition. Time is hr: min: sec.

1829 **Video 9. Cytosim simulations of PCM and microtubule self-organization**

1830 Example videos of our Cytosim simulations. Each simulation represents 1800 seconds of real time, and
1831 the last frame is shown in the panels of Figure 8. In all simulations, we considered a circular cell with
1832 a radius of 10 µm (gray line), containing microtubules (red), PCM complexes (green), and CAMSAP-
1833 kin14 complexes (blue). The videos correspond to panels A,B,C, D, I and J of Figure 8, as indicated.

1834

1835

1836 **Source data 1**

1837 **Uncropped Western blots shown in this manuscript**

1838 (A,B) Western blots showing that NEDD1 and CEP192 are present in centrinone-treated
1839 AKAP450/CAMSAP2 knockout cells shown in Figure 2 – figure supplement 1A.

1840 (C-J) Western blots showing the depletion of indicated proteins in centrinone-treated
1841 AKAP450/CAMSAP2 knockout cells shown in Figure 2 – figure supplement 1B.

1842 White dashed lines indicate where the blots were cut before incubation.

1843 (K) Western blot showing that 3 hrs treatment with dynaprazole A does not affect the expression of
1844 the endogenous dynein heavy chain and the dynactin large subunit p150Glued in centrinone-treated
1845 AKAP450/CAMSAP2 knockout cells shown in Figure 4D.

1846

1847 **Source data 2**

1848 **Uncropped Western blots shown in this manuscript**

1849 (A) Western blots showing the knockout of p53 from AKAP450/CAMSAP2 knockout cell line shown in
1850 Figure 2 – figure supplement 2F.

1851 (B) Western blots showing the knockout of pericentrin from AKAP450/CAMSAP2/p53 knockout cell
1852 line shown in Figure 2 – figure supplement 2K.

1853 (C-D) Western blots showing expression levels of CDK5RAP2, γ-tub, and ninein (NIN) in control (-CentB)
1854 and centrinone-treated AKAP450/CAMSAP2/p53 knockout and AKAP450/CAMSAP2/p53/PCNT
1855 knockout cell lines shown in Figure 2 – figure supplement 4B.

1856 (E) Western blots showing the knockout of AKAP450 and CAMSAP2 from EB1/EB3 mutant RPE1 cell
1857 line shown in Figure 2 – figure supplement 5B.

1858 (F) Western blots showing the knockout of pericentrin in AKAP450/CAMSAP2/CDK5RAP2/MMG/p53/
1859 knockout cell line shown in Figure 7 – figure supplement 3G.

1860 White dashed lines indicate where the blots were cut before incubation.

1861

1862 **Supplemental file 1. Cytosim configuration file for the simulations.**

1863 The configuration file was executed with a compiled Cytosim (www.cytosim.org) version June 2019**.**

1864 **Supplemental Table S1: Parameters with numerical values used in the Cytosim simulations.**

	Symbol	Value	Note	Reference
Cell				
Cell radius		10 µm		
Viscosity		1 pN s/ µm^2	Typical value for Cytosim simulations	(Kole et al., 2005; Letort et al., 2016)
Thermal energy	kT	4.2 pN nm		
Dynein				
Binding rate	k_{on}	5 s^{-1}	Typical order of magnitude	(Ohashi et al., 2019)
Force-free unbinding rate	k^0_{off}	0.1 s^{-1}		(Ohashi et al., 2019)
Detachment force	F_d	2		(Ohashi et al., 2019)
Binding range		75 nm	Estimated	
Force-free velocity	v_0	500 nm/s		(Brenner et al., 2020)
Stall force	F_s	4 pN		(Belyy et al., 2016)
Kin14				
Binding rate	k_{on}	1 s^{-1}	Typical order of magnitude for molecular motors	(Klumpp et al., 2015)
Force-free unbinding rate	k^0_{off}	1 s^{-1}	Assumption based on kinesin-1 value	(Berger et al., 2019)
Detachment force	F_d	3	Assumption based on kinesin-1 value	(Pyrpassopoulos et al., 2020)
Binding range		75 nm	Estimated	
Force-free velocity	v_0	800 nm/s	Assumption based on kinesin-1 value	(Carter and Cross, 2005)
Stall force	F_s	7 pN	Assumption based on kinesin-1 value	(Carter and Cross, 2005)
Microtubules				
Rigidity		20 pN µm^2		(Gibeaux et al., 2017)
Catastrophe rate	k_{cat}	0.026 s^{-1}	A similar value has been used in the reference	(Gibeaux et al., 2017)
Rescue rate		0	We ignore rescues	
Growing force		1.7 pN		(Dogterom and Yurke, 1997)

Growing speed	v_g	0.13 µm/s		(Burakov et al., 2003; Letort et al., 2016)
Shrinkage speed		0.272 µm/s		(Burakov et al., 2003; Letort et al., 2016)
Maximum length		7.5 µm	To avoid boundary effects	
Adhesive interactions of PCM complexes				
Binding rate		10 s^{-1}	Estimated	
Binding range		100 nm	Estimated	
Unbinding rate		0.01 s^{-1}	Estimated	
Detachment force		3 pN	Typical value, estimated	
General parameters				
Stiffness of all linking elements		100 pN/ µm	Typical value for molecular motors	(Gros et al., 2021; Letort et al., 2016)

1867 ***Key reagent or resource table***

Reagent type (species) or resource	Designation	Source or reference	Identifiers	Additional information
Antibody	anti-Pericentrin (mouse monoclonal)	Abcam	Abcam Cat# ab28144, RRID:AB_2160664	(1:500) for IF
Antibody	anti-Pericentrin (rabbit polyclonal)	Abcam	Abcam Cat# ab4448, RRID:AB_304461	(1:500) for IF; (1:1000) for WB
Antibody	anti-CDK5RAP2 (rabbit polyclonal)	Bethyl Laboratories	Bethyl Cat# A300-554A, RRID:AB_477974	(1:300) for IF; (1:1000) for WB
Antibody	anti-γ-tubulin (mouse monoclonal)	Sigma-Aldrich	Sigma-Aldrich: T6557; RRID:AB_477584	(1:300) for IF; (1:2000) for WB
Antibody	anti-γ-tubulin (rabbit polyclonal)	Sigma-Aldrich	Sigma-Aldrich:T3559, RRID:AB_477575	(1:300) for IF
Antibody	anti-NEDD1 (mouse monoclonal)	Abnova	Abnova Corporation Cat# H00121441-M05, RRID:AB_534956	(1:300) for IF
Antibody	anti-NEDD1 (rabbit polyclonal)	Rockland	Rockland Cat# 109-401-C38S, RRID:AB_10893219	(1:1000) for WB
Antibody	anti-Ninein (rabbit polyclonal)	BETHYL	Bethyl Cat# A301-504A, RRID:AB_999627	(1:300) for IF; (1:2000) for WB
Antibody	anti-Ninein (mouse monoclonal)	Santa Cruz Biotechnology	Santa Cruz Biotechnology Cat# sc-376420, RRID:AB_11151570	(1:300) for IF
Antibody	anti-Dynein HC (rabbit polyclonal)	Santa Cruz Biotechnology	Santa Cruz Biotechnology Cat# sc-9115, RRID:AB_2093483	(1:300) for IF; (1:500) for WB
Antibody	anti-p150Glued (mouse monoclonal)	BD Biosciences	BD Biosciences Cat# 610473, RRID:AB_397845	(1:100) for IF; (1:500) for WB
Antibody	anti-PCM1 (mouse monoclonal)	Santa Cruz Biotechnology	Santa Cruz Biotechnology Cat# sc-398365, RRID:AB_2827155	(1:300) for IF
Antibody	anti-PCM1 (rabbit polyclonal)	Bethyl Laboratories	Bethyl Cat# A301-150A, RRID:AB_873100	(1:300) for IF
Antibody	anti-AKAP450 (mouse monoclonal)	BD Biosciences	BD Biosciences Cat# 611518, RRID:AB_398978	(1:500) for WB
Antibody	anti-CAMSAP2 (rabbit polyclonal)	Novus	Novus:NBP1-21402; RRID:AB_1659977	(1:200) for IF; (1:1000) for WB
Antibody	anti-p53 (mouse monoclonal)	Santa Cruz Biotechnology	Santa Cruz Biotechnology Cat# sc-126, RRID:AB_628082	(1:300) for IF; (1:1000) for WB
Antibody	anti-p53 (rabbit polyclonal)	BETHYL	Bethyl Cat# A300-248A, RRID:AB_263349	(1:300) for IF
Antibody	anti-EB1 (mouse monoclonal)	BD Biosciences	BD Biosciences:610535; RRID:AB_397892	(1:400) for IF

Antibody	anti-EB3 (rabbit polyclonal)	Martin, et al., 2018;		(1:300) for IF
Antibody	anti-Centrin (mouse monoclonal)	Millipore	Millipore Cat# 04-1624, RRID:AB_10563501	(1:500) for IF
Antibody	anti-CEP120 (rabbit polyclonal)	Thermo Fisher Scientific	Thermo Fisher Scientific Cat# PA5-55985, RRID:AB_2639665	(1:300) for IF
Antibody	anti-CEP135 (rabbit polyclonal)	Sigma-Aldrich	Sigma-Aldrich:SAB4503685; RRID:AB_10746232	(1:300) for IF
Antibody	anti-CEP152 (rabbit polyclonal)	Abcam	Abcam, Cat # ab183911	(1:300) for IF; (1:1000) for WB
Antibody	anti-CEP170 (mouse monoclonal)	Thermo Fisher Scientific	Thermo Fisher Scientific Cat# 41-3200, RRID:AB_2533502	(1:200) for IF
Antibody	anti-CEP192 (rabbit polyclonal)	Bethyl Laboratories	Bethyl Cat# A302-324A, RRID:AB_1850234	(1:300) for IF; (1:1000) for WB
Antibody	anti-GM130 (mouse monoclonal)	BD Biosciences	BD Biosciences:610823; RRID:AB_398142	(1:300) for IF; (1:2000) for WB
Antibody	anti-α-tubulin YL1/2 (rat monoclonal)	Pierce	Pierce: MA1-80017; RRID:AB_2210201	(1:300) for IF
Antibody	anti-α-tubulin (mouse monoclonal)	Sigma-Aldrich	Sigma-Aldrich:T5168; RRID:AB_477579	(1:400) for IF
Antibody	anti-α-tubulin (rabbit monoclonal antibody)	Abcam	Abcam Cat# ab52866, RRID:AB_869989	(1:800) for IF
Antibody	Anti-β-tubulin (mouse monoclonal)	Sigma-Aldrich	Sigma-Aldrich Cat# T8660, RRID:AB_477590	(1:2000) for WB
Antibody	anti-CLASP1 (rabbit polyclonal)	(Akhmanova et al., 2001)		(1:400) for IF
Antibody	anti-CLASP2 (rabbit polyclonal)	(Akhmanova et al., 2001)		(1:400) for IF
Antibody	anti-CLIP-115 #2238 (rabbit polyclonal)	(Akhmanova et al., 2001)		(1:300) for IF
Antibody	anti-CLIP-170 #2360 (rabbit polyclonal)	(Akhmanova et al., 2001)		(1:300) for IF
Antibody	anti-ch-TOG (rabbit polyclonal)	(Charrasse et al., 1998)	Dr. Lynne Cassimeris (Lehigh University, USA)	(1:200) for IF
Antibody	anti-CPAP (rabbit polyclonal)	(Kohlmaier et al., 2009)	Dr. Pierre Gönczy (EPFL, Switzerland)	(1:200) for IF
Antibody	anti-CP110 (rabbit monoclonal)	Proteintech	Proteintech Cat# 12780-1-AP, RRID:AB_10638480	(1:300) for IF
Antibody	anti-KIF1C (rabbit polyclonal)	Cytoskeleton	Cytoskeleton Cat# AKIN11-A, RRID:AB_10708792	(1:300) for IF

Antibody	anti-KIF2A (rabbit polyclonal)	(Ganem and Compton, 2004)	Dr. Duane Compton (Geisel School of Medicine at Dartmouth, USA)	(1:300) for IF
Antibody	anti-HAUS2 (rabbit polyclonal)	(Lawo et al., 2009)	Dr. Laurence Pelletier (Lunenfeld-Tanenbaum Research Institute, Canada)	(1:200) for IF
Antibody	anti-BICD2 (rabbit polyclonal)	(Hoogenraad et al., 2003)		(1:2500) for WB
Antibody	anti-Actin (mouse monoclonal)	Millipore	Millipore Cat# MAB1501, RRID:AB_2223041	(1:4000) for WB
Antibody	anti-Ku80 (mouse monoclonal)	BD Biosciences	BD Biosciences Cat# 611360, RRID:AB_398882	(1:2000) for WB
Antibody	anti-LaminA/C (mouse monoclonal)	BD Biosciences	BD Biosciences Cat# 612162, RRID:AB_399533	(1:400) for IF
Antibody	anti-Cytochrome C (mouse monoclonal)	BD Biosciences	BD Biosciences Cat# 556432, RRID:AB_396416	(1:300) for IF
Antibody	anti-Calnexin (rabbit polyclonal)	Abcam	Abcam Cat# ab22595, RRID:AB_2069006	(1:300) for IF
Antibody	Anti-Lamtor4 (rabbit monoclonal)	Cell Signaling (CST)/Bioke	Cell Signaling Technology Cat# 12284, RRID:AB_2797870	(1:800) for IF
	Anti-Tom20 (mouse monoclonal)	BD Biosciences	BD Biosciences Cat# 612278, RRID:AB_399595	(1:200) for IF
Antibody	IRDye 800CW/680LT secondaries	Li-Cor Biosciences	LI-COR Biosciences Cat# 926-32219, RRID:AB_1850025' LI-COR Biosciences Cat# 926-68020, RRID:AB_10706161; LI-COR Biosciences Cat# 926-32211, RRID:AB_621843; LI-COR Biosciences Cat# 926-68021, RRID:AB_10706309	(1:5000) for WB
Antibody	Alexa Fluor 405–, 488–, and 594– secondaries	Molecular Probes/ Thermo Fisher Scientific	Molecular Probes Cat# A-11007, RRID:AB_141374; Cat# A-11034, RRID:AB_2576217; Cat# A32723, RRID:AB_2633275; Cat# A-31553, RRID:AB_221604; Cat# A-11029, RRID:AB_138404; Cat# A-11032, RRID:AB_2534091; Cat# A-11006, RRID:AB_141373; Thermo Fisher Scientific Cat# A-11012, RRID:AB_2534079	(1:500) for IF
Sequence-based reagent	siRNA against PCNT #1	(Gavilan et al., 2018)	5'-AAAAGCUCUGAUUUAUCAAAAGAAG-3'	

Sequence-based reagent	siRNA against PCNT #2	(Gavilan et al., 2018)	5'-UGAUUGGACGUCAUCCAAUGAGAAA-3'	
Sequence-based reagent	siRNA against PCNT #3	(Tibelius et al., 2009)	5'-GCAGCUGAGCUGAAGGAGA-3'	
Sequence-based reagent	siRNA against CDK5RAP2	(Fong et al., 2008)	5'-UGGAAGAUCUCCUAACUAA-3'	
Sequence-based reagent	siRNA against γ-tubulin #1	(Luders et al., 2006)	5'-GGAGGACAUGUUCAAGGAA-3'	
Sequence-based reagent	siRNA against γ-tubulin #2	(Vinopal et al., 2012)	5'-CGCAUCUCUUUCUCAUAU-3'	
Sequence-based reagent	siRNA against Ninein	(Goldspink et al., 2017)	5'-CGGUACAAUGAGUGUAGAAUU-3'	
Sequence-based reagent	siRNA against PCM1	(Wang et al., 2013)	5'-UCAGCUUCGUGAUUCUCAG-3'	
Sequence-based reagent	siRNA against CEP152	(Cizmecioglu et al., 2010; Komarova et al., 2005)	5'-GCGGAUCCAACUGGAAAUCUA-3'	
Sequence-based reagent	siRNA against CEP120	(Ganem et al., 2005; Lin et al., 2013)	5'-AAUAUAUCUUCUUGCAUCUCCUUCC-3'	
Sequence-based reagent	siRNA against CEP192	(Sonnen et al., 2013)	5'-CAGAGGAAUCAAUAAUAAA -3'	
Sequence-based reagent	siRNA against NEDD1 #1	(Luders et al., 2006)	5'-GCAGACAUGUGUCAAUUUA-3'	
Sequence-based reagent	siRNA against NEDD1 #2	(Haren et al., 2006)	5'-GGGCAAAAGCAGACAUGUG-3'	
Sequence-based reagent	siRNA against DHC #1	(Splinter et al., 2010)	5'-CGUACUCCCGUGAUUGAUG-3'	
Sequence-based reagent	siRNA against DHC #2	(Splinter et al., 2010)	5'-GCCAAAAGUUACAGACUUU-3'	
Sequence-based reagent	siRNA against CAMSAP2	(Jiang et al., 2014)	5'-GUACUGGAUAAAUAAGGUA-3'	
Sequence-based reagent	siRNA against CEP170	(Stolz et al., 2015)	5'-GAAGGAAUCCUCCAAGUCA-3'	
Sequence-based reagent	siRNA against CPAP	(Tang et al., 2009)	5'-AGAAUUAGCUCGAAUAGAA-3'	
Sequence-based reagent	siRNA against CLIP170 #1	(Lansbergen et al., 2004; Mimori-Kiyosue et al., 2005)	5'-GGAGAAGCAGCAGCACAUU-3'	

Sequence-based reagent	siRNA against CLIP170 #2	(Lansbergen et al., 2004; Mimori-Kiyosue et al., 2005)	5'-UGAAGAUGUCAGGAGAUAA-3'	
Sequence-based reagent	siRNA against CLIP115 #1	(Lansbergen et al., 2004)	5'-GGCACAGCAUGAGCAGUAU-3'	
Sequence-based reagent	siRNA against CLIP115 #2	(Lansbergen et al., 2004)	5'-CUGGAAAUCCAAGCUGGAC-3'	
Sequence-based reagent	siRNA against ch-TOG:	(Cassimeris and Morabito, 2004; Lansbergen et al., 2004)	5'-GAGCCCAGAGUGGUCCAAA-3'	
Sequence-based reagent	siRNA against EB1	(Grigoriev et al., 2008; Lansbergen et al., 2004)	5'-AUUCCAAGCUAAGCUAGAA-3'	
Sequence-based reagent	siRNA against EB3	(Cassimeris and Morabito, 2004; Komarova et al., 2005)	5'-CUAUGAUGGAAAGGAUUAC-3'	
Sequence-based reagent	siRNA against KIF2A	(Ganem et al., 2005; Grigoriev et al., 2008)	5'-GGCAAAGAGAUUGACCUGG-3'	
Sequence-based reagent	siRNA against CP110	(Cizmecioglu et al., 2010; Spektor et al., 2007)	5'-AAGCAGCAUGAGUAUGCCAGU-3'	
Sequence-based reagent	siRNA against Luciferase	(Lansbergen et al., 2004; Lin et al., 2013)	5'-CGUACGCGGAAUACUUCGA-3'	
Sequence-based reagent	sgRNA target CAMSAP2	(Lansbergen et al., 2004; Wu et al., 2016)	5'-gCATGATCGATACCCTCATGA-3	
Sequence-based reagent	sgRNA target p53 e2 #1	This study	5′-gCGTCGAGCCCCCTCTGAGTC-3′;	
Sequence-based reagent	sgRNA target p53 e4 #2	This study	5′-gCCATTGTTCAATATCGTCCG-3′;	
Sequence-based reagent	sgRNA target PCNT e5-1 #1	This study	5′-gAGACGGCATTGACGGAGCTG-3′;	

Sequence-based reagent	sgRNA target PCNT e5-2 #2	This study	5′-GCTCAACAGCCGGCGTGCCC-3′;	
Sequence-based reagent	p53 KO sequencing primer F	This study	5′-TCAGACACTGGCATGGTGTT-3′;	
Sequence-based reagent	p53 KO sequencing primer R	This study	5′-AGAAATGCAGGGGGATACGG-3′;	
Sequence-based reagent	PCNT KO sequencing primer F	This study	5′-ATACAGCGAGGGAATTCGGG-3′;	
Sequence-based reagent	PCNT KO sequencing primer R	This study	5′-TAGAATGCCCACACCGAGC-3′;	
Chemical compound	Centrinone B	Tocris Bioscience	Tocris Bioscience Cat # 5690	125 nM
Chemical compound	Nocodazole	Sigma-Aldrich	Sigma-Aldrich, Cat # M1404-10MG	10 µM
Chemical compound	Rapalog (A/C Heterodimerizer)	Takara	Takara, Cat # 635056	50 nM (fixation), 100 nM (live imaging).
Chemical compound	Dynapyrazole A	Sigma-Aldrich	Sigma-Aldrich, Cat # SML2127-25MG	5 µM
Chemical compound	BI2536	Selleckchem	Selleckchem, Cat # S1109	500 nM
Chemical compound	Thymidine	Sigma-Aldrich	Sigma-Aldrich, Cat # T9250-25G	5 mM
Chemical compound	proTAME	Boston Biochem	Boston Biochem, Cat # I-440	5 µM
Chemical compound	Brefeldin A	Peptrotech	Peptrotech, Cat # 2031560	5 µg/ml
Chemical compound	SiR-tubulin	Tebu-bio	Tebu-bio, Cat # SC002	100 nM
Software, algorithm	ImageJ radiality plugin	https://github.com/ekatrukha/radialitymap	Katrukha, 2017. radialitymap. Github. https://github.com/ekatrukha/radialitymap cf1e78f	
Recombinant DNA reagent	pLVX-IRES-puro (plasmid)	Clontech		
Recombinant DNA reagent	pB80-FRB-TagBFP-GCN4-ppKin14 (plasmid)	This work		

Recombinant DNA reagent	pB80-FRB-GFP-GCN4-ppKin14 (plasmid)	This work		
Recombinant DNA reagent	pB80-FRB-HA-GCN4-ppKin14 (plasmid)	This work		
Recombinant DNA reagent	2FKBP-mCherry-CAMSAP2 (plasmid)	This work		
Recombinant DNA reagent	GFP-PCNT (plasmid)	This work		
Recombinant DNA reagent	GST-DmKHC(1-421)-mNeonGreen (plasmid)	This work		
Cell line (Homo sapiens)	hTERT-RPE-1	ATCC	CRL-4000	
Cell line (Homo sapiens)	hTERT-RPE-1 AKAP450 knockout	(Wu et al., 2016)		
Cell line (Homo sapiens)	hTERT-RPE-1 AKAP450/CAMSAP2 knockout	(Wu et al., 2016)		
Cell line (Homo sapiens)	hTERT-RPE-1 AKAP450/CAMSAP2/p53 knockout	This work		
Cell line (Homo sapiens)	hTERT-RPE-1 AKAP450/CAMSAP2/p53/Pericentrin knockout	This work		
Cell line (Homo sapiens)	hTERT-RPE-1 AKAP450/CAMSAP2/EB1/EB3 mutant	This work		
Cell line (Homo sapiens)	hTERT-RPE-1 AKAP450/CAMSAP2/CDK5RAP2/MMG/p53/Pericentrin knockout	This work		

Cell line (Homo sapiens)	HEK 293T	ATCC	CRL-11268	

Figure 1

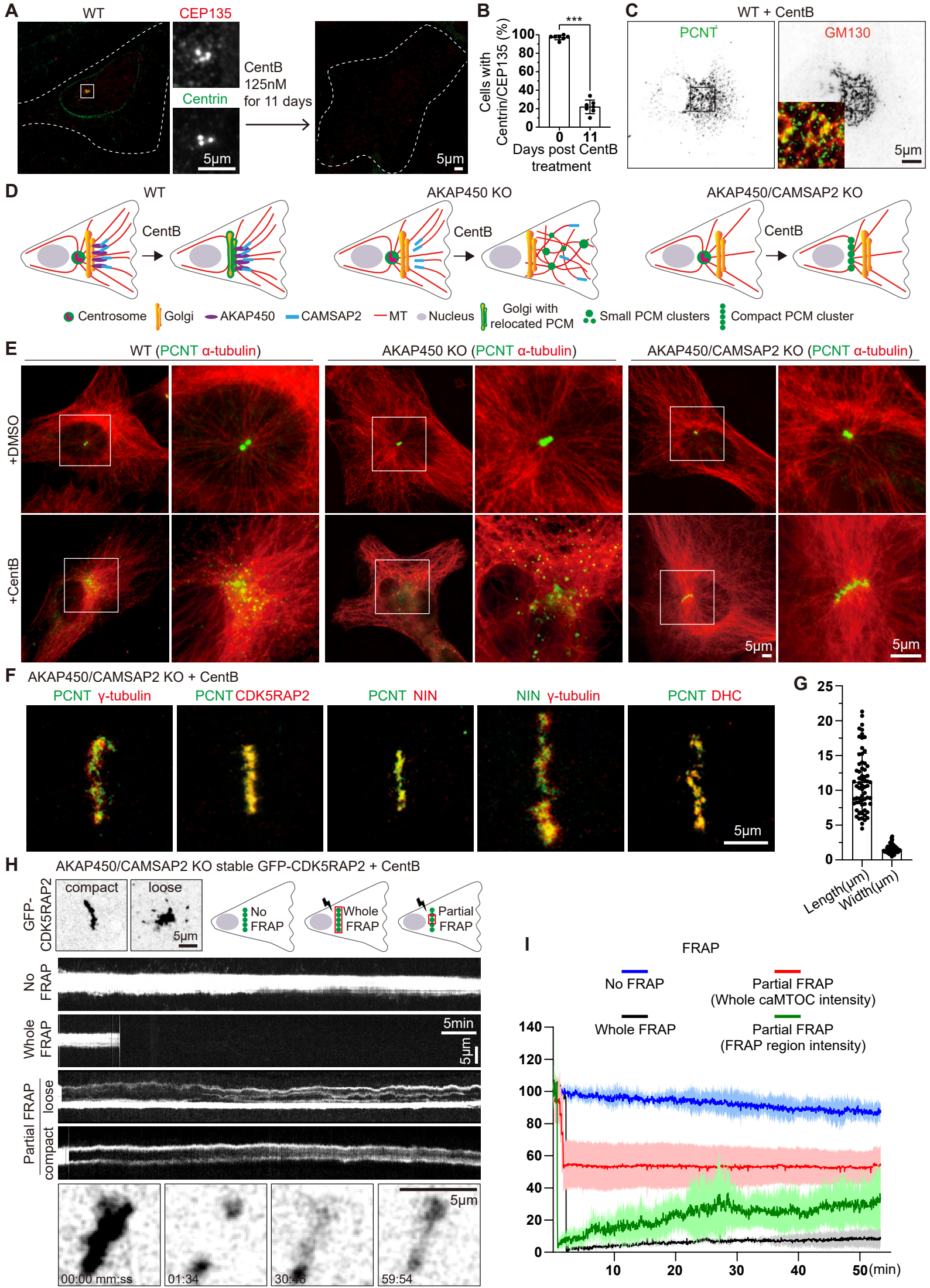
A
WT
CEP135
Centrin
5μm
CentB
125nM
for 11 days
5μm
B
***
Cells with Centrin/CEP135 (%)
100
80
60
40
20
0
0
11
Days post CentB treatment
C
WT + CentB
PCNT
GM130
5μm
D
WT
AKAP450 KO
AKAP450/CAMSAP2 KO
CentB
Centrosome
Golgi
AKAP450
CAMSAP2
MT
Nucleus
Golgi with relocated PCM
Small PCM clusters
Compact PCM cluster
E
WT (PCNT α-tubulin)
AKAP450 KO (PCNT α-tubulin)
AKAP450/CAMSAP2 KO (PCNT α-tubulin)
+DMSO
+CentB
5μm
5μm
F
AKAP450/CAMSAP2 KO + CentB
PCNT γ-tubulin
PCNT CDK5RAP2
PCNT NIN
NIN γ-tubulin
PCNT DHC
5μm
G
25
20
15
10
5
0
Length(μm)
Width(μm)
H
AKAP450/CAMSAP2 KO stable GFP-CDK5RAP2 + CentB
GFP-CDK5RAP2
compact
loose
5μm
No FRAP
Whole FRAP
Partial FRAP
No FRAP
Whole FRAP
5min
5μm
Partial FRAP
loose
compact
5μm
00:00 mm:ss
01:34
30:46
59:54
I
FRAP
No FRAP
Partial FRAP (Whole caMTOC intensity)
Whole FRAP
Partial FRAP (FRAP region intensity)
140
120
100
80
60
40
20
0
10
20
30
40
50 (min)

Figure 2

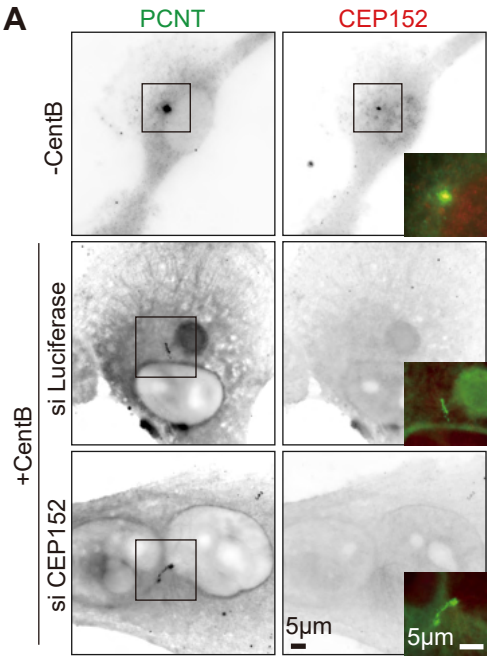

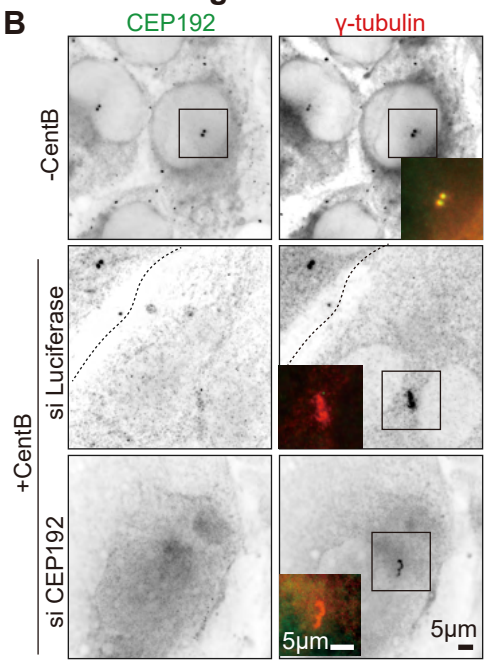

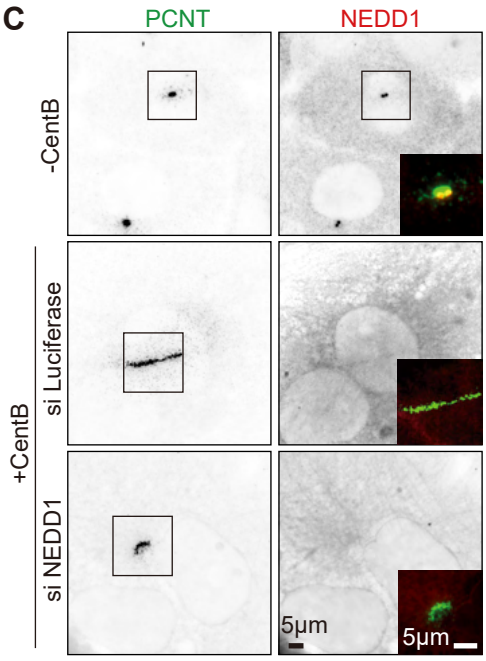

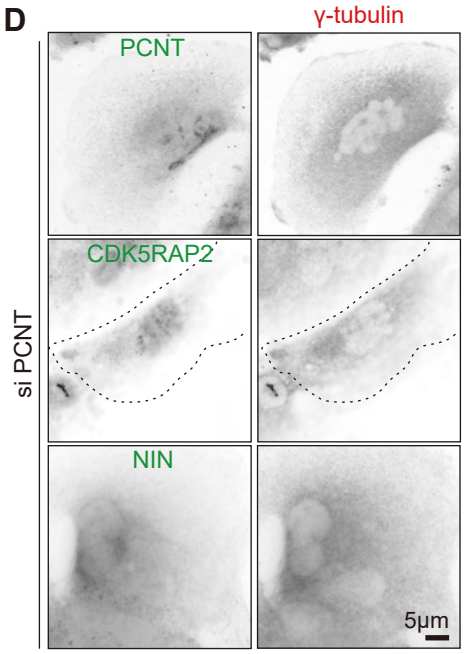

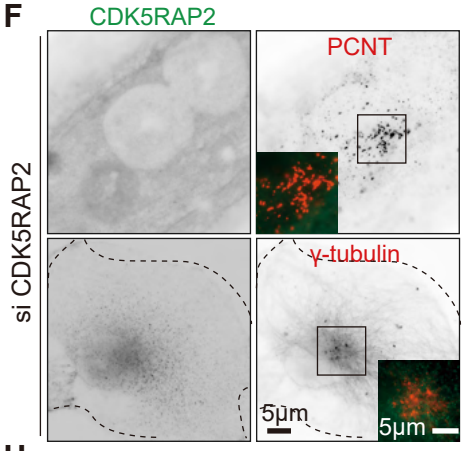

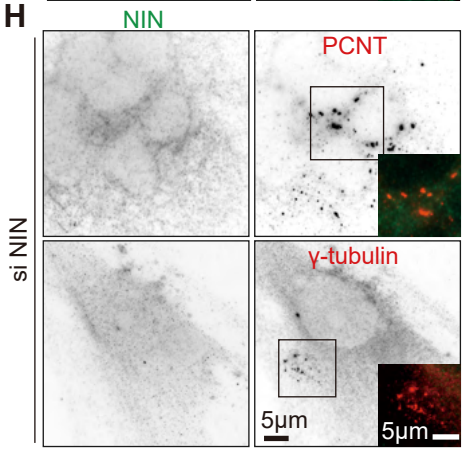

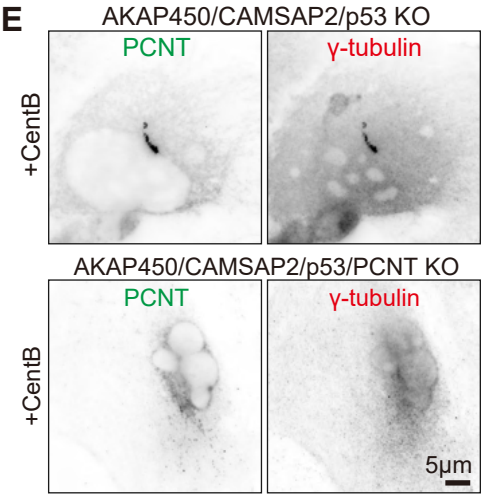

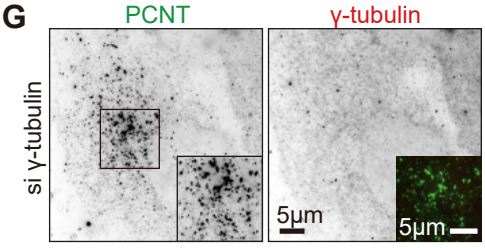

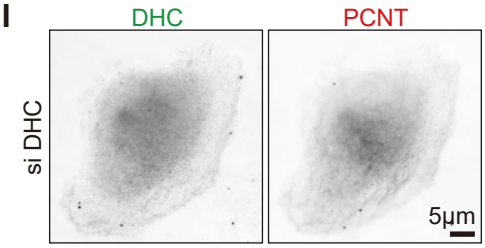

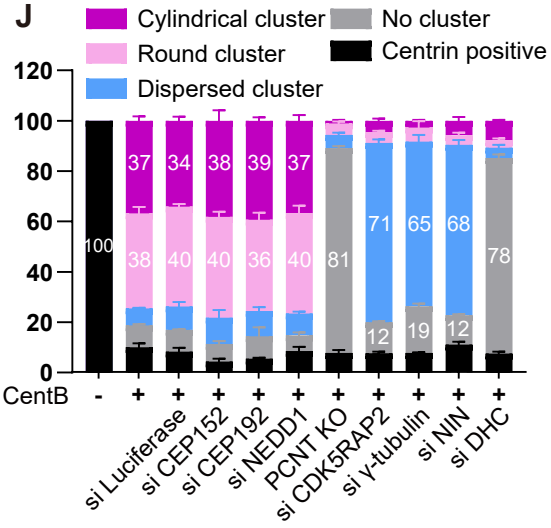

K

AKAP450/CAMSAP2 KO

		Present in caMTOC	Loss affects caMTOC
γ-TuRC binding	PCNT	+	+
	CDK5RAP2	+	+
	NEDD1	-	-
	γ-tubulin	+	+
	HAUS2	+	NT
Pericentriolar matrix	CEP170	+	NT
	CEP152	-	-
	Ninein	+	+
	CEP192	-	-
Centriole	CPAP	+	-
	Centrin	-	NT
	CP110	+	-
	CEP135	-	NT
	CEP120	+	-
Dynein/ Dynactin	DHC	+	+
	p150Glued	+	NT
Microtubule associated	CLASP1	+	NT
	CLASP2	+	NT
	CLIP115	+	-
	CLIP170	+	-
	chTOG	+	-
	KIF2A	+	-
	KIF1C	+	NT
	EB1	-	-
	EB3	-	-
Centriolar satelites	PCM1	+	-

NT=not tested

Figure 3

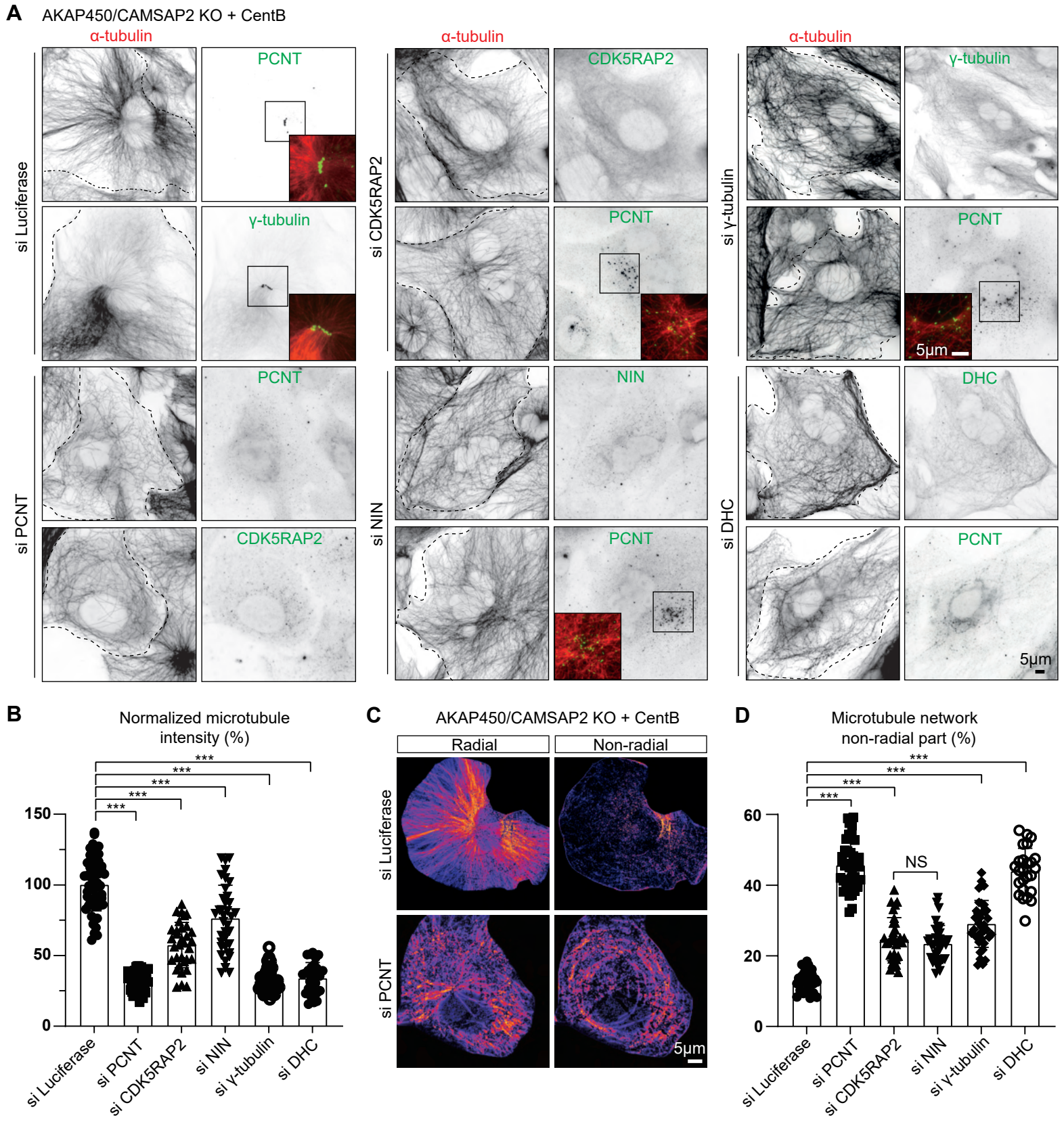
A
AKAP450/CAMSAP2 KO + CentB
α-tubulin
PCNT
γ-tubulin
CDK5RAP2
NIN
DHC
si Luciferase
si PCNT
si CDK5RAP2
si NIN
si γ-tubulin
si DHC
5μm
B
Normalized microtubule intensity (%)
150
100
50
0
***
si Luciferase
si PCNT
si CDK5RAP2
si NIN
si γ-tubulin
si DHC
C
AKAP450/CAMSAP2 KO + CentB
Radial
Non-radial
D
Microtubule network non-radial part (%)
60
40
20
0
NS

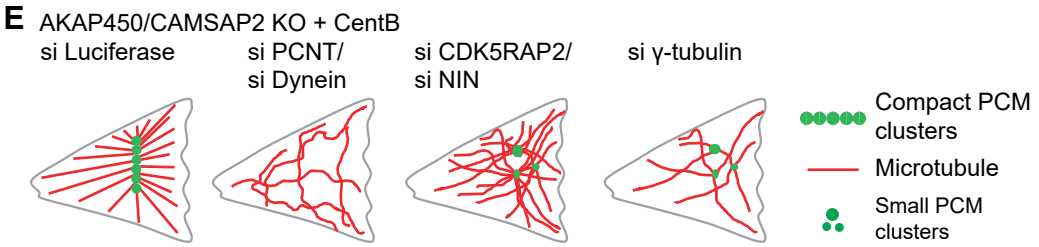
E
AKAP450/CAMSAP2 KO + CentB
si Luciferase
si PCNT/
si Dynein
si CDK5RAP2/
si NIN
si γ-tubulin
Compact PCM clusters
Microtubule
Small PCM clusters

Figure 4

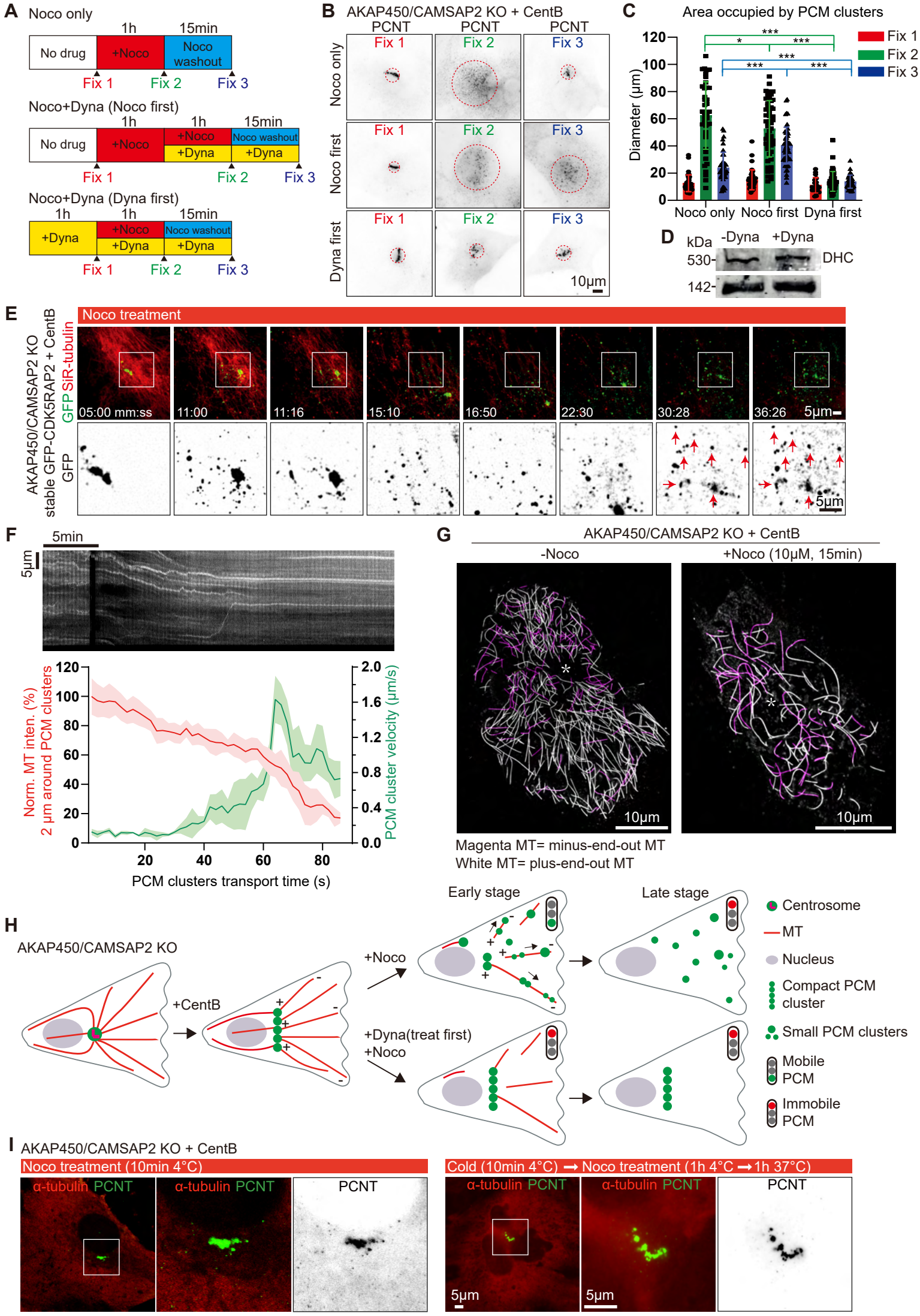
A
Noco only
1h
15min
No drug
+Noco
Noco washout
Fix 1
Fix 2
Fix 3
Noco+Dyna (Noco first)
1h
1h
15min
No drug
+Noco
+Noco
+Dyna
Noco washout
+Dyna
Fix 1
Fix 2
Fix 3
Noco+Dyna (Dyna first)
1h
1h
15min
+Dyna
+Noco
+Dyna
Noco washout
+Dyna
Fix 1
Fix 2
Fix 3
B
AKAP450/CAMSAP2 KO + CentB
PCNT
PCNT
PCNT
Noco only
Noco first
Dyna first
Fix 1
Fix 2
Fix 3
10μm
C
Area occupied by PCM clusters
Diameter (μm)
Fix 1
Fix 2
Fix 3
Noco only
Noco first
Dyna first
D
kDa
-Dyna
+Dyna
530-
142-
DHC
E
Noco treatment
AKAP450/CAMSAP2 KO
stable GFP-CDK5RAP2 + CentB
GFP SiR-tubulin
GFP
05:00 mm:ss
11:00
11:16
15:10
16:50
22:30
30:28
36:26
5μm
5μm
F
5min
5μm
Norm. MT inten. (%)
2 μm around PCM clusters
PCM cluster velocity (μm/s)
PCM clusters transport time (s)
G
AKAP450/CAMSAP2 KO + CentB
-Noco
+Noco (10μM, 15min)
10μm
10μm
Magenta MT= minus-end-out MT
White MT= plus-end-out MT
H
AKAP450/CAMSAP2 KO
+CentB
+Noco
+Dyna(treat first)
+Noco
Early stage
Late stage
Centrosome
MT
Nucleus
Compact PCM cluster
Small PCM clusters
Mobile PCM
Immobile PCM
I
AKAP450/CAMSAP2 KO + CentB
Noco treatment (10min 4°C)
α-tubulin PCNT
α-tubulin PCNT
PCNT
Cold (10min 4°C) → Noco treatment (1h 4°C → 1h 37°C)
α-tubulin PCNT
α-tubulin PCNT
PCNT
5μm
5μm

Figure 5

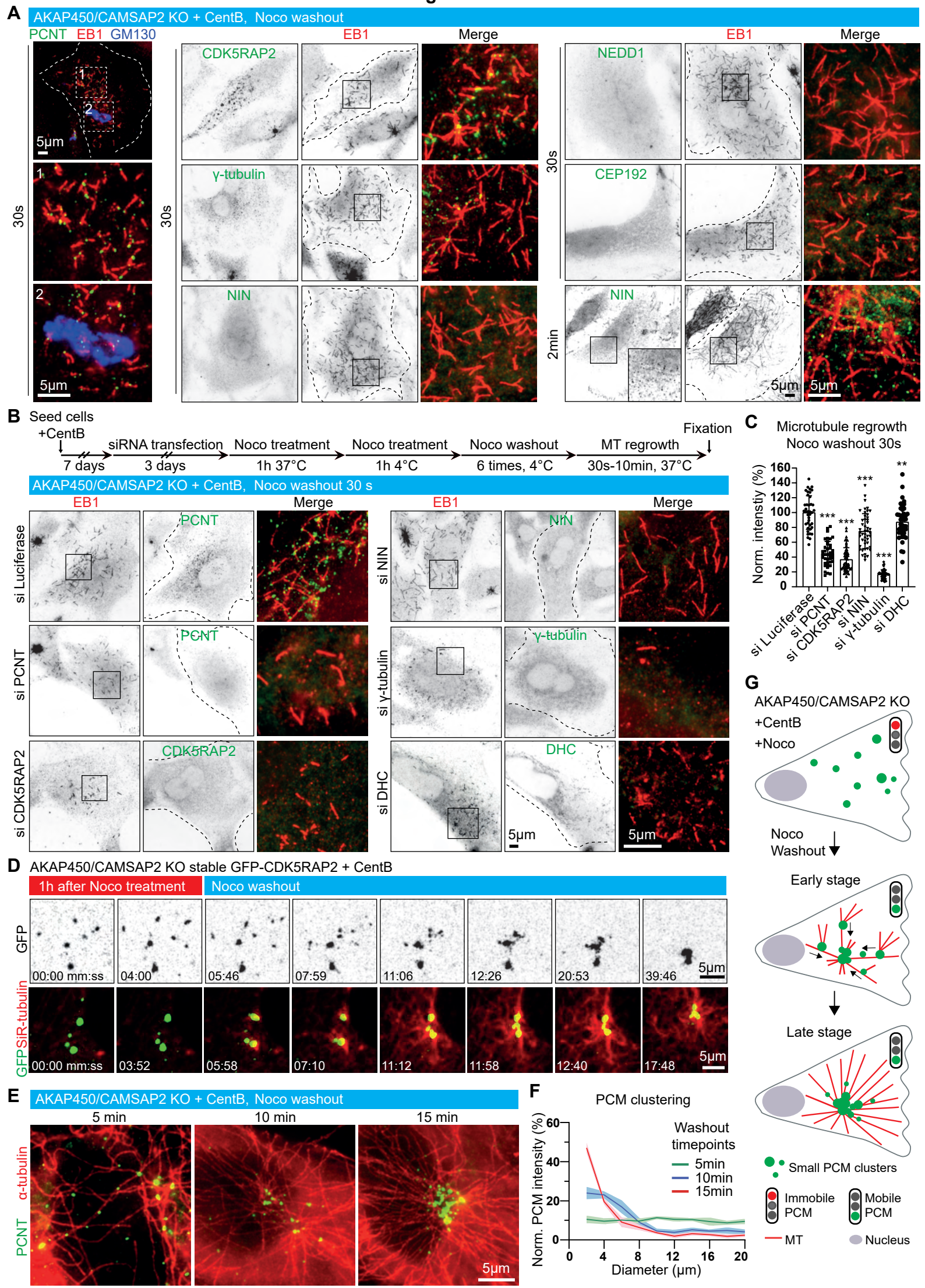
A
AKAP450/CAMSAP2 KO + CentB, Noco washout
PCNT EB1 GM130
EB1
Merge
CDK5RAP2
γ-tubulin
NIN
NEDD1
CEP192
30s
2min
5μm
B
Seed cells
+CentB
siRNA transfection
Noco treatment
Noco treatment
Noco washout
MT regrowth
Fixation
7 days
3 days
1h 37°C
1h 4°C
6 times, 4°C
30s-10min, 37°C
AKAP450/CAMSAP2 KO + CentB, Noco washout 30 s
si Luciferase
si PCNT
si CDK5RAP2
si NIN
si γ-tubulin
si DHC
C
Microtubule regrowth
Noco washout 30s
Norm. intensity (%)
si Luciferase
si PCNT
si CDK5RAP2
si NIN
si γ-tubulin
si DHC
D
AKAP450/CAMSAP2 KO stable GFP-CDK5RAP2 + CentB
1h after Noco treatment
Noco washout
GFP
GFP SiR-tubulin
00:00 mm:ss
04:00
05:46
07:59
11:06
12:26
20:53
39:46
03:52
05:58
07:10
11:12
11:58
12:40
17:48
E
AKAP450/CAMSAP2 KO + CentB, Noco washout
5 min
10 min
15 min
α-tubulin
PCNT
F
PCM clustering
Norm. PCM intensity (%)
Washout timepoints
5min
10min
15min
Diameter (μm)
G
AKAP450/CAMSAP2 KO
+CentB
+Noco
Noco Washout
Early stage
Late stage
Small PCM clusters
Immobile PCM
Mobile PCM
MT
Nucleus

Figure 6

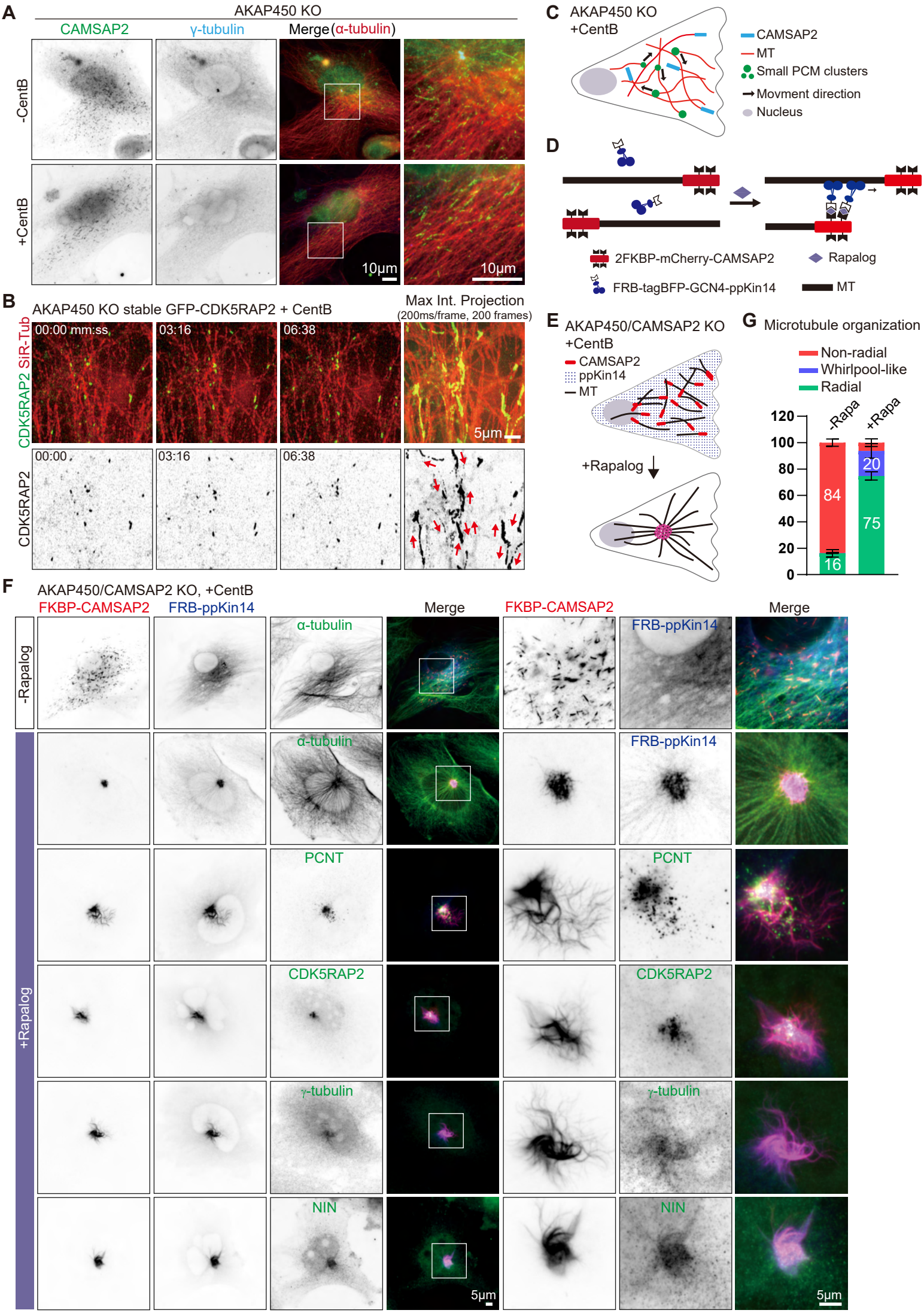
A
AKAP450 KO
CAMSAP2
γ-tubulin
Merge (α-tubulin)
-CentB
+CentB
10μm
10μm
B
AKAP450 KO stable GFP-CDK5RAP2 + CentB
Max Int. Projection
(200ms/frame, 200 frames)
CDK5RAP2 SiR-Tub
00:00 mm:ss
03:16
06:38
5μm
CDK5RAP2
00:00
03:16
06:38
C
AKAP450 KO
+CentB
CAMSAP2
MT
Small PCM clusters
Movment direction
Nucleus
D
2FKBP-mCherry-CAMSAP2
Rapalog
FRB-tagBFP-GCN4-ppKin14
MT
E
AKAP450/CAMSAP2 KO
+CentB
CAMSAP2
ppKin14
MT
+Rapalog
G
Microtubule organization
Non-radial
Whirlpool-like
Radial
-Rapa
+Rapa
120
100
80
60
40
20
0
84
16
20
75
F
AKAP450/CAMSAP2 KO, +CentB
FKBP-CAMSAP2
FRB-ppKin14
Merge
FKBP-CAMSAP2
Merge
-Rapalog
+Rapalog
α-tubulin
FRB-ppKin14
PCNT
CDK5RAP2
γ-tubulin
NIN
5μm
5μm

Figure 7

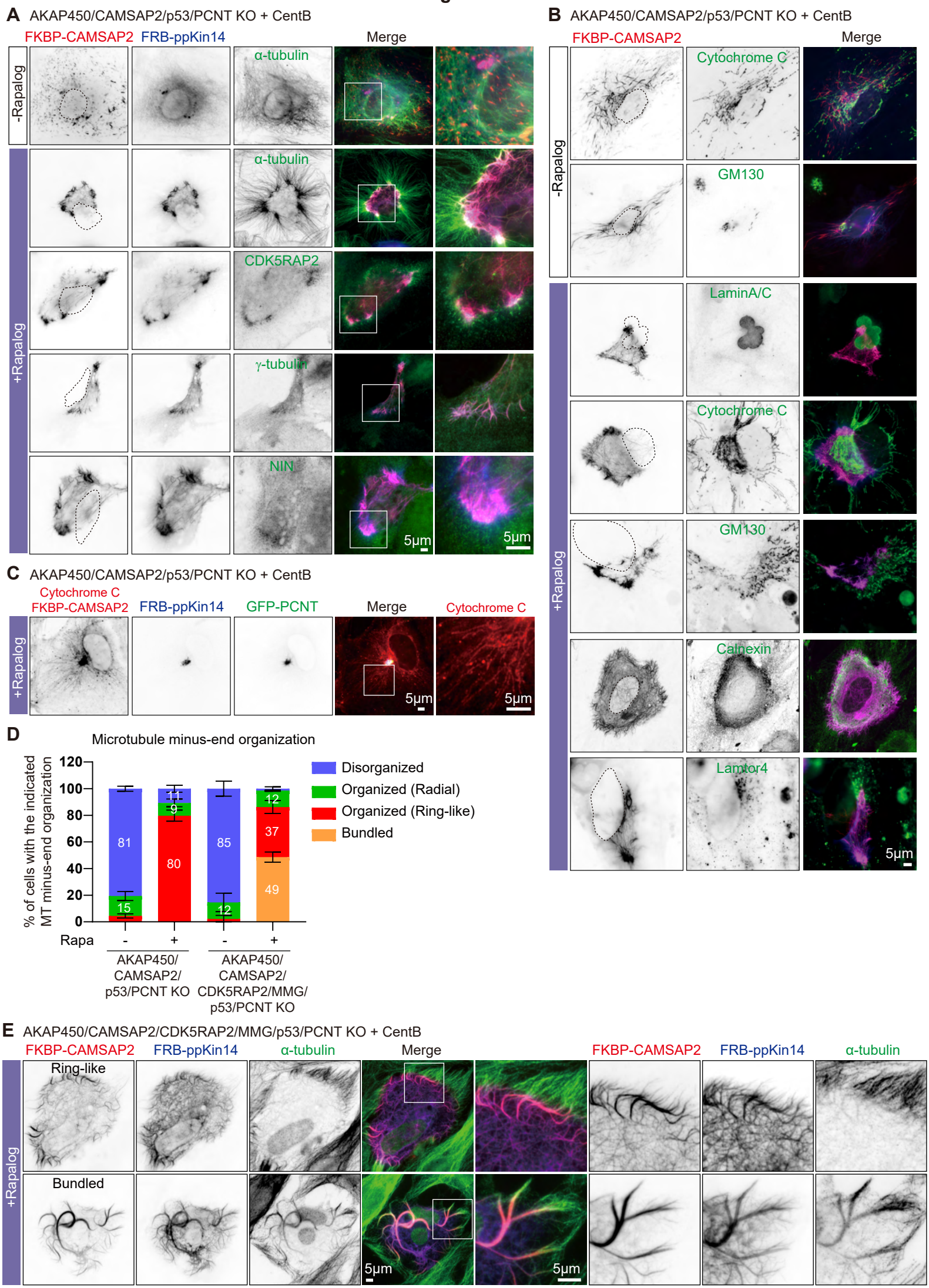
A AKAP450/CAMSAP2/p53/PCNT KO + CentB
FKBP-CAMSAP2
FRB-ppKin14
Merge
-Rapalog
+Rapalog
α-tubulin
CDK5RAP2
γ-tubulin
NIN
5μm
B AKAP450/CAMSAP2/p53/PCNT KO + CentB
FKBP-CAMSAP2
Merge
Cytochrome C
GM130
LaminA/C
Calnexin
Lamtor4
C AKAP450/CAMSAP2/p53/PCNT KO + CentB
Cytochrome C
FKBP-CAMSAP2
FRB-ppKin14
GFP-PCNT
Merge
D
Microtubule minus-end organization
% of cells with the indicated MT minus-end organization
Disorganized
Organized (Radial)
Organized (Ring-like)
Bundled
Rapa
AKAP450/ CAMSAP2/ p53/PCNT KO
AKAP450/ CAMSAP2/ CDK5RAP2/MMG/ p53/PCNT KO
E AKAP450/CAMSAP2/CDK5RAP2/MMG/p53/PCNT KO + CentB
Ring-like
Bundled

Figure 8

A
300 adhesive PCM complexes
(all MT-nucleating)

B
300 non-adhesive PCM complexes
(all MT-nucleating)

C
300 adhesive PCM complexes
(50 MT-nucleating)
300 immobile MTs

D
300 strongly adhesive PCM complexes
(50 MT-nucleating)
300 immobile MTs

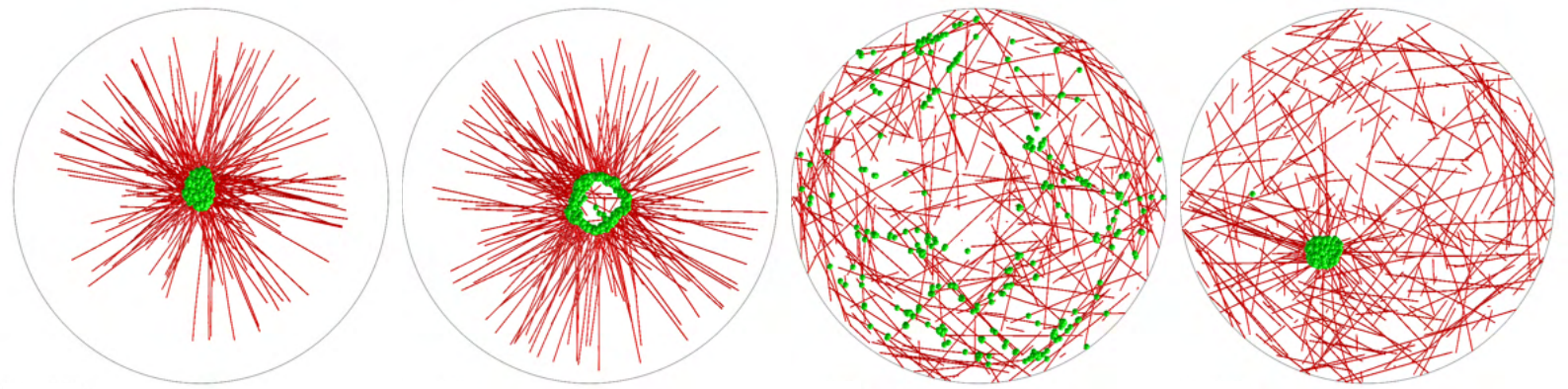

E

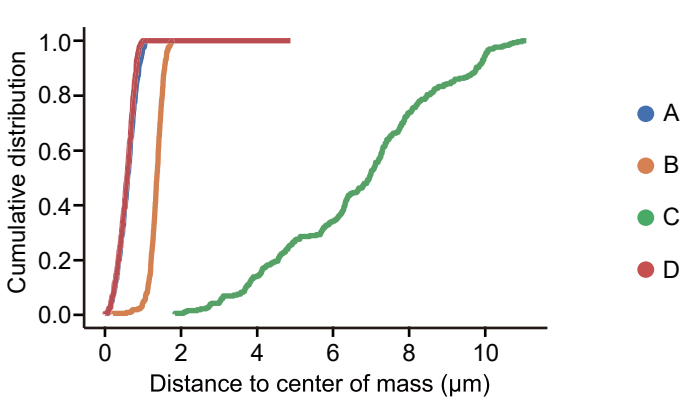

F

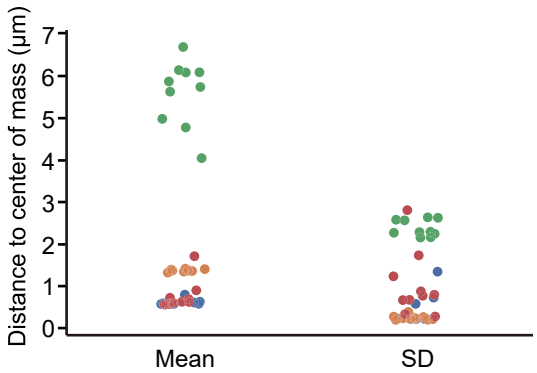

G
300 non-adhesive CAMSAP-kin14
complexes (all MT-nucleating)

H
300 adhesive CAMSAP-kin14
complexes (all MT-nucleating)

I
150 non-adhesive CAMSAP-kin14
complexes (all MT-nucleating)
150 adhesive PCM complexes
(all MT-nucleating)

J
150 non-adhesive CAMSAP-kin14
complexes (all MT-nucleating)
150 non-adhesive PCM complexes
(all MT-nucleating)

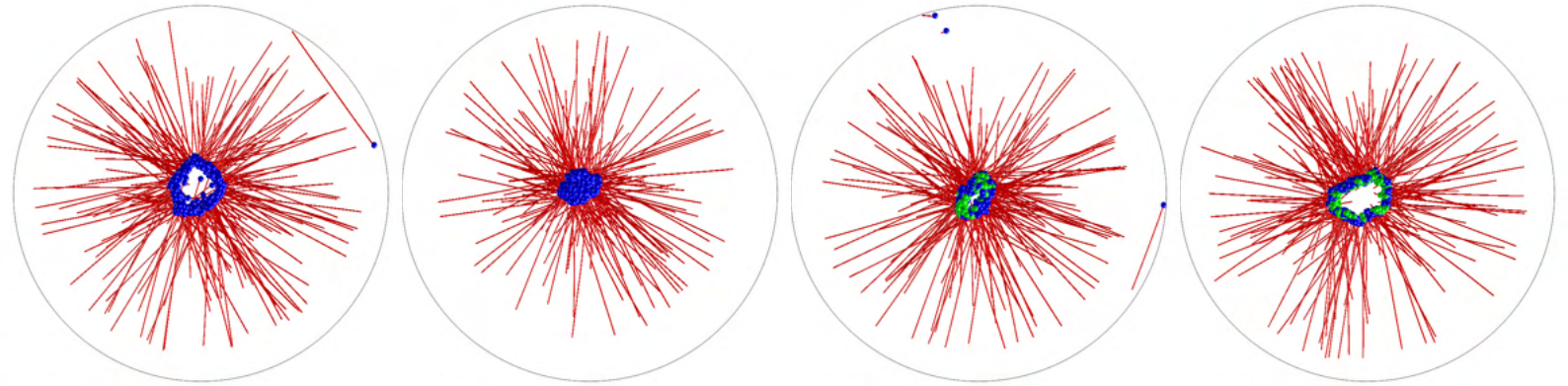

K

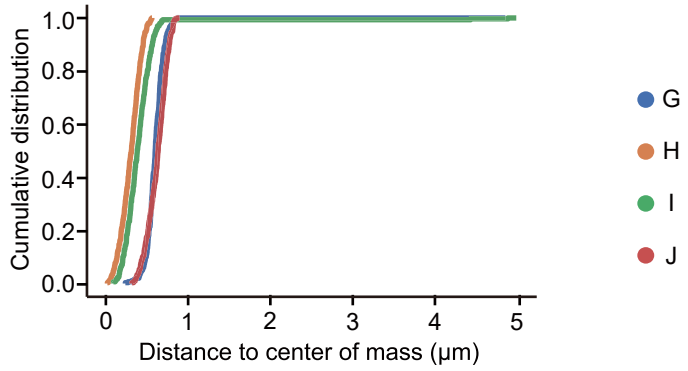

L

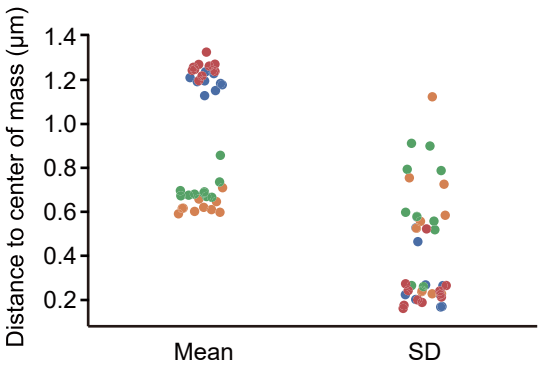

Figure 1 - figure supplement 1

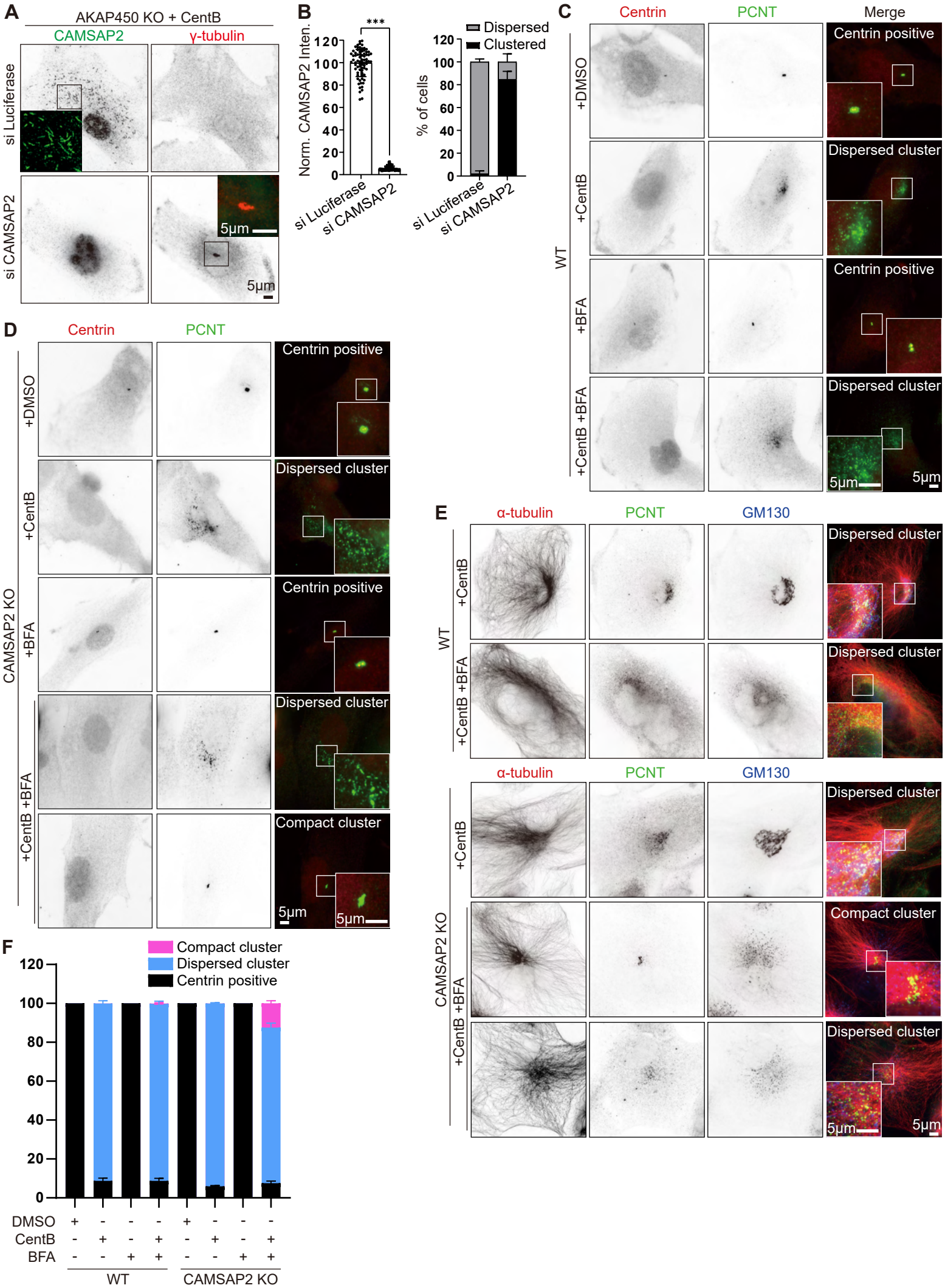

Figure 1 - figure supplement 2

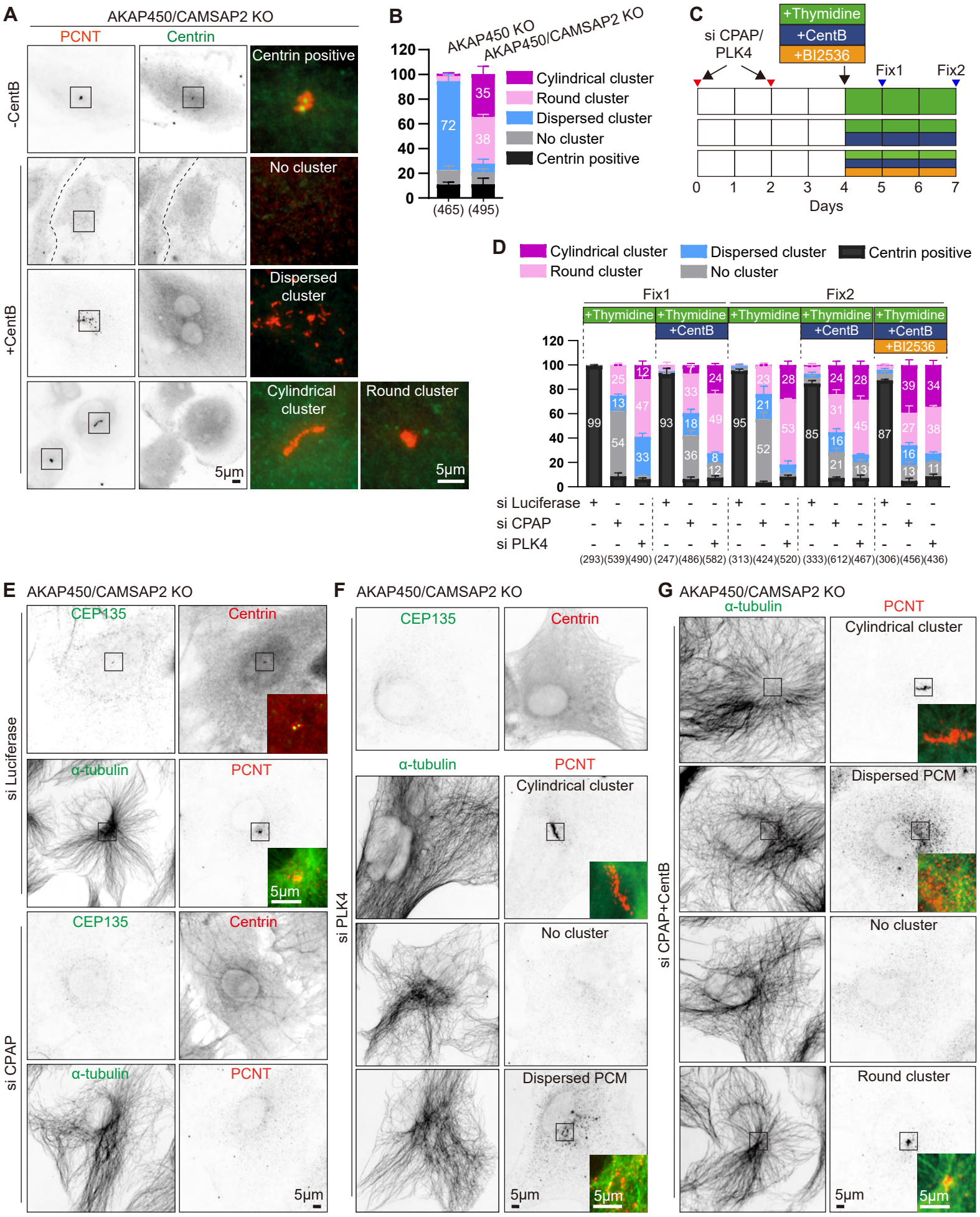

Figure 1 - figure supplement 3

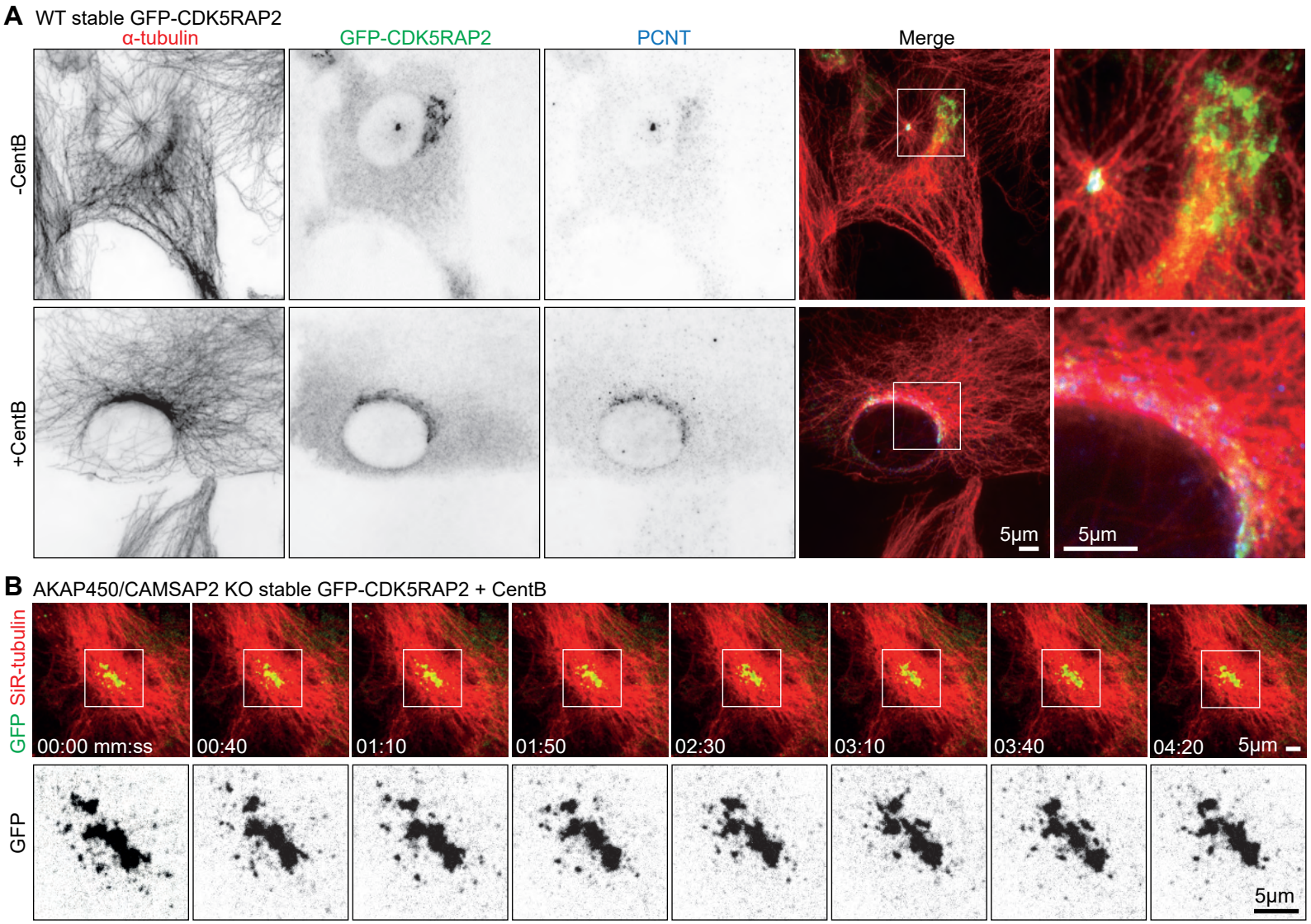

Figure 2- figure supplement 1

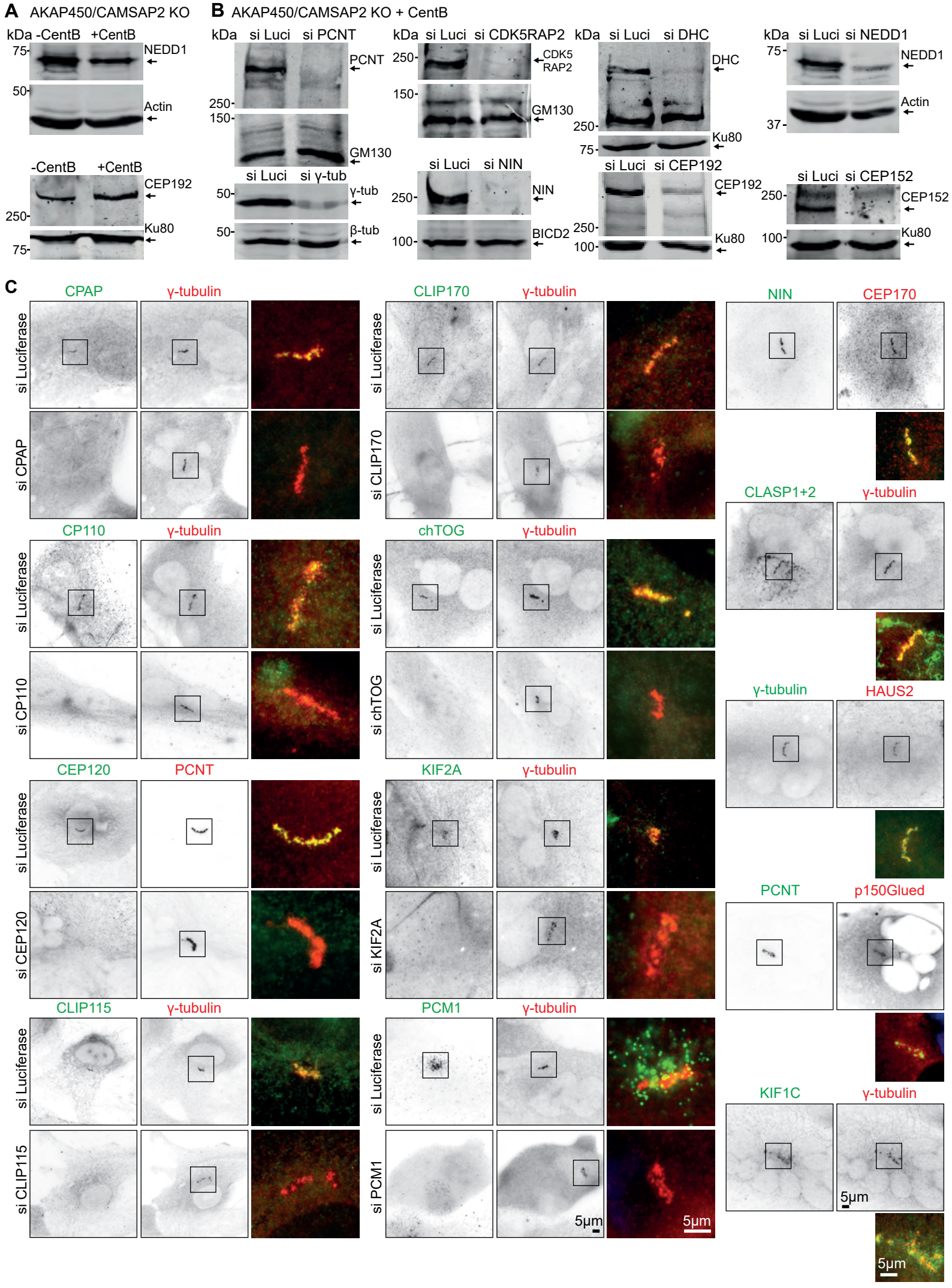

Figure 2 - figure supplement 2

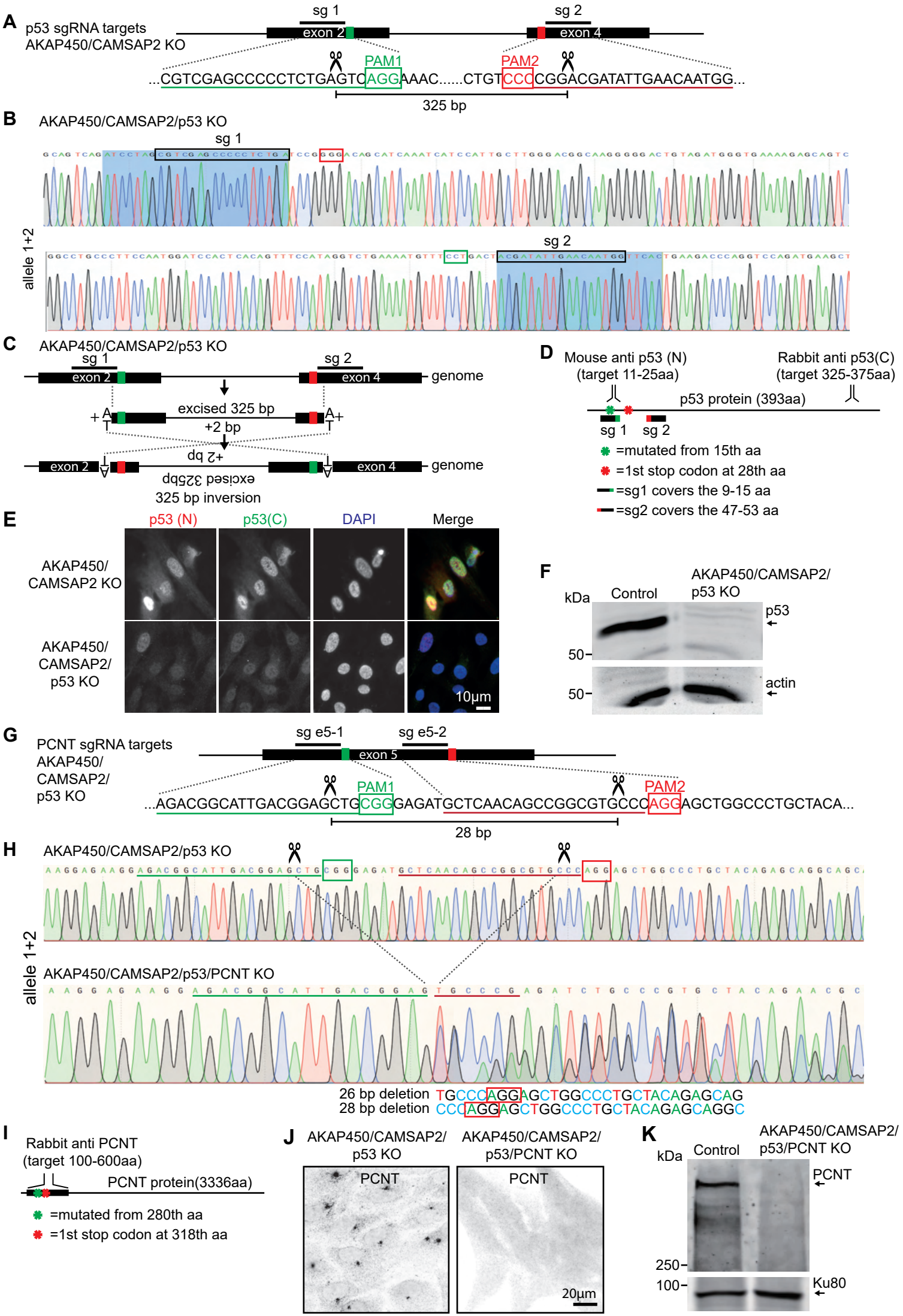

Figure 2 - figure supplement 3

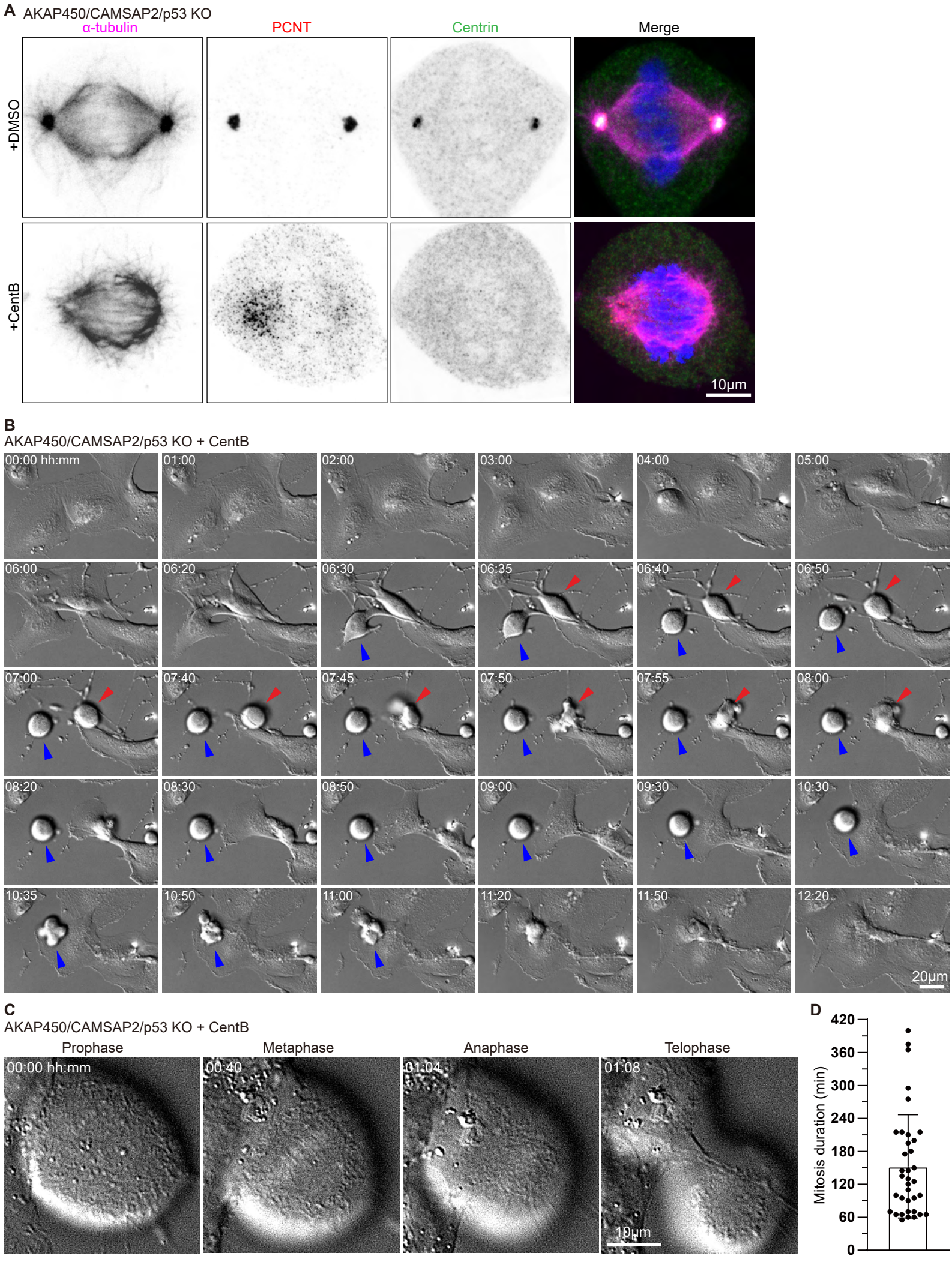

Figure 2 - figure supplement 4

A Control=AKAP450/CAMSAP2/p53 KO + CentB

PCNT KO=AKAP450/CAMSAP2/p53/PCNT KO + CentB

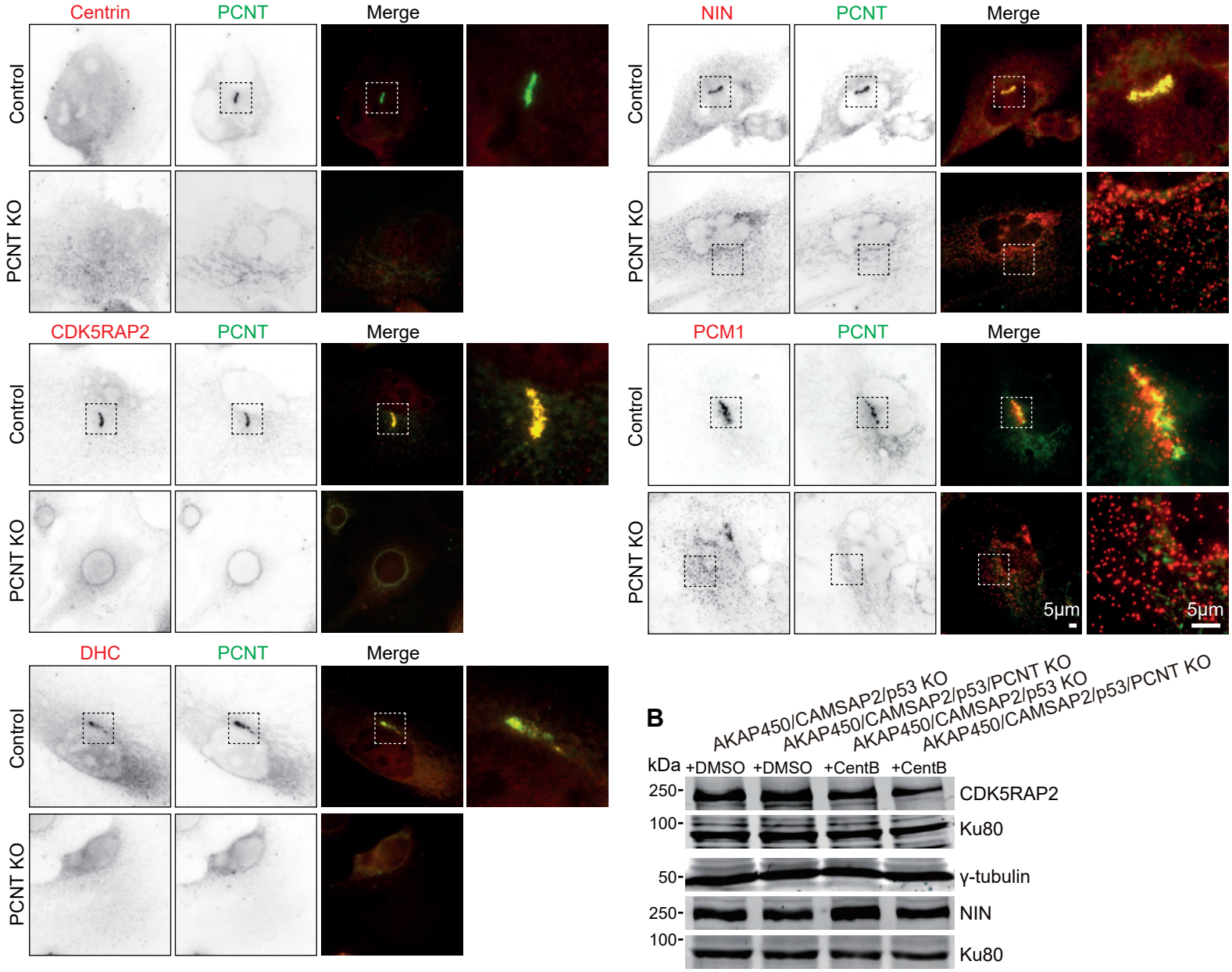

B

Figure 2 - figure supplement 5

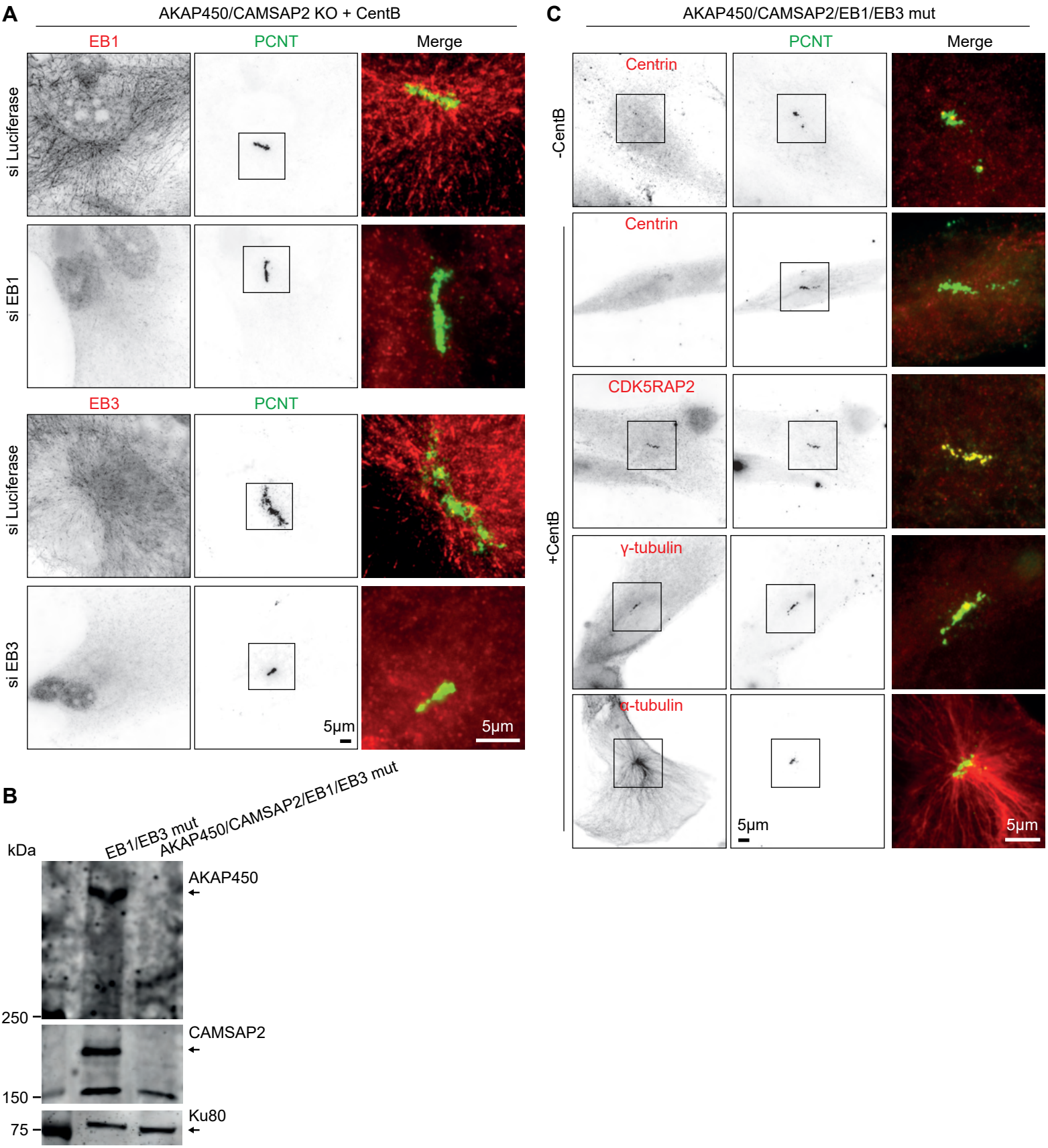

Figure 4 - figure supplement 1

A AKAP450/CAMSAP2 KO stable GFP-CDK5RAP2 + CentB

Noco treatment

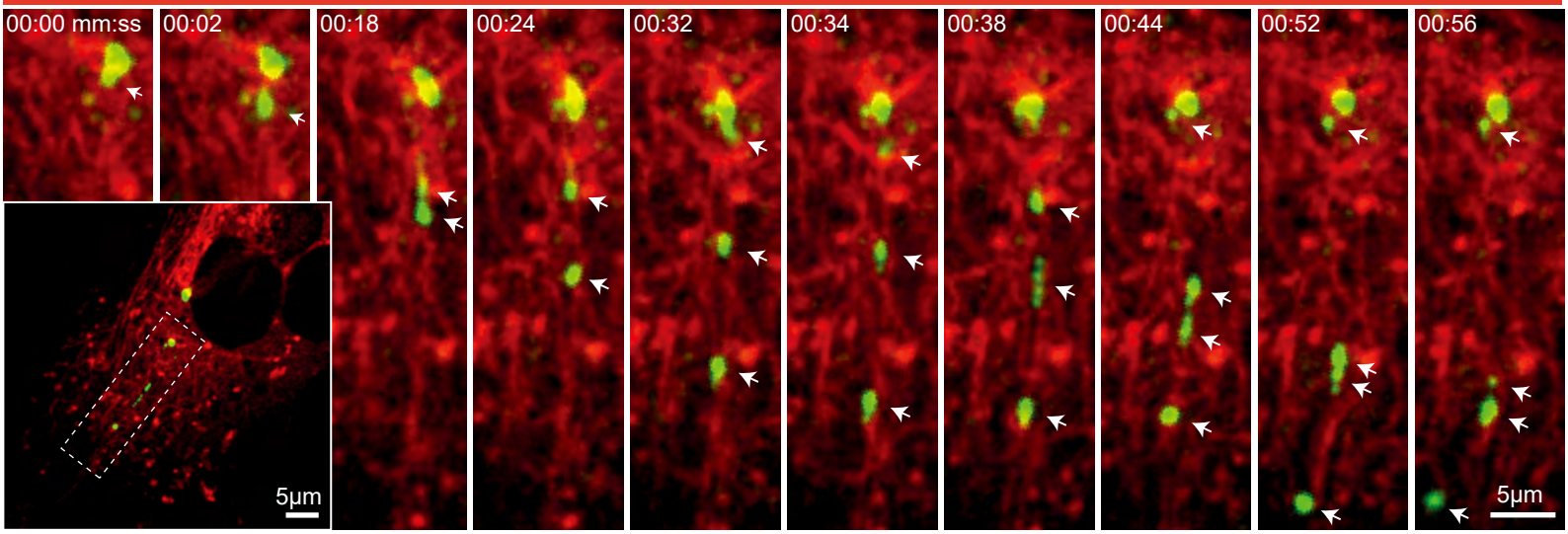

B AKAP450/CAMSAP2 KO + CentB

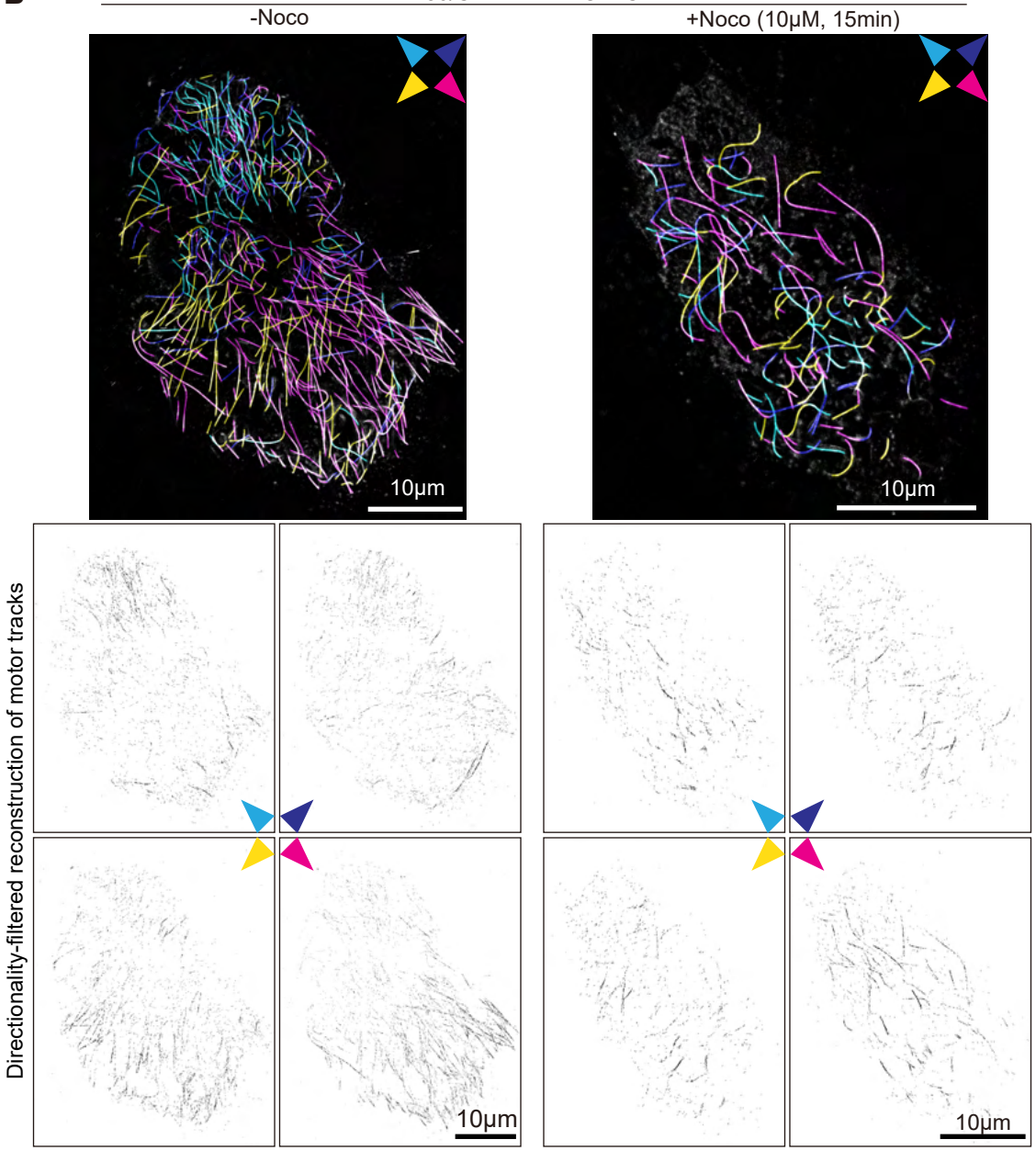

C AKAP450/CAMSAP2 KO + CentB, Cold treatment (30min 4°C)

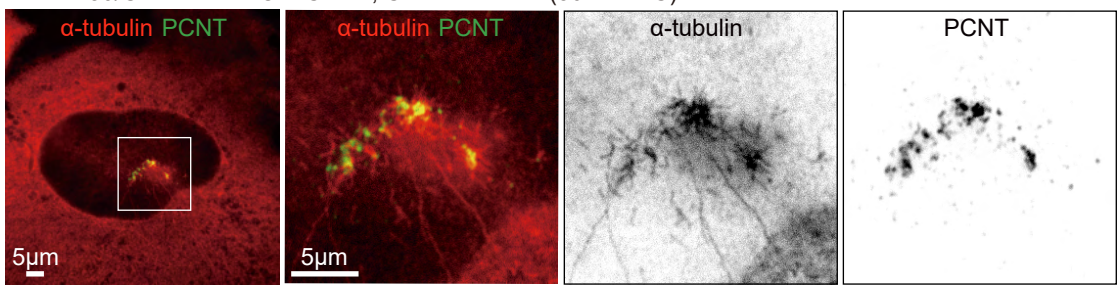

Figure 5 - figure supplement 1

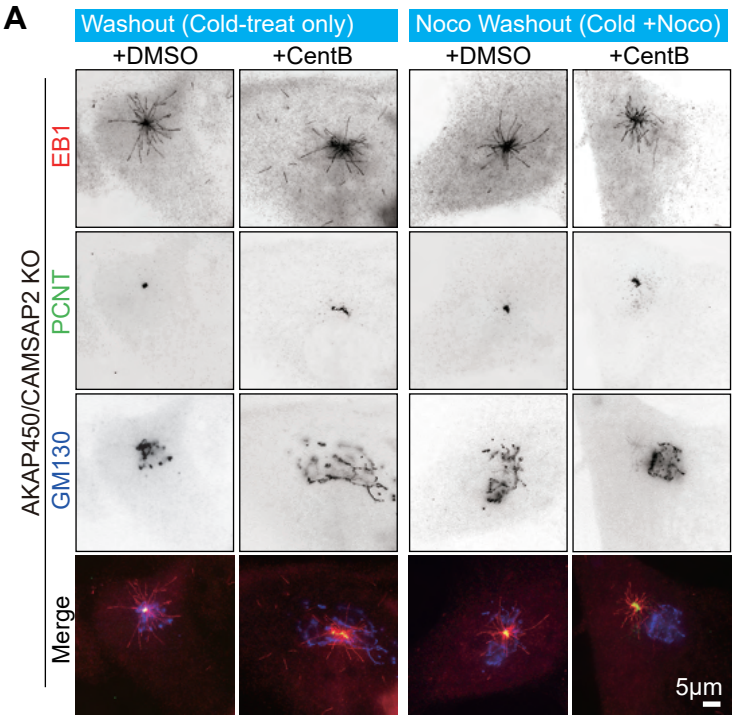

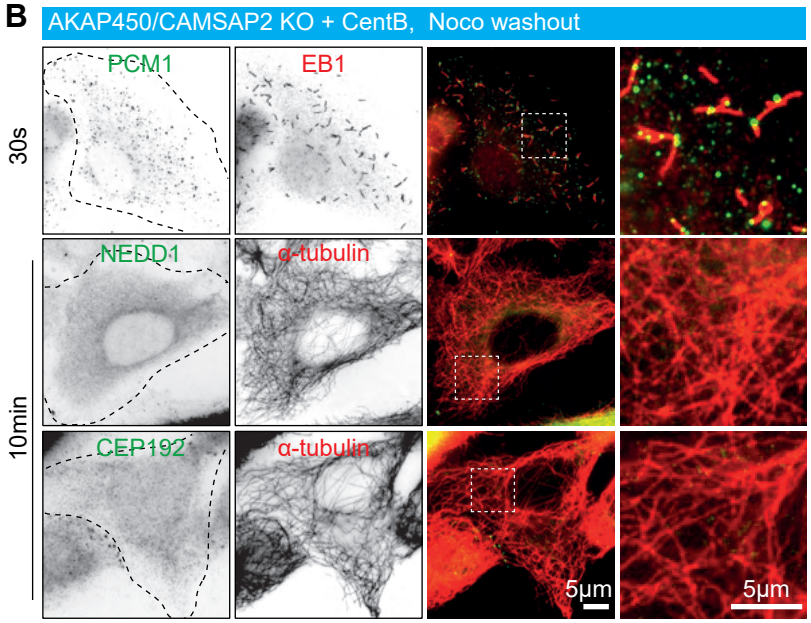

C Presence of PCM proteins in clusters before and after Noco washout

CentB	-	+	+	+	+	+
Nocodazole	-	-	+	+	+	+
Washout			30s	2min	5min	10min
PCNT	+	+	+	+	+	+
CDK5RAP2	+	+	+	+	+	+
γ-tubulin	+	+	+	+	+	+
NEDD1	+	-	-	-	-	-
Ninein	+	+	-	+	+	+
CEP192	+	-	-	-	-	-
PCM1	+	+	+	+	+	+

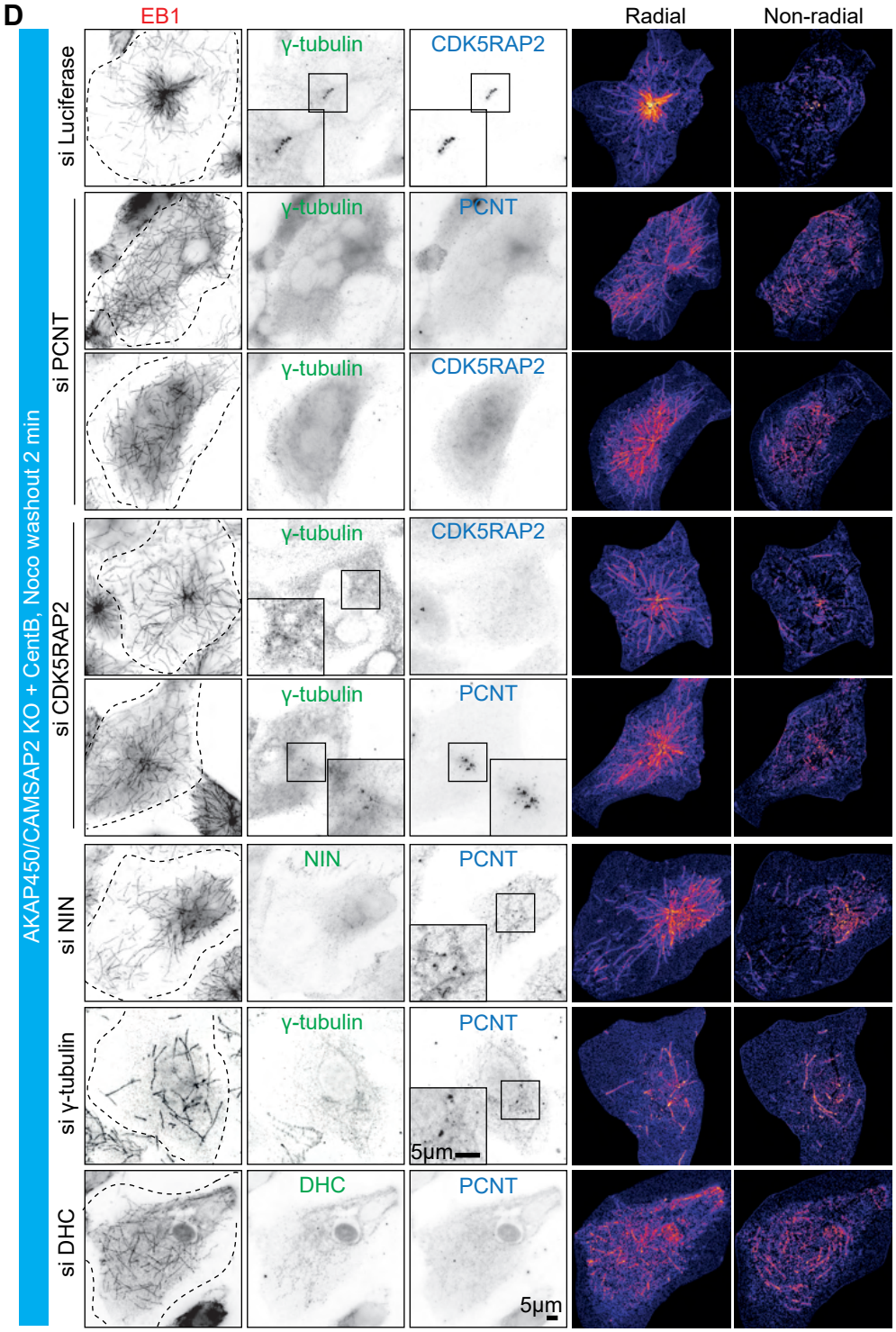

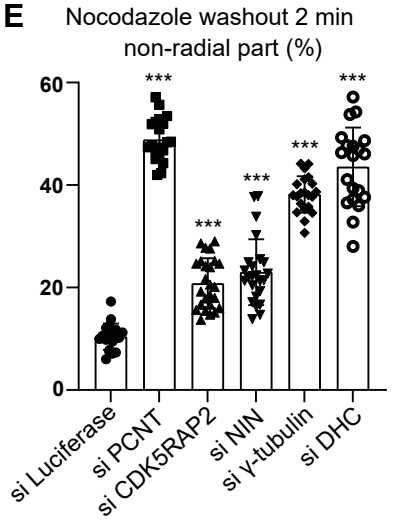

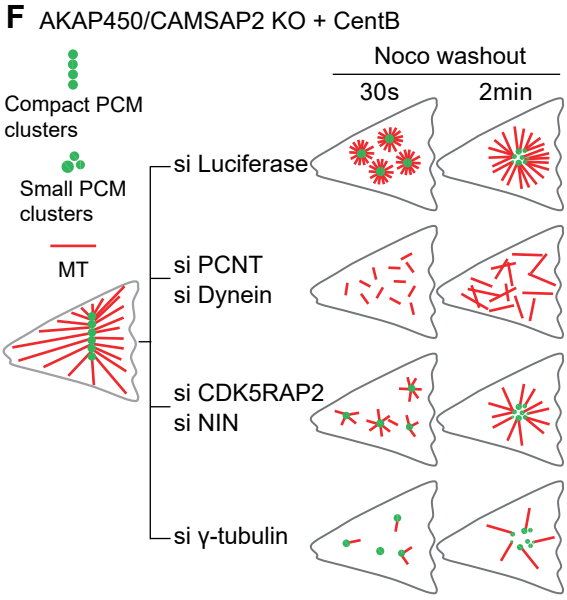

Figure 5 - figure supplement 2

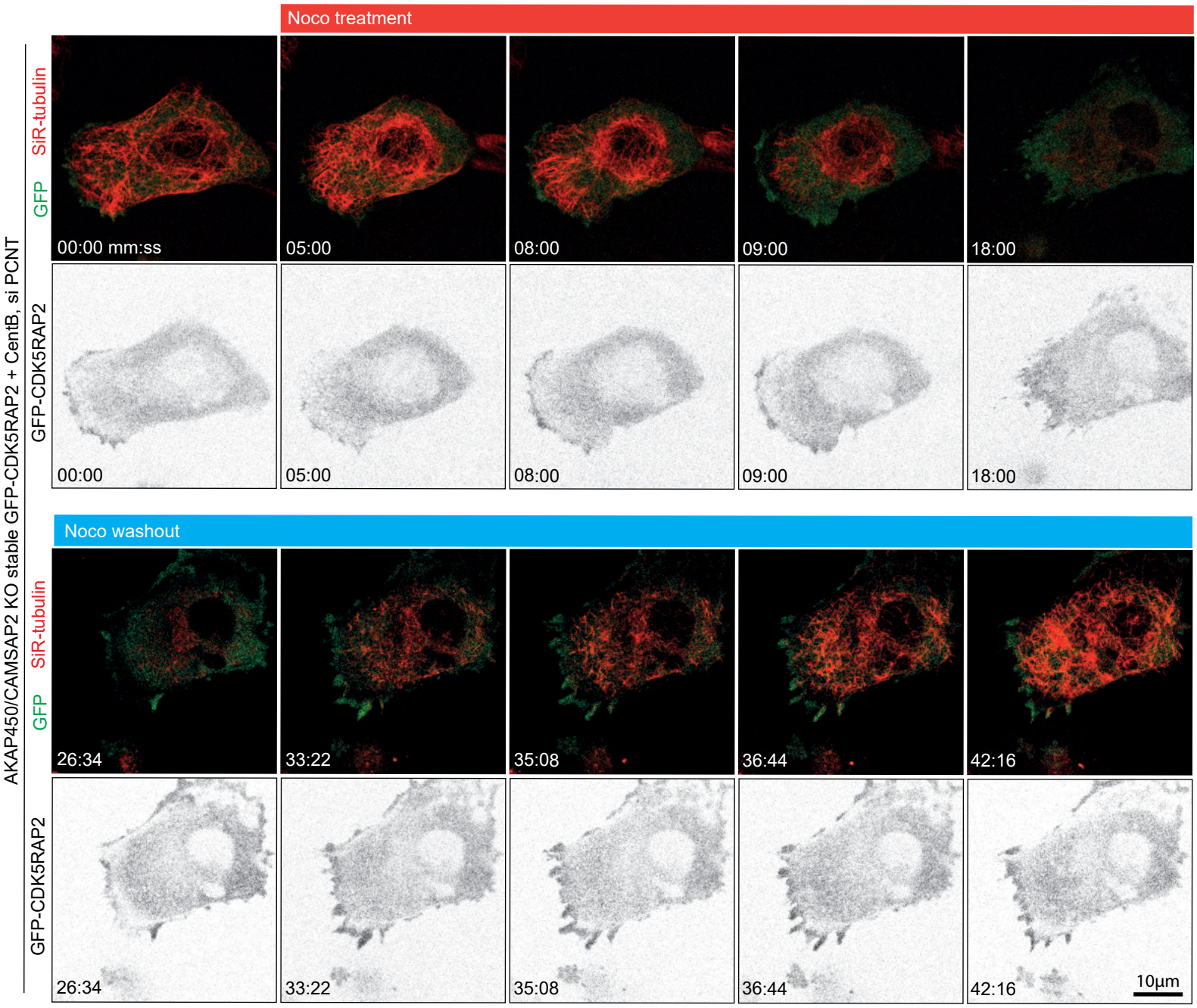

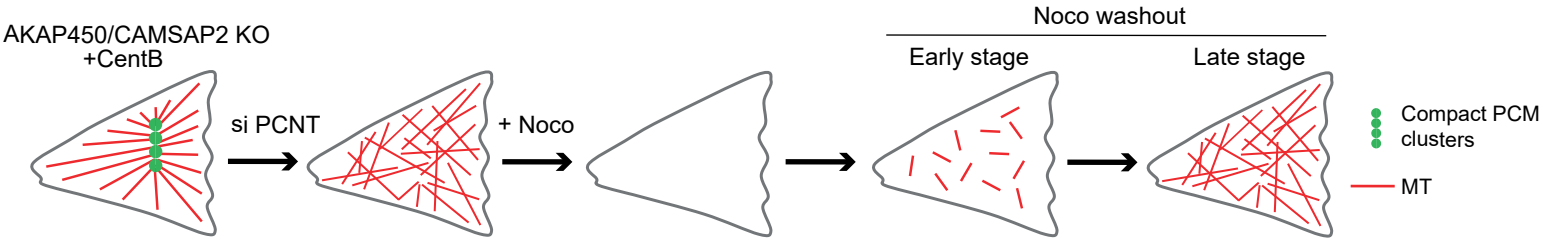

Figure 6 - figure supplement 1

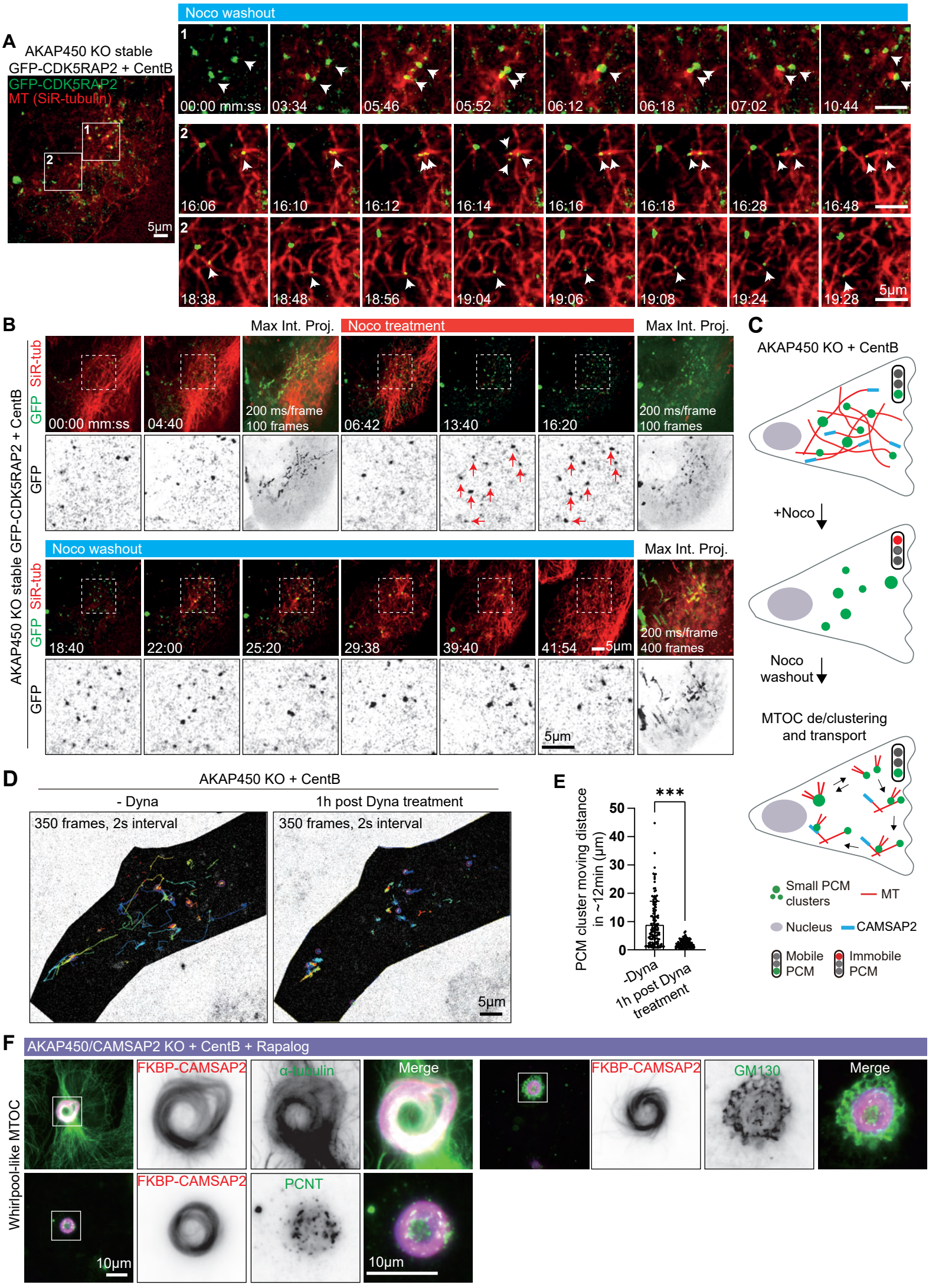

Figure 6 - figure supplement 2

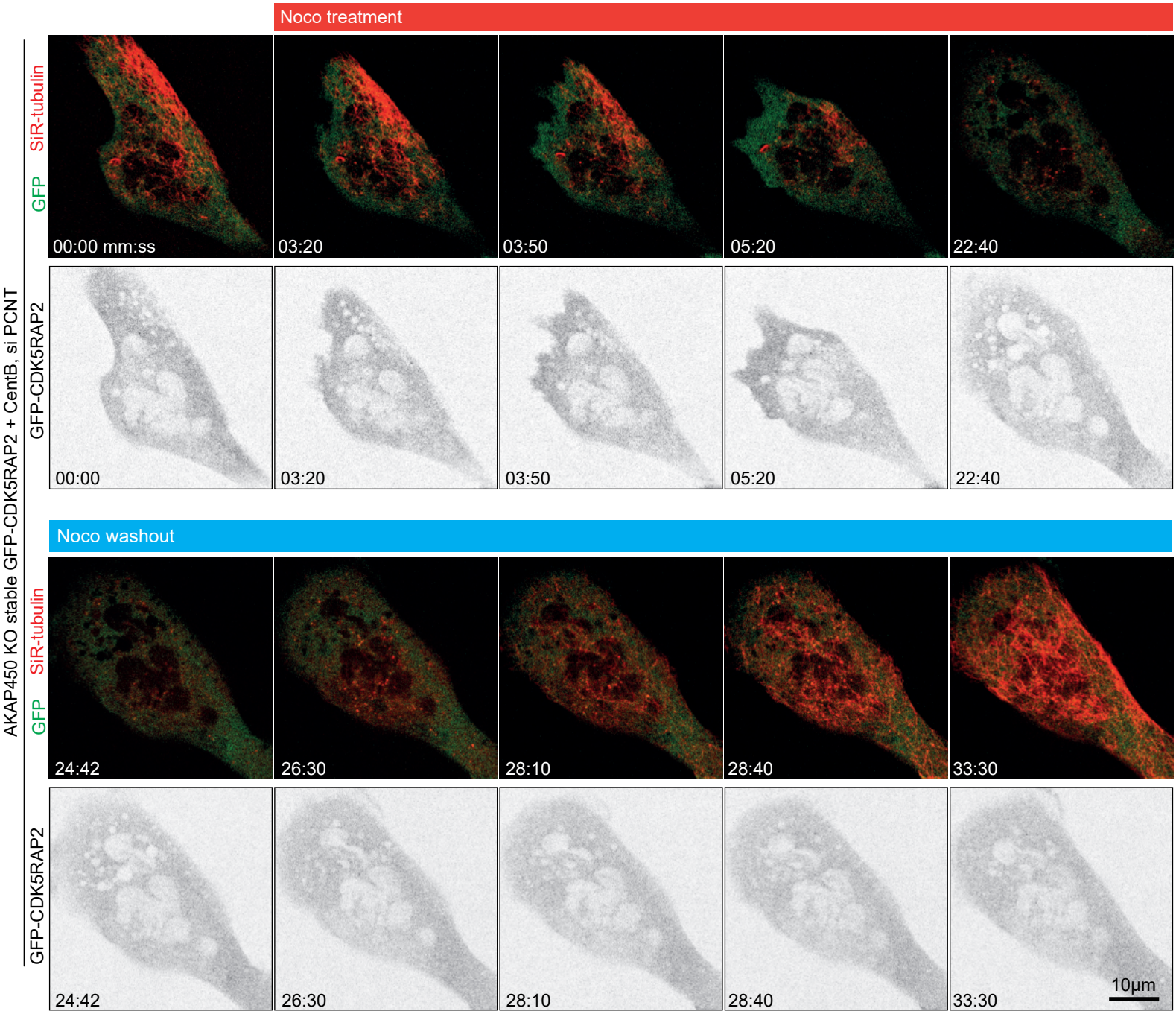

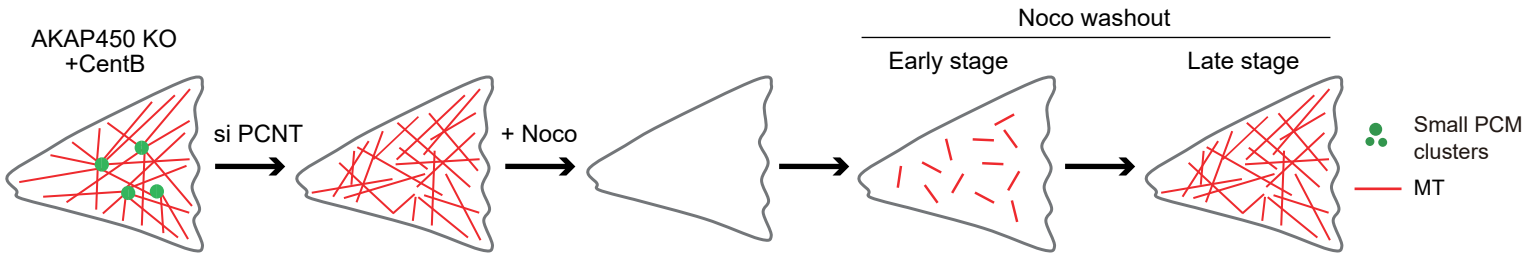

Figure 7 - figure supplement 1

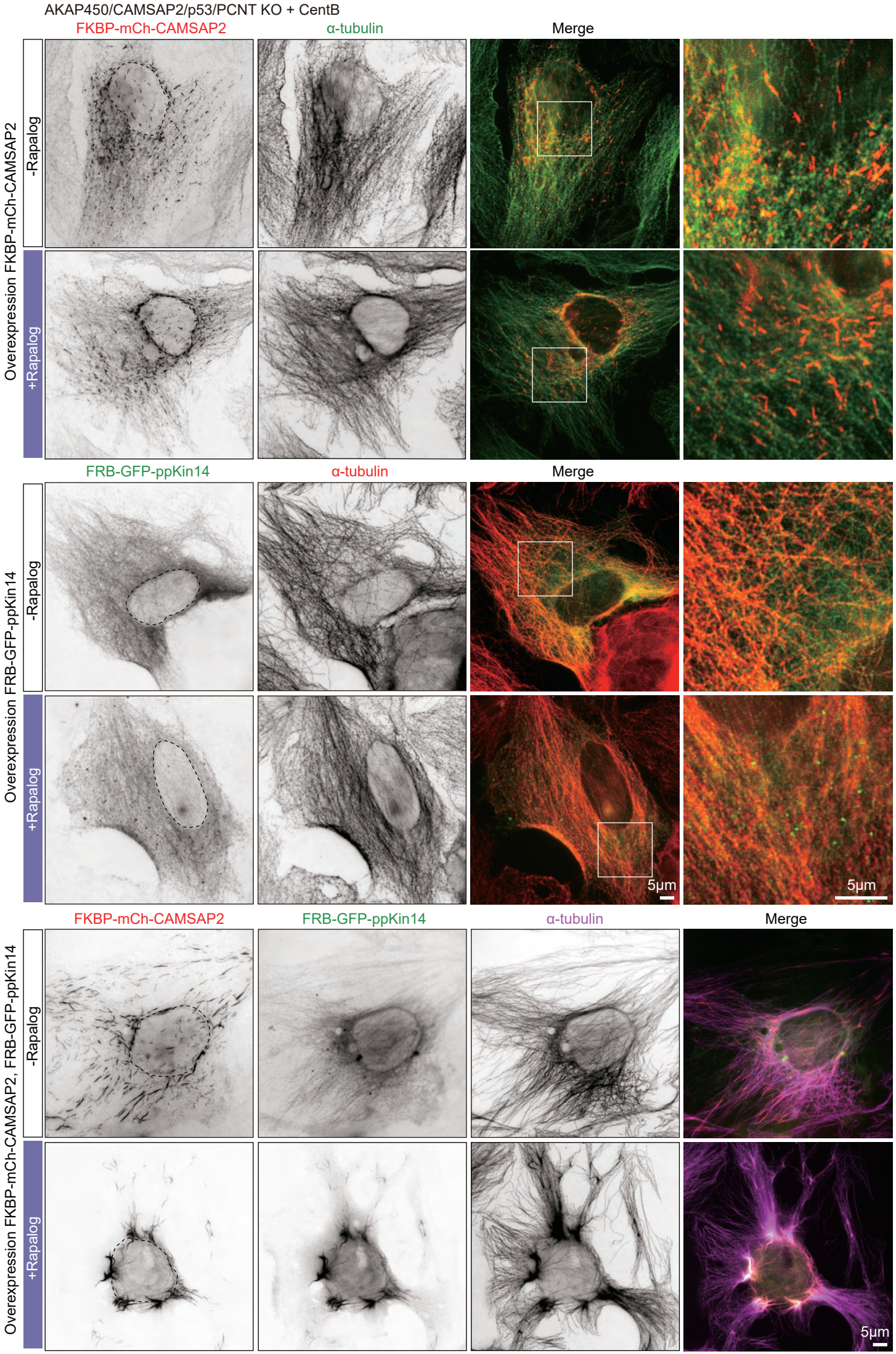

Figure 7 - figure supplement 2

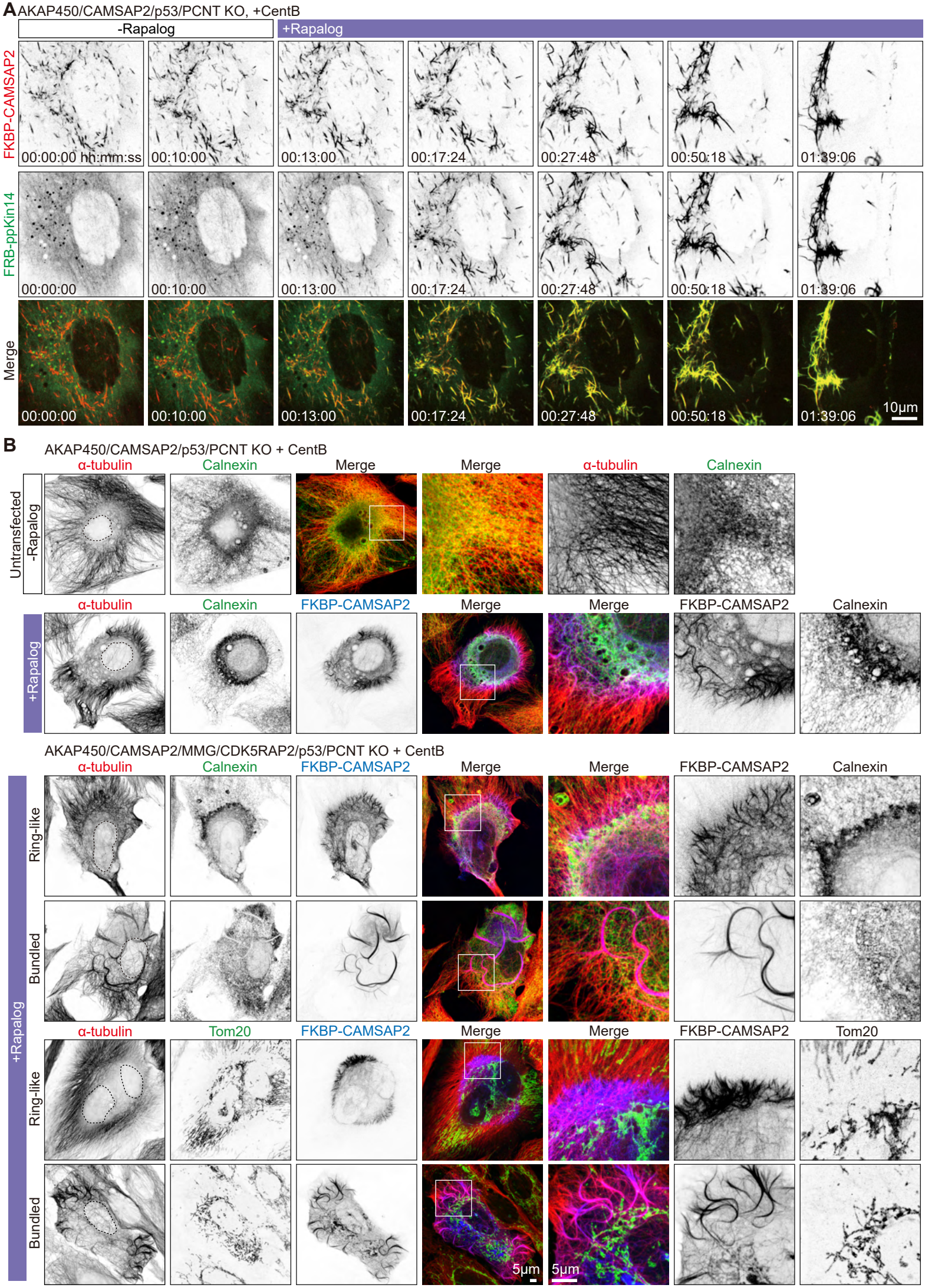

Figure 7- figure supplement 3

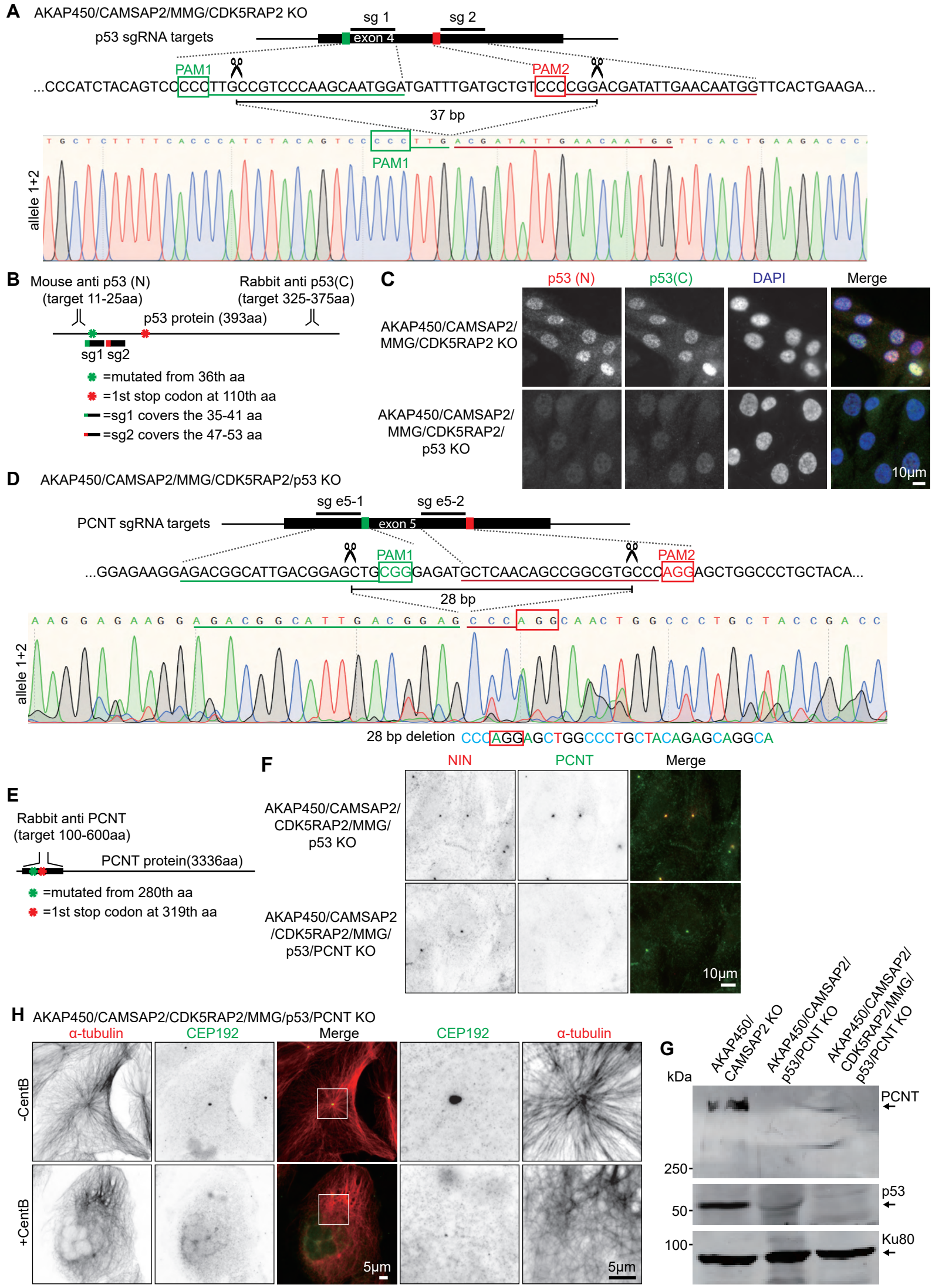

Source data 1
Uncropped Western blots shown in this manuscript

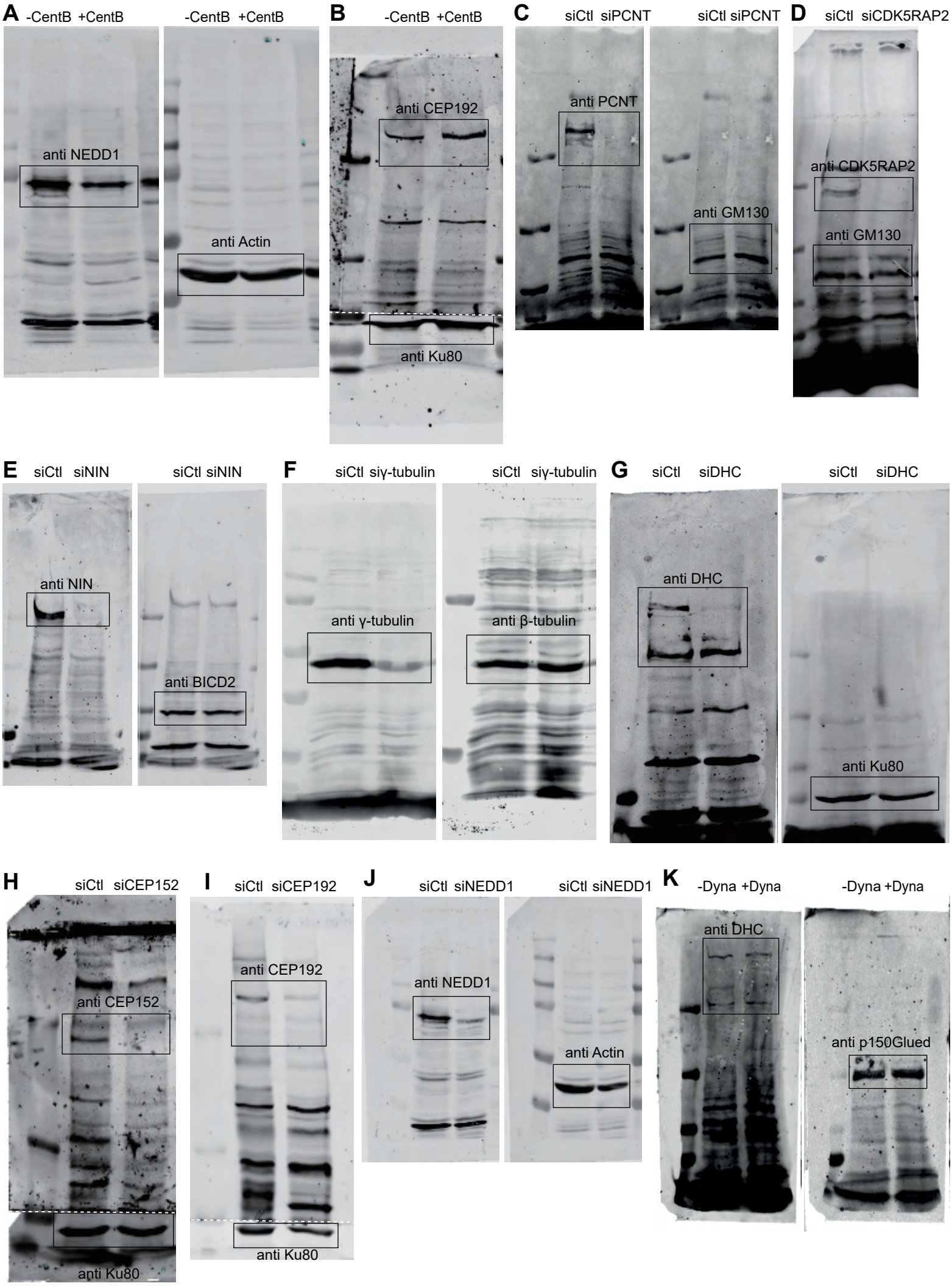
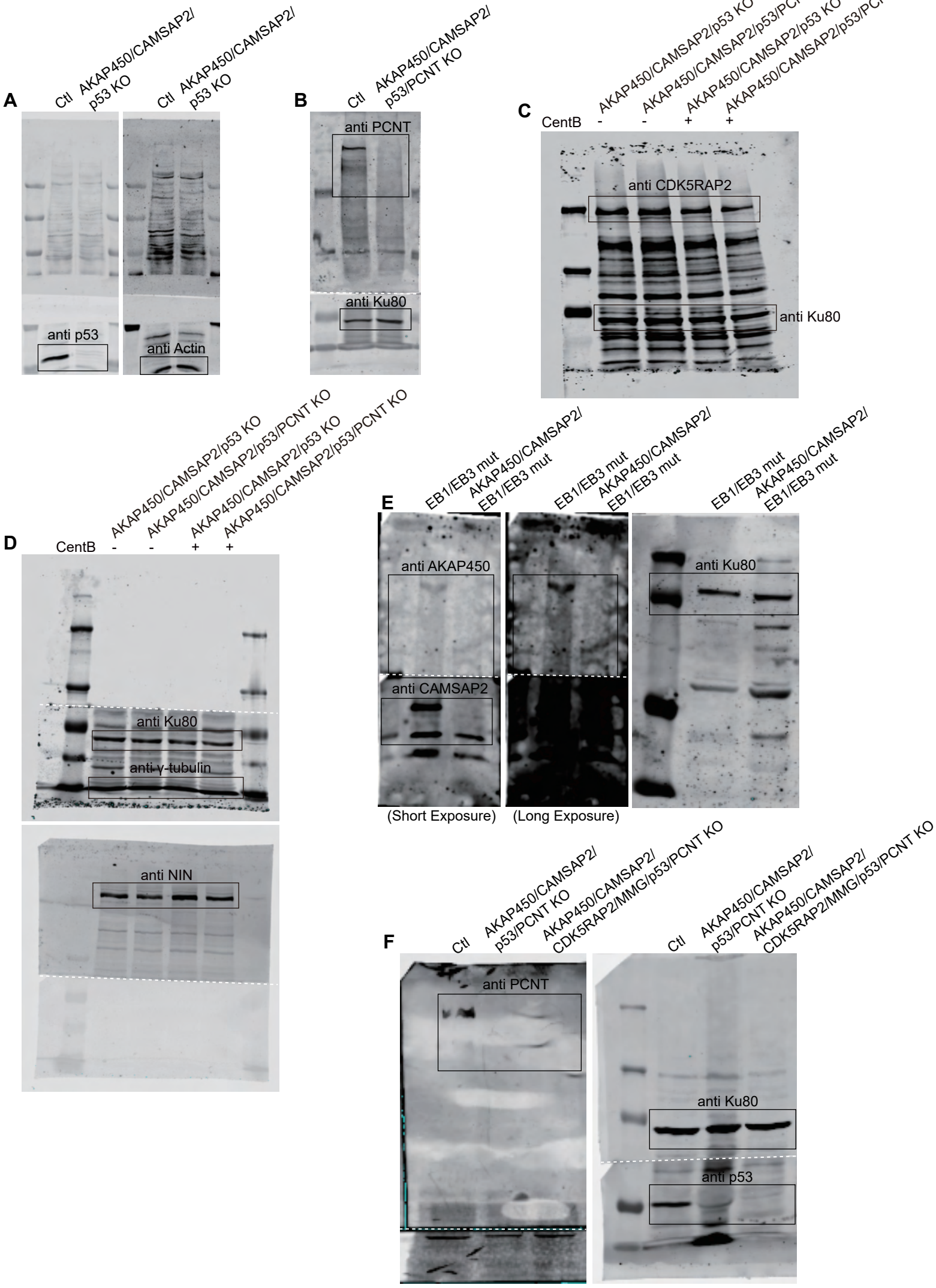
Source data 2
Uncropped Western blots shown in this manuscript